Friedrich-Schiller-Universität Jena
Physikalisch-Astronomische Fakultät
Thüringer Landessternwarte Tautenburg

seit 1558

Transiting Sub-stellar companions of Intermediate-mass stars

Dissertation
zur Erlangung des akademischen Grades

doctor rerum naturalium (Dr. rer. nat.)

vorgelegt dem Rat der Physikalisch-Astronomischen Fakultät
der Friedrich-Schiller-Universität Jena

von Dipl.-Phys. Daniel Sebastian

geboren am 03. März 1987 in Leipzig

Gutachter

1.   Prof. Dr. Artie P. Hatzes

                Thüringer Landessternwarte Tautenburg

2.   Prof. Dr. C.W.M. Fridlund

                Leiden Observatory

3.   Prof. Dr. Sebastian Wolf

                Christian-Albrechts-Universität zu Kiel

Tag der Disputation: 23.05.2017

Übersicht

Ziel ist es, durch die Messung der absoluten Häufigkeiten kurzperiodischer Planeten von IMSs (engl. für Sterne intermediärer Masse) die Vorhersagen von Theorien der Planetenentstehung zu testen.

Überraschend war in den späten 90ern die Entdeckung von sogenannten heißen Jupitern bei sonnenähnlichen Sternen. Solche schweren und sehr nah bei ihren Sternen ($< 0.1\,\mathrm{AE}$) umlaufenden Planeten gibt es nicht in unserem Sonnensystem. Die gängige Theorie ist, dass Planeten in großer Entfernung zum Stern entstehen und dann durch Wechselwirkungsprozesse zum Stern hin migrieren. Wechselwirkungen der Planeten mit der protoplanetaren Scheibe, welche diese Migration erklären können, tragen allerdings nur effektiv zur Migration bei, solange die Scheibe existiert.

Die Erforschung von nahen Planeten bei IMSs kann effektiv die Parameter der Entstehung dieser Planeten eingrenzen. Erstens ist von Infrarotbeobachtungen bekannt, dass die Lebenszeiten von protoplanetaren Scheiben dieser Sterne nur halb so lang sind wie die von sonnenähnlichen Sternen. Zweitens wurde durch Radialgeschwindigkeitsstudien von entwickelten IMSs entdeckt, dass diese im Vergleich zu Sternen mit sonnenähnlicher Masse viel häufiger Planeten in weiten Umlaufbahnen ($> 5\,\mathrm{AE}$) besitzen. Allerdings ist nicht viel über die nahen Planeten um IMSs bekannt. Ein wichtiger Schlüssel, um die Parameter der Entwicklung dieser Objekte einzugrenzen, ist die Antwort auf die Frage: **"Gibt es eine höhere Häufigkeit von diesen sehr nah umlaufenden Planeten bei Sternen mittlerer Masse als bei Sternen mit sonnenähnlicher Masse?"**

Die Transitmethode ist am besten geeignet, um solche Planeten zu finden. Erstens hat bei der Methode die schnelle Rotation der Sterne keinen Einfluss, zweitens ist sie ideal, um kurzperiodische Planeten zu finden. Im Gegensatz zu bodengebundenen Teleskopen erlaubt es die Genauigkeit des Weltraumteleskops CoRoT, alle jupitergroßen, transitierenden Objekte bei IMSs zu detektieren. Um die Massenverteilung der Sterne in der CoRoT-Durchmusterung zu bestimmen, habe ich zunächst eine repräsentative Stichprobe von 7 131 Sternen spektral klassifiziert. Anschließend wurden mehr als 123 000 Lichtkurven der CoRoT-Mission untersucht, um Transitkandidaten zu finden. 14 Kandidaten habe ich daraufhin genauer analysiert um herauszufinden, ob es sich um sub-stellare Begleiter handelt oder nicht.

Als Ergebnis dieser Durchsuchung habe ich einen Planeten und zwei sehr junge braune Zwerge mit übergroßen Radien bei IMSs gefunden. Darunter befindet sich der erste, transitierende, braune Zwerg der überhaupt bei einem B-Stern entdeckt wurde. Dieses Ergebnis bestätigt, dass es kurzperiodische Planeten um IMSs gibt. Die absolute Häufigkeit kurzperiodischer Planeten wurde bei dieser Durchmusterung mit $0.11 \pm 0.04\,\%$ berechnet. Damit sind kurzperiodische, massereiche Planeten von Sternen mittlerer Masse sowohl im Vergleich zu den langperiodischen Planeten dieser Sterne, als auch im Vergleich zu den sonnenähnlichen Sternen weniger häufig. Im Kontext der Theorie der Scheibenmigration lässt sich dieses überraschende Ergebnis am besten damit erklären, dass die Lebensdauer der Scheiben dieser Sterne zwar ausreicht, um Planeten entstehen zu lassen, aber nicht ausreicht, um diese anschließend zum Stern migrieren zu lassen.

Abstract

The aim of the project is to evaluate the predictions from theories of planet formation by determining the absolute frequency of close-in planets of intermediate-mass stars (IMSs).

In the late 90s, the detection of hot Jupiters orbiting solar-type stars was a big surprise. These massive and extreme close-in ($< 0.1\,\mathrm{AU}$) planets have no counterpart in our Solar System. State-off-the-art theories of planet formation predict that these planets first form at large distances from their host stars. Due to interaction processes, they migrate then inwards to distances of $0.1\,\mathrm{AU}$ and less. Even though other processes exist, it is commonly accepted that planet-disc interactions are the main source of migration. Therefore, planets can only migrate due to this process as long as the disc exists.

The detection of close-in planets of IMSs can put constraints to these theories of planet formation. First, it is known from infrared observations that the lifetimes of protoplanetary discs of IMSs are half as long as those of solar-mass stars. Second, radial velocity surveys of evolved IMSs show that the frequency of planets at distances larger than $5\,\mathrm{AU}$ is higher in comparison to solar-mass stars. However, not much is known about the frequency of close-in planets. An important key to constrain processes of planet formation and evolution is, thus, answering the question: **"Is the frequency higher for close-in planets of IMSs than for solar-mass stars?"**

The transit method is best suited to find such planets. First of all, it is not affected by the fast rotation of these stars and secondly, it favours the detection of close-in planets. I used the CoRoT database to survey all IMSs observed with this instrument. In contrast to ground-based surveys, the precision of CoRoT allows the detection of all Jupiter-sized transiting objects orbiting IMSs. To determine the mass-distribution of the stars in the sample, I first did a spectral classification of a representative sample containing $7\,131$ stars. To find transit candidates, more than $123\,000$ light-curves from the CoRoT mission were analysed. I finally identified and observed 14 candidates to find out whether they are sub-stellar companions or not.

In result, I detected one planet as well as two very young brown dwarfs with large radii of IMSs by this survey. Among them, the first transiting brown dwarf of a B-type star. This result confirms that close-in planets of IMSs exists. The frequency for close-in planets of IMSs derived from this survey is $0.11 \pm 0.04\,\%$. This means that close-in planets are less frequent than long-periodic planets of IMSs and they are less frequent than close-in planets of solar-type stars. In the context of disc-migration, this surprising result can be explained by the lifetime of the protostellar discs of IMSs. It is apparently long enough for the planets to form, but on average too short for them to migrate inwards.

Contents

Glossary

a-M	semimajor-axis-mass		**IRAF**	Image Reduction and Analysis Facility
ASFIA	Automatic Spectral FItting Application		**log(g)**	Surface gravity
BEB	Background eclipsing binary		**LR**	long-run
CAFE	Calar Alto Fiber-fed Échelle spectrograph		**LSD**	Least-Squares Deconvolution
CCD	Charge-coupled Device		**M-R**	mass-radius
CCF	cross-correlation function		**PSF**	Point spread function
CFHT	Canada France Hawaii Telescope		**RM**	Rossiter-McLaughlin
CoRoT	COnvection ROtation and planetary Transits		**RV**	Radial velocity
ESO	European Southern Observatory		**S/N**	signal-to-noise ratio
HARPS	High-Accuracy Radial velocity Planetary Searcher		**Spt**	Spectral type
IMS	Intermediate-mass star		**SR**	short-run
IR	Initial run		T_{eff}	Effective temperature
			ThAr	Thorium-Argon
			TLS	Thüringer Landessternwarte Tautenburg

Units

AE	Astronomische Einheit		$M_\odot$	Solar mass
AU	Astronomical unit		M_{Jup}	Jupiter mass
HJD	Heliocentric Julian date		R_{Jup}	Jupiter radius
mag	Magnitude			

1 Introduction to sub-stellar objects

Improvements in space exploration revealed extraordinary insights in the objects of our Solar System. With space probes we see and analyse the objects in our Solar System in great detail. For example, recently hints for active volcanism on the planet Venus were observed from an orbital probe (Shalygin et al. 2015), or the origin of sinkholes on cometary surfaces is discussed and their activity was monitored (Vincent et al. 2015). Many discoveries in our own Solar System deliver hints for a fundamental question: How did our Solar System form and which processes played a role in its development?

This question is closely related to the evolution of our Sun itself. When we analyse the evolution of planetary atmospheres, we know that the Sun was much more active in the first 100 million years. It was a T-Tauri star and emitted about 1000 times more Extreme-UV radiation (EUV: $200 \leq \lambda \leq 911\,\text{Å}$) than today. Afterwards, the EUV radiation decreased slowly as the Sun evolved on the main sequence (Ribas et al. 2005). Strong EUV radiation lead to a heating and expansion of the thermosphere of terrestrial planets. Such an expansion can lead to a sufficient atmospheric loss. For example, Tian et al. (2009) calculated that if Mars started with a dense atmosphere of CO_2, it would not have maintained this atmosphere during the first hundred million years of evolution until the EUV radiation became weak enough for it to accumulate a dense CO_2 atmosphere again.

Apart the direct space exploration, another major approach to answer this question is to observe other planetary systems. This is well known from the developments in stellar physics. Due to its small distance and the possibility of very detailed observations, our Sun is the most well characterised star. By setting our Sun as reference, the other stars have been observed spectroscopically for more than a century now. Nowadays, we not just know much about there phenomenological differences, as they are for example explained and catalogued in the MK-system (Morgan et al. 1943), but also about their physical properties. This is possible because of the continuous development of spectroscopic instruments, from broad- and narrow-band photometers and high-resolution spectrographs to instruments installed on-board of space observatories.

The observation of planetary systems can also be used to unveil the mystery of the development of our own Solar System. Just like the investigation of the stars before, such explorations reveal the diversity of planetary systems. Through observation of such systems in different states of their evolution, we will finally be able to classify our Solar System and its bodies. We will be able to discern whether the Solar System is unique, or maybe it is even part of a whole class of planetary systems that is common for a certain type of stars. Even further, we can better understand whether Earth-like planets with oceans and continents filled with a big variety of life exist, and where to find them.

In contrast to the spectroscopic investigation of stars, it is much more difficult to analyse planetary systems. The challenge is the close proximity of the planet to the star and the large brightness ratio. Given the distance of Jupiter to the Sun of about five AU, this would be translated to a distance of 3.74 arcseconds for one of the nearest stars $\alpha\,Cen$. This distance could easily be resolved with amateur telescopes, but it becomes much smaller for more distance stars. Typically we would expect separations of about 0.1 to 0.5 arcseconds. Additionally, the planet brightness depends on how much light is reflected from the host star. For

example, the system Sun-Jupiter exhibits a brightness difference of about 10^{-9}. Exactly this brightness difference is the problem for detecting planets orbiting other stars. It is just not possible to observe and study a planetary system directly. This is comparable with taking a picture of a tiny insect in front of a stadium lamp. Therefore, several detection mechanisms have been developed in the last decades.

1.1 The melange of planet-detection methods

Perryman (2011) describes in detail the methods that are commonly used to discover planetary systems. In this section I will give a brief summary of the different methods used nowadays, their sensibility and their impact up to now. Furthermore, I will specially focus on the two methods with the most impact into the field of exoplanets in the past years. Some methods require the development of more accurate and precise techniques or depend on space-based observations.

Astrometry: The classical method to measure distances of stars is astrometry. If our Earth revolves around the Sun in half a year, the projected position of the star has changed by its angle of parallax. This angle depends trigonometrically to the distance of the star. For example, for one of the closest stars $\alpha\,Cen$ the parallax is 0.74 arcseconds. The measurement of the position therefore has to be very accurate. This method is sensitive to planets with long orbital periods ($P \geq 1\,yr$). Most of the detected planets today have very close-in orbits, leading to astrometric displacements of just several $\mu arcsec$.

The early exoplanet hunters used astrometry to search for exoplanets. For example, van de Kamp (1982) reported the discovery of two planets orbiting Barnard's star. The measured displacements could not be reproduced by other observatories and were later found to be caused by instrumental effects. Up to now, only few planets have been detected by this method (see for example Muterspaugh et al. (2010) and Sahlmann et al. (2013)). However, the impact of this method is expected to increase dramatically with the release of the GAIA catalogue. According to Perryman et al. (2014), about 21,000 massive exoplanets within $500\,pc$ will be found with GAIA in its 5- yr survey.

Microlensing: Microlensing profits from the effect of general relativity, which states that light is deflected as a result of the distortion of space-time. Such a distortion of space-time is caused by the presence of matter. Radiated light from a distant source is bent in the vicinity of a foreground source (e.g. a star). As a result, the light of the source is focused and amplified. The mass of the foreground source acts literally like a lens, a so-called gravitational lens. If the images of the sources are unresolved, like in the case of stars, the effect is called microlensing. Strong microlensing events show magnifications of several magnitudes. The amplification depends on the mass and on the geometry of the lensing object. The first exoplanet detected via microlensing was published by Bond et al. (2004).

Since such an event only occurs if the geometry of source and lens is very close to the line of sight, these events are very rare. Surveys to detect microlensing events, like OGLE (Optical Gravitational Lensing Experiment, Udalski 2009), concentrate on regions in the sky with a

large stellar density. Typically, it is near the central regions of our Milky Way. Discoveries are only possible if thousands of stars are continuously observed over a long period of time. Up to now, 33 single planets and 2 systems have been discovered using microlensing (http://exoplanet.eu, Schneider et al. 2011).

Direct imaging: The direct detection of an exoplanet is extremely difficult because of the extreme brightness contrast between planet and star, as well as the location of the planet in the vicinity of the star. Nevertheless, the development of telescope techniques allowed the detection of several planets in wide orbits in the past years . Chauvin et al. (2005) reported a planetary companion orbiting the M dwarf 2M J1207. They used an 8-m telescope with an adaptive optic system to remove scintillations of the atmosphere of the Earth. Additionally, they observed in the infrared wavelength regime where the flux-ratio between star and planet can rise up to 10^{-4} for nearby stars (Burrows et al. 2004). Further discoveries have been reported in the past years, yielding several planets orbiting young intermediate-mass stars (see Quanz 2015).

Timing: Periodic signals can be measured from radio pulsars, eclipsing binaries, transiting planets (see section 1.3), and pulsating stars. The reflex motion of such a star or planet due to the gravitational influence of one or more objects can be the source of timing variations. The more accurately the periodic signal can be measured, the more precise the reflex motion can be measured and, thus, the mass of the companion can be derived. Pulsars are neutron stars that exhibit very stable radio pulses. Therefore, The first exoplanets were discovered by pulsar timing (Wolszczan & Frail 1992). They reported a system of two exoplanets orbiting the pulsar PSR B1257+12[1]. Lee et al. (2009) used the eclipse-timing method to detect two circumbinary exoplanets orbiting the binary HW Vir (AB). These were the first exoplanets detected by this method. The transit-timing method became feasible with photometric data covering several years from the Kepler space mission (chapter 1.3.2). Ballard et al. (2011) calculated from transit timing variations of the transiting planet Kepler 19 b the presence of a second companion. Up to now, about 20 planets are discovered by timing methods (exoplanet.eu, Schneider et al. 2011).

1.2 Radial velocities

The reflex motion of a star around the star-planet barycentre can be used to detect an exoplanet. It can be used by measuring the angular displacement via astrometry or by measuring the radial displacement via timing. The radial part of the reflex motion can be measured, even if a source does not exhibit a timing effect. Radial velocity (RV) measurements are based on the Doppler shift of stellar lines, while the star changes its velocity. The light from a star that recedes from the observer appears to be red shifted. Light from an approaching star appears to be blue shifted. In its non-relativistic form, the Doppler effect can be calculated by the simple formula: $\Delta\lambda/\lambda = v/c$, where c is the speed of light, λ the emitted wavelength, $\Delta\lambda$ the measured Doppler shift and v the corresponding velocity. The effect is

---

[1]The rotation period of this neutron star is $6.2\,\text{ms}$.

already used for more than 100 years to measure the velocity of stars. Following Doyle (2008), I will summarise its application as detection method for exoplanets. In contrast to binary stars, the mass ratio between an exoplanet and its host star is extreme. Therefore, the actual challenge is the expected extremely small semi-amplitude (K) of the reflex motion:

$$K = \left(\frac{2\pi G}{P}\right)^{1/3} \frac{M_P \sin i}{(M_P + M_\star)^{2/3}} \frac{1}{(1 - e^2)^{1/2}}. \tag{1}$$

Here P is the orbital period, e is the eccentricity of the orbit, and G the gravitational constant. Since only the radial part of the movement is measured, the factor $\sin i$ counts the angle of the orbit inclination i. The inclination is the angle between the orbit plane and the reference plane on the sky. The mass derived from timing and the RV-method, therefore is a minimum mass and will be equal to the real mass if i is $90°$. The orientation of the orbital plane is then called "edge-on".

The semi-amplitude for Jupiter would be 12.5 m/s in about 12 yr. The Earth would cause a variation of 0.1 m/s in its 1- yr orbit. Such extreme accuracies for a time of several years made it necessary to develop new, very stable instruments (see section 1.2.1), as well as observation programs with long time series. The first planets detected by this method were massive companions like HD 114762 b, a planet with $M_P \sin i = 11\,M_{Jup}$ (Latham et al. (1989)). Mayor & Queloz (1995) published the first detection of a sub-Jupiter mass companion orbiting the solar-type star 51 Peg. The planet has a minimum mass of $0.45\,M_{Jup}$, which was re-calculated by Martins et al. (2015) using data from different observatories of 20 years of observations. The most interesting part of this discovery was the orbit period of just 4.23 days. For several years, the existence of close-in massive planets, so-called Hot Jupiters, was questioned since those were not known from our Solar System. In the following years, the RV-method became very successful in detecting Hot Jupiters and deriving their minimum masses. Hot Jupiters were found first, since their K is relatively large compared to planets in long period orbits. Nevertheless, not only close-in planets have been observed. A prominent example for a non-close-in planet is the $2.3 - M_{Jup}$ planet of β Gem (also known as Pollux) in a 590 d orbit. The discovery was confirmed by Hatzes et al. (2006), by using an immense dataset with 25 years baseline. Several long term planet search programs are ongoing to find long period planets. The CORALIE planet search program (Marmier et al. 2013) focuses on 822 solar-type, main-sequence stars within 50 pc in the southern hemisphere. With a time span of almost 16 years in this survey, planets with long periods of up to several years were detected. The McDonald Observatory Planet Search programme focuses on several hundred stars for almost 30 years (Endl et al. 2016). At the time of writing, exoplanet.eu (Schneider et al. 2011) lists 454 planetary systems detected with the RV-method. Among them 109 planetary systems with two or more planets have been detected so far.

1.2.1 High-resolution spectrographs

High-resolution spectra are obtained using Échelle spectrographs. Following Schroeder (1967), I give a short outline to the principle of such a spectrograph.

An Échelle spectrograph uses a blaze grating. These gratings can be described as tilted mirrors. The tilt is called the blaze angle. Usually it is used in a configuration such that

the angle of incidence is equal to the blaze angle (θ_0), the so-called Littrow mounting. In this configuration, the angular resolution and the resolving power increase with the angle of incidence. As a consequence the grating has to provide a high diffraction order to reach a high resolution. In contrast to conventional gratings, a blaze grating has the advantage that the largest maximum flux is not in the zeroth order, but shifted to a higher order. The blaze angle for a specific wavelength λ can be calculated by the grating equation:

$$\theta_0 = \arcsin \frac{m\lambda}{2d}, \tag{2}$$

with m being the diffraction order and d the groove separation. A typical blaze angle for λ = 5000 Å, $1/d$ = 30 lines/mm, and m = 120 is around 64°. The blaze angle does not work only for this one wavelength. Since at high orders all wavelengths are diffracted to almost the same angle, the grating works effectively over a large range of wavelengths. High diffraction orders always overlapp, thus, a cross-dispersion element (often a grating) is used to separate the orders again. The higher the order, the smaller is the wavelength coverage in a single order. The so-called free spectral range ($\delta\lambda$) can be calculated by λ/m. It gives the separation between two wavelengths in adjacent orders that are diffracted to the same angle. The final cross-dispersed two-dimensional spectrum resembles a ladder (French: échelle), which gives the name to the spectrograph's design. A further advantage is the usually rectangular shaped CCDs can, therefore, perfectly be used in a very efficient way. To calibrate optical Échelle spectra, commonly Thorium-Argon (ThAr) hollow-cathode lamps are used. The line positions of the emission lines of these lamps are well known from laboratory measurements and are published for example by de Cuyper & Hensberge (1998). To achieve a high accuracy, calibration frames can be taken before and after each spectrum. Changes of the position of the wavelengths, for example due to temperature drifts during the exposure, can be determined and corrected. Even higher precision can be achieved with the simultaneous exposure of a calibration lamp (Baranne et al. 1996) or with the iodine-cell method (Marcy & Butler 1992). In the latter, a cavity filled with iodine gas is placed directly in the path of the light and, thus, absorbs the star light. These artificial absorption lines and their positions with respect to the stellar lines can be measured with very high precision. The iodine-cell method can be used for solar-type and late-type stars with sharp lines and allows accuracies in the order of m/s.

Another factor influencing the RV-precision is the stability of the spectrograph. A spectrograph mounted directly on the telescope is not stabilised in temperature, pressure, and mechanical deformations. The most stable spectrographs up to now are the two High-Accuracy Radial velocity Planetary Searcher (HARPS) instruments (HARPS at La Silla and HARPS-N at Roque de los Muchachos). Both instruments are temperature and pressure stabilised by operating them in vacuum. The light from the telescope is coupled via optical fibres. Two spectrograph arms offer a wide usable spectral range of about 3000 Å and a high resolution of R $\sim$ 115 000. Mayor et al. (2003) found empirically an RV-precision of 0.2 m/s for the instrument. Nevertheless, they concluded for exoplanet research of solar-type stars that the minimum noise level is about 1 m/s due to stellar activity and pulsations.

1.2.2 Deriving the mass from RV-measurements

Assuming that the object is orbiting the star in an elliptic orbit (described by Kepler's law), it is possible to calculate the orbit and the projected mass of the object. If close-in companions have circular orbits, the RV-data can be phase-folded by the transit period and fitted with a sinusoidal function. The semi-amplitude (K) of the fitted function can directly be translated to the projected mass of the planet. Nevertheless, especially if the objects are young, their orbits may be not circular. In this case all parameters of an elliptical orbit have to be calculated and fitted to the data.

The orbital equations for keplerian orbits can be found in Perryman (2011). In the following, I summarise the necessary equations to calculate the velocity in the line of sight. To describe the movement of the planet along the orbit, time-depended angles have to be considered. The first angle is the true anomaly (ν), the angle between the direction of pericentre and the position of the planet, seen from the barycentric focus of the ellipse. ν can be written as

$$\nu = 2 * \arctan\left(\left(\frac{1+e}{1-e}\right)^{1/2} * \tan(\frac{E}{2})\right) \tag{3}$$

with (e) being the eccentricity of the orbit and (E) the eccentric anomaly. E is the second angle and refers to an auxiliary circle with the radius of the semi mayor axis. It is determined by a line through the position of the planet perpendicular to the mayor axis that intersects the auxiliary circle. The Eccentric anomaly is the angle between the direction of pericentre and the intersect point.

The third angle is called mean anomaly (M). It refers to a fictive body that moves along the auxiliary circle with constant angular velocity. M is defined as the angle between the direction of the pericentre and the position of the fictive body on the circle. Since this is a simple trigonometric problem, the angle is given by

$$M = \frac{2\pi}{P}(t - t_p) \tag{4}$$

with (t) being the time, (t_p) the time after the pericentre passage, and (P) is the orbit period. It is connected to E via Keplers equation:

$$M = E - e\sin(E). \tag{5}$$

The radial velocity in the line of sight can be derived by determining the position of the object in the plane of the observer and calculating its velocity afterwards. In this plane, three angles are representing the movement of the planet in respect to a reference frame projected on the sky and centred in the barycentric focus. The longitude of the ascending node (Ω) is the angle between the reference frame and the position of the planet when it intersects the reference frame heading away from the observer. (ω) is the argument of perihelion that describes the angle between the pericentre and the ascending node in the orbital plane. The angle between the orbital plane and the reference frame (i) is the inclination of the orbit. The solution for the velocity in the line of sight (v_r) is

$$v_r = v_{r0}K(\cos(\omega + \nu) + e\cos(\omega)) \tag{6}$$

with (K) is the semi amplitude of the radial velocity and v_{r0}, a constant offset. From the parameters P, K, e, and $M_\star$ the mass of the companion (M_P) can be calculated by using the formula (1).

1.3 The transit method

A transit occurs if a planet revolves around its host star and crosses the line of sight between the observer and the stellar disc. Figure 1.1 shows the principle. Numbers indicate (1) the first contact, when the planetary disc starts to occult the star, (2) the second contact, when the complete planet is in front of the star. (3) and (4) are the reverse situations.

Transits are only visible if the inclination i of the orbit fulfils the simple geometric condition: $\cos i_{min} = (R_\star/a)$, where $R_\star$ is the radius of the star and a is the semi-major axis.

For example, given the semi-major axis of Venus and the Sun, this minimum inclination can be about $89.646°$. Following Borucki & Summers (1984), the probability that a star with an exoplanet also exhibit a transit is $p = R_\star/a$ if the inclination is oriented arbitrary. For example, the probability to detect an Venus-like exoplanet is only 0.7%.

Figure 1.1: Geometric view to a planetary transit (from Winn (2009), Figure 1).

Otherwise, to detect an exoplanet similar to 51 Peg b it is already about 11.4%. If a planet transits, it occults a part of the stellar disc, leading to a decreased stellar flux. The maximum change in flux is directly proportional to the covered area

$$\Delta F \simeq \left(\frac{R_P}{R_\star}\right)^2,$$

where R_P is the radius of the planet. The transit depth gives a direct measure for the relative size of the planet or even of its real size if the size of the host star is known. Depicted in Figure 1.2 is the result of this dependence for planets with a given size orbiting host stars of different spectral types. The green line shows that a planet of the size of Jupiter orbiting the Sun would show a transit depth of 1%. A 1% deep transit detected around an M0 V star would correspond to a 0.5 Jupiter-radius planet. Despite the transit depth, four other important variables can be obtained from the transit: the inclination i, the period P, the transit time between the first and fourth contact t_τ, and the time between second and third contact t_F. If the planet is fully transiting the stellar disc, between the second and third contact an almost flat bottom is observed. During this time, the covered area stays the same. Therefore, this flat bottom is not visible if the planet only partially transits the stellar disc. Deviations from the transit-shape have their origin typically from intensity variations on the stellar disc. For example, limb darkening plays an important role in the shape of a transit
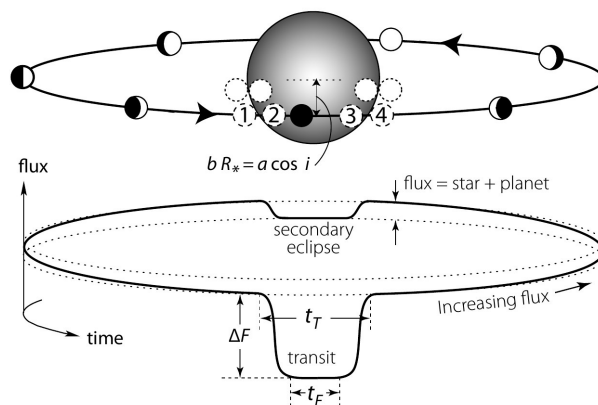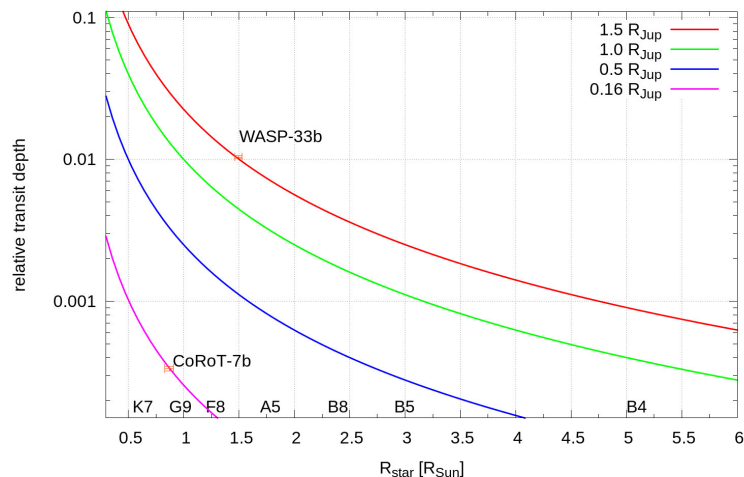
Figure 1.2: Transit depth of a planet with given size for different spectral types of the host stars.

(Mandel & Agol 2002).

First surveys to detect transits concentrated on stars with a previously known planet discovered by the RV-method. The first exoplanet observed during a transit was HD 209458 (Charbonneau et al. 2009). The orbital period of 3.5 days is almost the same as for the first published exoplanet 51 Peg b (orbiting a solar-type star). As well as the radial velocity technique, the transit method is sensitive to planets with short periods as the observation time is limited. The shorter the period, the more often a transit occurs and the higher is the probability of a discovery. Furthermore, Brown (2003) calculated that for close-in planets, like HD 209458 b, the detection rate is about several planets per 10^4 observed stars. This fact leads to the conclusion that many stars have to be observed for a relatively long time span to effectively detect transiting exoplanets.

1.3.1 Surveys from ground

From the ground, several wide angle transit searches have been developed during the past years. One is the Hungarian Automated Telescope project (HATnet, see Bakos et al. (2009) for a description). Seven telescopes are working from various locations in the world, which provide an almost uninterrupted time coverage. Each telescope has a broad field of view (FOV) of $8° \times 8°$. This leads to a relatively large sky coverage. The Wide Angle Search for planets (SuperWASP, Pollacco et al. 2006) uses also optics with a FOV of $8° \times 8°$. But in this case, eight of them are put together on one mount, reaching a sky coverage of about 482 square degree. Two facilities of this type are in operation. One is located on the island of La Palma and one in South Africa to cover the northern as well as the southern hemisphere. Yielding 66 and 103 discoveries respectively, HAT and SuperWASP are the most successful ground-based programs up to now (exoplanet.eu, Schneider et al. 2011). Ground-based surveys like SuperWASP reach a photometric precision of about 1% (Christian et al. 2005). This is sufficient to detect Jupiter-like planets orbiting solar-type stars. For a given field of view, these surveys can detect all transiting close-in (a < 0.1 AU) Jupiter-sized exoplanets. Considering the geometric probability, this is 10% of the complete

population of these planets in these fields. The Next Generation Transit Survey (NGTS, Wheatley et al. 2014) is operated at Cerro Paranal in Chile and will provide a photometric precision of about 0.1% in a field of view of 96 square degrees. This sensitivity will give the opportunity to find and characterise Neptune-sized planets from ground.

1.3.2 Space missions

Space-based transit surveys offer the possibility to observe continuously unaffected from weather and the Earth's day-night cycle. Furthermore, the missing influence of the turbulent Earth atmosphere raises the sensitivity and allows the instrument to detect shallower transits than from ground.

CoRoT: The first space mission dedicated to transit search of exoplanets was CoRoT (Baglin et al. 2002). It was designed to search for stellar oscillations as well as for transits. The acronym stands for COnvection, ROtation and planetary Transits. It orbits Earth in a polar orbit with 896 km height, leading to an orbital period of 1 h 43 min (Boisnard & Auvergne 2006). On this orbit the satellite is capable of observing a single field uninterrupted for about 152 days, until the sunlight leads to an increase of stray light. Thus, most pointed observations were done in two opposite and almost circular regions with 10° radius each. One is near Aquila [18h50m], the other is near Monoceros [6h50m], also called "centre" and "anticentre", respectively.

CoRoT was in operation from 2007 until October 2012 and equipped with a 27-cm telescope. It reaches a photometric accuracy of better than 10^{-3} for an R=15 mag star within two hours of observations. The satellite was equipped with four CCD detectors in the focal plane. Two detectors were dedicated to the analysis of bright ($V < 8\,mag$) stars in order to analyse stellar pulsations (Moutou et al. 2013). The other detectors were dedicated to the search for transits (the so-called exofield). As shown in Figure 1.3, a prism was installed in front of the focal plane to disperse the starlight of the stars into spectra.

The downlink rate did not allow to transmit complete images. After each new pointing, one image was completely downloaded and used to define a numerical mask (an area of the detector, dedicated to the dispersed image of each selected star). This mask depends on several factors, like the brightness and the colour of each target. Within a chromatic mask, the dispersed image of a star was assigned to three different colours and integrated by the on-board software separately. In this way, three coloured light curves of the brighter stars ($V < 14.5\,mag$) were obtained. For the faintest stars, the complete mask was integrated, yielding only monochromatic light curves. The light curves were pre-reduced using the on-board software and sent down to Earth. Only from the brightest stars, the single frames were transmitted to Earth. This
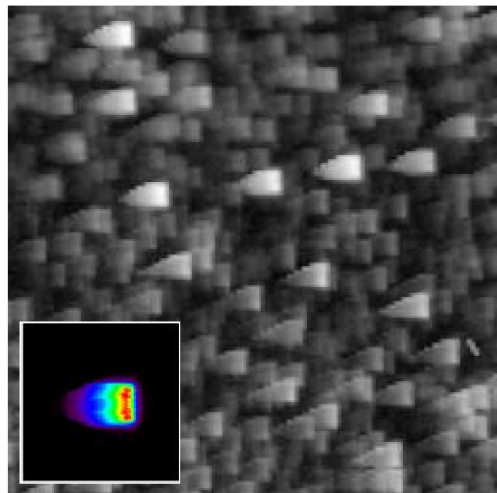

Figure 1.3: Simulation of the signal obtained from the exofield. The inlay shows the dispersed star in colours (Image from Boisnard & Auvergne (2006), Figure 23).

allowed a dedicated and more precise reduction. For each CCD, up to 5640 stars in a field of $1.4°$ x $1.4°$ were observed. The time sampling-rate was typically $32\,s$.

Due to the limited transfer rate, only 500 targets could be downloaded with this full sample-rate. The other stars were binned to a sampling-rate of $8\,min$ before transmission. The decision, which stars were transferred in the original time-resolution, was done by the ground team. Until October 2012, 163 664 stars have been monitored with an average run duration of 78 days. A total of fifty-eight square degrees have been covered in 26 different runs (Moutou et al. 2013). In the two fields, so-called long-runs were done with observations of about 150 days. In the phase between the long-runs, so-called short runs of several days were carried out, to point on interesting regions. At time of writing, 27 CoRoT objects were published, among them two brown dwarfs and the first rocky planet CoRoT 7b (Léger et al. 2009).

Kepler: Another very important space mission dedicated to transiting exoplanets is the Kepler satellite. It was launched into an Earth-trailing heliocentric orbit in 2009. Such an orbit has the advantage that disturbing effects from Earth, like radiation belts, illumination, and heating, do not affect the observations (Koch et al. 2010). It yields a higher photometric accuracy than CoRoT because of its $0.95\,m$ aperture. The initial mission concept was to observe a single field of $16°$ in diameter for 3.5 years. The field was located in the constellations Lyra and Cygnus [$19\,h\,22\,min$; $44°\,30'$]. As well as the CoRoT mission, the Kepler mission was extended and Mullally et al. (2015) reported a list of 7348 planet candidates after the analysis of 47 months of continuous observations. After two reaction wheels of the satellite stopped working, it was no longer possible to keep the accurate pointing on the original field. Howell et al. (2014) described a new operation method in which the two remaining reaction wheels can compensate the force produced by solar pressure on the Solar array if the telescope is pointing into the ecliptical plane. Additional corrections to the pointing are done using the thrusters. This new operation method allows a less precise pointing than achieved in the original mission. Nevertheless, the K2 mission offers 75 days of uninterrupted observations of different fields in the ecliptic plane. This allows astronomers to observe a wide range of astronomical targets, like cluster, galaxies, or young stars. The target selection is done through an open call for proposals from the community.

1.3.3 False alarms

One problem of transit searches are the so-called false alarms (Brown 2008). Typically, eclipsing binaries can produce transits that can be misclassified as planetary transits. It is possible to distinguish these different types of objects just from the transit light curve. Eclipsing binaries have often a larger radius than transiting planets. In contrast to a transit due to a planet, this translates into a longer eclipse time, a deeper eclipse depth, and often to an eclipse that is V-shaped. A V-shaped eclipse occurs if one star is from our point of view not totally in front of the other, but just a part of the eclipsing star is seen. This effect, also called a grazing eclipsing binary, does not show a flat bottom, but leads to a triangular transit shape, which can be detected easily. Most of the eclipsing binaries can also be identified, by the presence of a secondary eclipse. In contrast to a companion star, a planet does not show an obvious secondary transit if its host star occults it. An eclipsing binary can therefore

mimic a planet-like transit curve if the secondary eclipse is not visible. This is for example the case if the system is grazing, or if the companion star is very faint. Another aspect are interactions between the stars like tidal distortions, gravity darkening, or radiative heating that induce sinusoidal patterns in the light curve with the same period like the orbit or with an integer part of it. Close-in planets are rarely not massive or hot enough to produce these effects. However, by analysing very precise light curves from space missions, such effects were also detected for very massive planets (e.g. Mazeh et al. 2012).

A more complicated candidate for a false alarm is a bright star with a faint binary system in the background. Such a configuration can mimic a planet-like transit due to dilution of the eclipse depth by the brighter star. Transit surveys have mostly low spatial resolution because of the large field-of-view that is observed. Multi-colour photometry with high resolution can identify such configurations if the binary has a separation of several arcsec. When the transit time is well determined, it is sufficient to take one exposure within the transit and one out of the transit. By comparing the two observations, it is easy to exclude nearby eclipsing binaries, since the binary system would show a decreased brightness of several percent. In the case of a faint system, the binary cannot be detected anymore. This observation-method is called on-off photometry and is used in the follow-up programme of the CoRoT group (Deeg et al. 2009).

Faint background objects within 1 to 2 arcsec can be found by using adaptive optic (AO) systems as explained in Guenther et al. (2013). If the system is a close binary or a hierarchical triple, it is only possible to resolve the components if they are close by. For the most of the CoRoT and Kepler targets that are in distances of about 1 kpc, such a configuration would exhibit separations in the order of 0.1 marcsec and thus cannot be resolved anymore.

If, in case of a triple system, the bright star and the eclipsing binary have different colours, photometry in different wavelength areas (multiband photometry) might show changing transit depths in different colours. This observation can explain the nature of the system and rule out an false alarm. Therefore, the CoRoT satellite was designed to observe in three different colours. An effective test is described by Seager & Mallén-Ornelas (2003). They showed that the transit shape is related to the density of the host star. This can be used to directly rule out the host star as a giant. Furthermore, this density can be compared with the density of the host star, calculated by comparing its spectrum with stellar models. A strong discrepancy gives a strong hint for a stellar companion. If these tests do not show any hint for an eclipsing binary, the probability increases that the observed transit origins from is a planetary transit.

The transit method is usually combined with radial velocity measurements. Low-precision RV-measurements allow us immediately to exclude stellar companions that would show a reflex motion with an amplitude of several kilometres. The importance of a careful investigation is shown in Mandushev et al. (2005). After passing all tests and detecting a reflex motion consistent with a brown dwarf companion with $\sim 32\,M_{Jup}$, they discovered that it was indeed a hierarchical triple system of stars. A triple system with a fast rotator ($v\sin i_\star \approx 34\,km/s$) and a fainter eclipsing binary with a reflex motion within the amount of the rational speed of the fast rotator. This leads to small planet-consistent RV-variations in velocity due to line profile variations over the orbital period. These line profile variations were finally discovered by investigating high-resolution spectra, proving the brown dwarf as a false alarm.

1.4 Planets of solar-like stars

Planet search programmes are normally biased in favour of main-sequence stars with masses from 0.9 to $1.3\,\mathrm{M}_\odot$. One reason is that the RV-velocity of main-sequence stars is spectroscopically easy to measure. Therefore, the programmes concentrate specially on stars that rotate slowly, are not part of binary systems, and show low chromospheric activity (Marmier et al. 2013). But more important: these stars are solar-type stars. With more and more sensitive instruments, one goal for planet search programs is to find a planet in the habitable zone of the host star. The habitable zone is defined as the region around a star, where a terrestrial planet with CO_2, N_2 or H_2O atmospheres would receive enough energy from its host star to generate temperatures that allow the maintenance of liquid water on the surface. When the planet is closer to the host star, the water is lost due to the stellar radiation. If it is further out, the formation of high- albedo cloud layers is favoured and leads to a further cooling of the atmosphere (Kasting et al. 1993). The detection of a planetary system analogue to our Solar System, with at least one Earth-like planet in the habitable zone, would answer the question whether our Solar System is unique or not. The properties of planets and planetary systems found at solar-type stars are very different from our Solar System. Surprisingly, the first planets orbiting solar-type stars, like 51 Peg b, were hot Jupiters. About $1\,\%$ of all solar-type stars harbour hot Jupiters (Cumming et al. 2008). RV surveys with several years baseline also detected Jupiter-mass planets in distances of one to several AU, but often found high-eccentric orbits (e.g. Marmier et al. 2013). Nevertheless, the sample is not complete. The reason are selection effects: planets that are easier to detect were found first. Furthermore, all surveys have detection limits. Below these limits, planets cannot be found and close to those limits, not all planets are detected. Nevertheless, low-mass planets with masses smaller than $30\,\mathrm{M}_{Earth}$ (so-called "mini Neptunes"), as well as planets with masses smaller than $10\,M_{Earth}$ have been found. The latter are so-called "super Earths". With CoRoT 7b, the CoRoT team announced the detection of the first planet with a density comparable to that of the terrestrial planets in our Solar System (Léger et al. 2009). Hence, their planetary composition has to be rocky. At the time of writing, the latest discovery of a transiting rocky planet was reported in the planetary system of HD 219134b. This transiting planet is special, because its host star has an apparent magnitude of V=5.5 mag (Motalebi et al. 2015). Planets of relatively bright stars allow a wealth of follow-up observations. In-transit-spectroscopy can shed light into the physical properties of the atmosphere like composition and temperature distribution.

From the statistics of the planet candidates published by the Kepler team we know that small planets or even rocky planets are more frequent than Jupiter- or Neptune-sized planets (Dong & Zhu 2013). The region of planets with the masses of Mercury and Earth further out than $0.3\,\mathrm{AU}$ is currently not explored since the detection methods are still not sensitive enough in this regime (Rauer et al. 2014). To characterise the properties of all discovered planets, two parameter-spaces are typically analysed (Mordasini et al. 2015). One is the semimajor-axis-mass (a-M) diagram as shown in Figure 1.4 (a). Planets can be easily divided in several groups: There are (i) the massive close-in planets that were discovered first, (ii) the close-in planets with masses from $1-30\,M_{Earth}$, the super Earths or mini Netpunes, and (iii) the long periodic Jovian planets. In the mass regime of about $40\,M_{Earth}$ there is still a lack of discovered planets, the so-called "planetary dessert". From the planets discovered
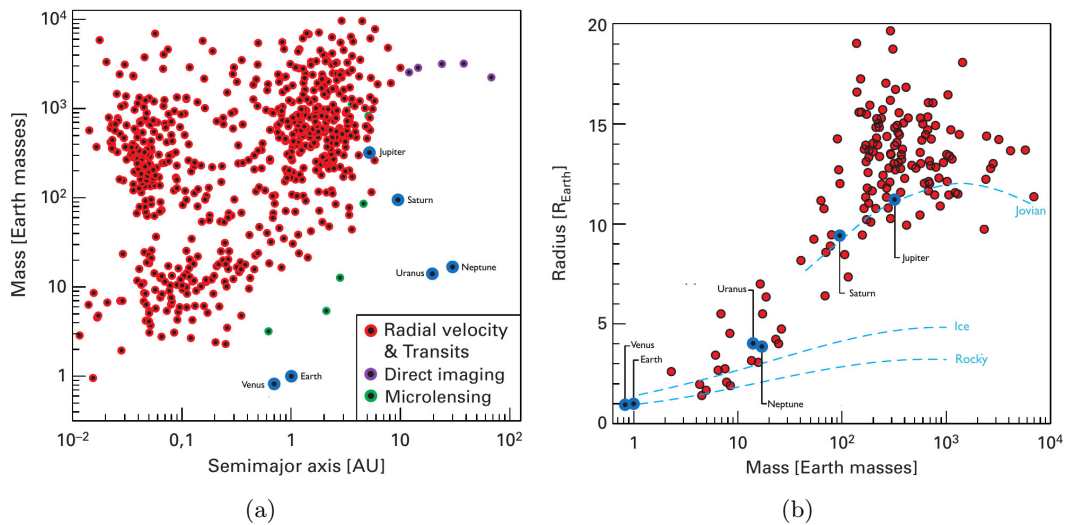
Figure 1.4: Detected exoplanets up to now: (a) a-M diagram of exoplanets detected with different techniques; (b) M-R diagram. The blue dashed lines indicate the theoretical M-R relation for different compositions of the planets (from Mordasini et al. 2015), Figure 1 and 2).

by direct imaging, the intrinsic brightness and temperature can be measured. Their masses are derived from evolutionary models (e.g. Marois et al. 2008). The second diagram is the mass-radius (M-R) diagram that became possible by combining RV- and transit methods. As shown in Figure 1.4 (b), the planets can be split in different groups, according to their composition. There are (i) heavy Jovian planets with an extended H/He atmosphere, (ii) rocky planets with a similar composition of our Earth, and (iii) icy planets with a similar composition to Neptune or Uranus. Deviations from the planets of our Solar System show new classes of planets. Jovian planets with extremely extended atmospheres or a group of H/He planets with extreme low density are perfect examples for that. This groups help to discuss the composition of exoplanets, but is not a definitive marker for several groups. For example, the planet GJ1214b is according to its composition between an ice giant and a terrestrial planet and, therefore, hard to classify. The analysis of planetary compositions is a very young field within the field of exoplanets and will benefit from new generations of instruments, like the European extremely large telescope (E-ELT, Udry et al. 2014).

1.4.1 Planet formation

The discovered planetary systems show a wide diversity. Most of the surveys up to now are not sensitive enough for planets with wide orbits, like Uranus and Neptune as well as for low mass objects, like an Earth around a solar-like star. Thus it too early to conclude our Solar System would be unique. Nevertheless, we can learn much about the extreme, since they challenge the theories of planet formation. Specially those that are based solely on the properties of our Solar System.

Mordasini et al. (2015) describe the use of planetary population synthesis. This method assumes that the physical processes in the planet formation are always the same, but that the initial conditions are different for each system. Therefore, they use statistical constraints to estimate the initial conditions of the planet formation, like the mass of the protoplanetary disc, dust-to-gas ratio of the disc, or lifetime of the disc as input for a global model containing

the general physics of planet formation. This general physics contains the formation of planets from a protostellar disc. Such discs formed around the evolution of a young star due to the infall of material from the initial gas cloud by conserving its angular momentum. One model to form planets from a disc is gravitational instabilities in the disc (Boss 1997). It predicts the rapid formation of Jovian planets without the presence of rocky cores. A competing and widely used model is the so-called core accretion theory (Kokubo & Ida 2002). This theory assumes that solid cores grow within a disc first and develop rocky cores that accrete gaseous envelopes from the gas in the disc. Terrestrial planets can be explained in this model due to the loss of there initial atmosphere due to stellar irradiation.

A challenge for these theories is the presence of close-in Jovian planets. It is supposed that they are formed further outward in the disc. As a consequence, mechanism to explain the change of the radial position of the planet is needed, i. e. the question has to be answered how it could be possible for the planet to migrate inward. The classical explanation is disc migration due to the gravitational interaction between gas and dust in the disc and the planets within the disc. A planet loses angular momentum due to torques that transfer angular momentum to the disc. Two types of migration are discussed: in type I migration the angular momentum transport due to the planet is smaller than the viscous angular momentum transport in the disc. Therefore, the surface density is not disturbed. Type II migration occurs if the planet mass is higher than the local disc mass. The planet then forms a gap in the disc. Still, torques transport angular momentum to the disc. Depending on the amount of angular momentum that is transported to the outer or the inner disc, the planet further migrates inward or even outward. Both types of migration work only if a protoplanetary disc exists. If the disc disappears in the further evolution of the planetary system, the disc migration stops. Another process to create close-in planets is planet-planet scattering followed by tidal circularisation. Tidal circularisation is already known to produce circular ($e = 0$) orbits of close-in massive binary stars within a time scale of about 10^6 yr (Beech 1987). For planets in close-in orbits, this time scale can be about 10^8 yr (Rasio & Ford 1996).

One important output of these models is the initial mass function of exoplanets. This mass function would help to shade light on how many planets form within a certain mass bin. Interesting to note is that the planetary dessert at about $40\,M_{Earth}$, already shown in the observed a-M diagram, can be reproduced by population synthesis. The physical explanation is that a planet in this critical mass regime starts a run-away accretion of gas in the protoplanetary disc. This critical core mass is about $15\,M_{Earth}$ (Mizuno et al. 1978), hence the critical mass is about $30\,M_{Earth}$ including the envelope. Such planets evolve quickly to planets with a mass of $100\,M_{Earth}$ and more (Mordasini et al. 2015). This fact explains the lack of planets in this mass regime.

1.5 Planets of non solar-like stars

Non-solar type stars have largely been ignored by planet searches, but these stars can also give us information about planet formation. For example, stars with very low masses, the so-called late-type stars, are the most abundant stars in our galaxy. If they frequently harbour planets, the properties of those might give us insight in the most common types of planets in

the galaxy. More massive stars with intermediate masses of 1.3 to 2.1 $M_\odot$ are much younger than most solar-type stars. Therefore, these massive stars harbour relatively young planets. The analysis of planets of non solar-like stars offers unique opportunities to test predictions made by theories of planet formation and evolution.

1.5.1 Low-mass stars

Low-mass planets, like Super-Earths, are difficult to detect if they orbit solar-like stars. Their induced RV-amplitudes are about several cm/s and therefore far below the limit for the RV-method (see chapter 5). Nevertheless, the study of low-mass planets in the habitable zone around their host stars is of fundamental interest in the goal to understand the evolution of our planet. Late-type main-sequence stars seem to be the best candidates to find and analyse such planets. First, Kepler data indicate a much higher abundance of small planets around low-mass stars. That means, it should be feasible to detect such planets even if the number of stars that can be studied is in the order of 1000 (Alonso-Floriano et al. 2015). This low number is caused by the fact that only the closest stars of this type can be observed at all, since the luminosity of such stars is much smaller than that of a solar-type star. Second, as described in section 1.3, the transit signal of a small planet can be detected easier. This is because of the dependence of the transit depth from the ratio of the sizes of both objects. For main-sequence stars with masses smaller than one solar mass, the mass-radius relation can be written as R $\sim$ M (Torres et al. 2010). Thus, low-mass stars have much smaller radii than solar-like stars. Third, due to the small luminosity, the habitable zone is much closer to the star than for a solar-like star. Furthermore, the mass of a late-type star with about $0.1\,M_\odot$ is much smaller than that of a solar-like star. In short, a planet with similar size and mass as our Earth in the habitable zone of a low-mass star would have the following characteristics: It would orbit close to its star and induce one order of magnitude stronger RV-amplitudes, and deeper transits than an Earth-like planet in the habitable zone of a solar-type star.

Since late-type stars, like M dwarfs, reach their maximum intensity in infra-red wavelengths, high-resolution infrared spectrographs, like the "Calar Alto high-Resolution search for M-dwarfs with Exoearths with Near-infrared and optical Échelle Spectrographs" (CARMENES, Quirrenbach et al. 2011), are currently under development and will be used to analyse these stars in detail. These RV-projects will have some overlap in terms of objects with the next photometric satellite mission TESS that will concentrate on transiting planets of solar-type as well as low-mass stars up to spectral type $M5$ (Ricker et al. 2015). Such planets will be analysed as possible locations to harbour life. The discussion about this idea is currently of high interest. Carone et al. (2015) found that a close-in and tidally locked terrestrial planet orbiting an M-dwarf star could exhibit an atmosphere with wind structures that under certain circumstances would support habitable temperatures.

O_2-, H_2O-, and CO_2-rich atmospheres are generally assumed to be biomarkers for potential life on habitable planets. Nevertheless, Tian et al. (2014) calculated that strong FUV radiation from low-mass stars could probably trigger the accumulation of molecular oxygen due to photolysis of O_3, H_2O_2, and HO_2. Thus, a detectable level would produce false biomarkers. We can compare the analysis of these planets with physics of well known particles in extreme environments that will give new clues to their properties. The analysis of such ter-

restrial planets can give us interesting insights in worlds with complex processes that are very different to those on our own planet.

1.5.2 Intermediate-mass stars

Intermediate-mass stars (IMSs) are stars in the mass range from 1.3 to 2.1 $M_\odot$. On the main sequence, these are in the classical MK-system all stars between the mid F stars and early A-type stars (Gray 2005). These stars are of particular importance, because their properties are quite different from those of solar-type stars. Compared to solar-type stars, IMSs have relative short lifetimes. Their typical ages range from 300 Myr for early A stars to 2500 Myr for mid F stars (David & Hillenbrand 2015).

From bisector measurements it is known that the velocity distribution of stellar photospheres changes at late A stars, indicating that the granulation vanishes with increasing temperature. Thus, convection driven stellar winds as well as the amount of coronal radiation is decreasing with increasing effective temperatures (Favata & Micela 2003). Since the generation of a magnetic field is directly coupled with the existence of an outer convection zone (Stix 1989), IMSs have low magnetic fields strengths. An important effect of the stellar magnetic field is its contribution to the decreasing of angular momentum. Stars loose angular momentum via stellar winds. The particles of the wind are coupled to the magnetic field and are forced to rotate rigidly with the star. This process increases the loss of angular momentum and slows down the rotation velocity of the star (Schatzman 1962). Single IMSs rotate typically faster than solar-type stars. This effect is visible in the Cerro Armazonas survey of F dwarfs (Pribulla et al. 2014), where I did the classification of the spectra by comparing them with template spectra (as described in chapter 3). Figure 1.5 shows that for early F dwarfs the maximum rotation velocity is about 10 times higher than for late F dwarfs with a transition near to the spectral type $F6$.
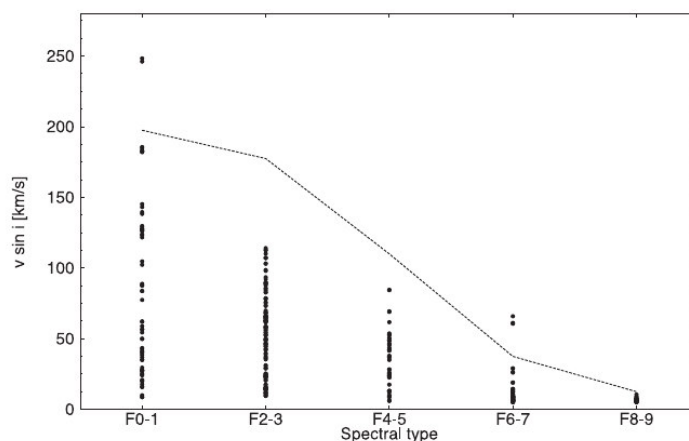
Figure 1.5: Velocities from the Cerro Armazonas spectroscopic survey of F-dwarfs. The line represents the upper envelope of velocities found by Gray (2005). (image from Pribulla et al. (2014), Figure 7)

The fast rotational velocities also have an effect to the spectral lines. Due to the Doppler effect, the lines produced in the approaching part of the star are blue-shifted, while the lines on the receding part are red-shifted. Since a stellar spectrum is the superposition of the disc-integrated light of the star, all velocity-shifted components are combined to the final line

profile. This Doppler broadening also depends on the inclination (i) of the rotation axis of the star. For velocities of more than $v \sin i_\star = 20 \, \text{km/s}$ the rotational broadening plays the major role in line broadening. For IMSs another broadening mechanism plays an important role. It is one kind of pressure broadening that affects the hydrogen lines and is caused by the linear Stark effect. An electric field in the ionised outer zone splits the energy levels of hydrogen atoms and causes a wavelength shift of the lines. The combined distribution of such shifted lines leads to hydrogen lines that are about two orders of magnitudes wider than the metal lines (Gray 2005).

IMSs as pulsating stars

Typically, stars with outer convection layers show solar-like pulsations with periods of about 3 to 15 min and a small amplitude of up to 8 ppm. Since IMSs are supposed to be in the transition regime with a vanishing convection zone with higher masses, such oscillations are observed in the later IMSs. On top of that, many stars show stronger pulsations, such like γ Dor stars. These are early F stars with $M = 1.5$ to $1.8 \, M_\odot$. If the stars have a convective outer layer, they show oscillations with periods of 0.5 to 3 days. The driving mechanism for these oscillations is called "convective blocking" (Dupret et al. 2007). This mechanism starts if the thermal relaxation time at the bottom of the convective envelope is about the same as the pulsation period. The radiative energy from below has to be transported further via convection. If now, due to pulsations, the radiative flux increases and the convective flux-diffusion is not fast enough, the convection layer acts periodically as a blocking layer. This mechanism further supports the instability. In the upper mass regime of IMSs, δ Sct pulsators are common. The pulsation of these stars is driven by the κ-effect in the second zone of partial ionised HeII. The κ-effect is well known from radial pulsation of the Cepheid pulsators. In this case, the opacity increases if the gas compresses and blocks the radiation, until it expands due to increasing temperature again. The pulsation times of theses stars are about 18 min to 8 h. A third group of pulsating IMSs are the rapidly oscillating A_P (roAp) stars. These stars exhibit chemical peculiarities and strong magnetic fields. They pulsate with periods from 5.65 to 21.2 min and magnitudes of about 6 mmag. Late A_m stars were found to be pulsators with low amplitudes, too (Smalley et al. 2011). As for the δ Sct stars, in both cases the driving mechanism is the κ-effect.

Pulsations also induce RV-variations. This is especially true for stars with high degree modes that show nodes within the stellar atmosphere. Since lines of different species are created in different heights, lines that origin from below and above of such a mode line are moving in opposite directions. For example, Kurtz et al. (2005) analysed the pulsating roAp star 33 Lib spectroscopically. With high S/N spectra, they analysed the RV-variations of several elements separately. They found that lines near the node-line of Fe, Cr and Ca show small amplitudes of several m/s. In contrast to lines of H_α, NdII, CeII and SmII that show high amplitudes of about 300 m/s. Since 50% of the late A stars tend to be Am stars, pulsations in IMSs are a rather frequent phenomenon.

Properties of protoplanetary discs of IMSs

From spatial resolved infrared observations of Herbig *AeBe* stars, many discs with a large variety of features have been detected. These stars are known to evolve to normal IMSs (Waters & Waelkens 1998). These discs often show strong evidence for gaps, indicating an advanced stage of planet formation (Menu et al. 2015). The size of the discs increases by one order of magnitude for an increase of the luminosity of the star by two orders of magnitude (Monnier et al. 2009). The time-depended evolution of such discs is driven mainly by accretion. The gas in the disc disperses by photoevaporation caused by the heating of the high energetic X-ray or FUV radiation from the star (Alexander et al. 2014). The disc lifetimes are calculated from Spitzer observations by Mamajek (2009). He finds that the average lifetime for stars with masses $> 1.3\,M_\odot$ is about $1.2\,$Myr. Which is half of the time found for solar-type stars ($2.5\,$Myr).

1.5.3 Massive planets and brown dwarfs

Massive Jupiter-like planets and low-mass stars differ strongly in their inner structure. Low-mass stars are massive enough to enable a stable hydrogen fusion and reach the main-sequence. The minimum mass for this process is M $= 0.075\,M_\odot$ (Baraffe et al. 2002). In contrast massive planets do not initialise a fusion chain at all. If a planet reaches the deuterium-burning mass, it starts to fuse deuterium. Spiegel et al. (2011) found from models that the minimum mass for deuterium-burning is between 11- and $16\,M_{Jup}$. This fusion lasts for less than $1\,$Myrs. Nevertheless, after this time the objects cool down and contract like massive planets. Burrows et al. (2001) suggested to use this mass to distinguish between massive planets and so-called brown dwarfs. This criterion is still subject of discussions. Udry (2010) pointed out, that there is no special feature in the observed mass distribution of planets that would support the importance of the deuterium-burning mass. Schneider et al. (2011) used a mass of $25\,M_{Jup}$ as criterion because of an observed dip in the mass-distribution and mass-radius relationship which implies a different physical nature of planets and brown dwarfs.

Recently Hatzes & Rauer (2015) suggested to distinguish between low-mass planets and high-mass planets from the mass-density diagram by analysing transiting and eclipsing objects with well known mass and radius. The mass-density diagram shows a minimum for $0.3\,M_{Jup}$ and a maximum at $63 \pm 6\,M_{Jup}$ (see Fig. 7.4 in chapter 7). The minimum roughly corresponds to the transition from low-mass and H/He-dominated planets. The maximum corresponds to the boundary between massive brown dwarfs and low-mass stars. According to this new approach all objects that were previously denoted as brown dwarfs are still categorized as planets.

Marcy & Butler (2000) noted that there is a lower frequency of sub-stellar objects with masses between 5-80 M_{Jup}. This so-called brown dwarf desert was observed by radial-velocity studies. During the last years more brown dwarfs have been found and the brown dwarf desert was filled successively. Sahlmann et al. (2011)) found a lower frequency for objects between 25 and $45\,M_{Jup}$. With transit surveys, objects were found in this mass region (Csizmadia 2016). Nevertheless, as showed in the mass-density diagram (Hatzes & Rauer 2015), very few transiting objects were found in the mass-regime between 25 and $60\,M_{Jup}$.

1.5.4   Why are planets of IMSs important?

The fate of planets and brown dwarfs is connected to the evolution of their host stars and the other way around. The best possibility to constrain single questions and to draw a complete picture of planet formation and evolution is to analyse planets of all stages of star formation. The properties of planets of low-mass and solar-type main-sequence stars are discussed above and already well known. But what do we know about IMSs and what can we learn in the context of planet formation?

First, planets can just form as long as the protoplanetary disc exists. It is known that the life-time of a disc of a star more massive than the Sun is on average shorter than that of our Sun. By drawing the frequency of planets over the mass of the host star, one would expect a drop of the frequency at higher masses since the life-time of the disc becomes too short to form planets.

Second, the classical disc-migration can only occur as long as the stellar disc is present. Planet formation theories show that close-in planets exist due to the inward migration of planets that have been formed further away from the star. The frequency of close-in planets can, therefore, provide information about the migration time-scale of the type II migration.

The third point is the evolution of the host star itself. Close-in planets or brown dwarfs will for sure be engulfed by their host star if this star becomes a giant. The existence of close-in objects gives the initial conditions for the possibility whether such objects can change the evolution of the host star if they are engulfed.

The forth point is the possibility to analyse the properties of such planets. For example, the size of the atmosphere can give hints about the effect of stellar irradiation, or the amount of misaligned planets for a certain type of star can either prove stellar formation theories or models of the internal structure of the stars. In the following I will discuss the current state as well as the achievements already reached in these points.

Frequency of planets

RV measurements of IMSs are less accurate than those of solar-type stars due to the highly broadened lines of rapidly rotating IMSs (see chapter 5). Furthermore, the stars often show pulsations that induce RV variations. Interestingly, RV surveys of giant or sub-giant stars were performed to obtain the planet occurrence rate of IMSs.

The reason for choosing those stars is the evolutionary path of a main-sequence IMS towards the horizontal branch phase. The radius of the star increases and the effective temperature drops, changing the spectrum to a late-type G or K giant. The larger radius, as well as the development of a stellar wind that carries away angular momentum result in a slow rotational velocity and thus to sharp spectral lines. More than half of the G and K giants have masses in the IMS-regime or higher. In other words, these are evolved main-sequence IMSs, making them the perfect targets to search for planets of IMSs. Large RV-surveys, like the California Planet Survey, have found an increase of the planet occurrence rate for higher stellar masses, indicating that the frequency of planets for IMSs is $\sim 11\,\%$ and, thus, about twice the frequency of solar-type stars' planets (Johnson et al. 2010). Reffert et al. (2015) recently published the results of a 12-yr survey at the Lick Observatory with a sample of higher-mass stars. They found that the frequency of massive planets increases for higher-

mass stars, supporting previous findings. As shown in Figure 1.6 (a), due to a larger sample in stellar mass, they found a maximum for the planet frequency at $1.9\,M_\odot$, a slow decrease until $2.5\,M_\odot$, a steep decrease with higher masses, and no planets orbiting stars more massive than $2.7\,M_\odot$. They also found that the frequency increases with the metallicity of the star. Planets of A-type main-sequence stars with large orbital separations were found by means of direct imaging (DI) observations. A famous example is the star HR 8799 that yields a system of four planets (Marois et al. 2008). RV and DI surveys give the possibility to compare planets with large orbital separations to planets with small separations. It is interesting to note that by comparing the planet frequencies obtained from RV and DI surveys, Vigan et al. (2012) obtained comparable results of about 10 % for IMSs. Since their DI measurements were precise enough to find planets, they would find all brown dwarfs in wide orbits (5 to 320 AU). Therefore, they concluded that the frequency of brown dwarfs is about 3 % for IMSs. Several additional DI surveys were undertaken in the last years, like the NaCo Large Program (Vigan et al. 2014). They found no further planets, but concluded that their sample was consistent with the previous results. Up to now, DI surveys found seven planets orbiting four IMSs Quanz (2015).
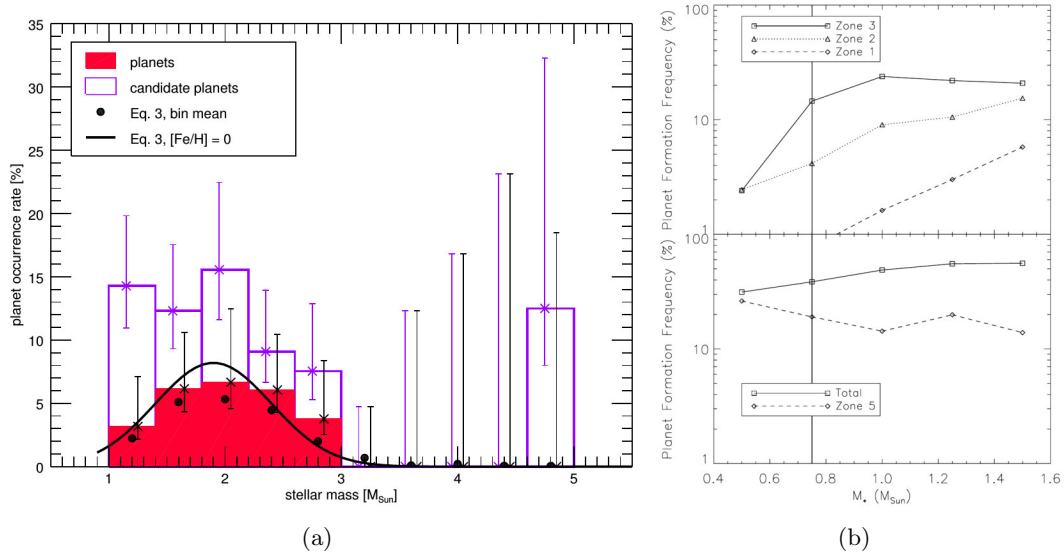

(a)   (b)

Figure 1.6: The frequency of planets over the stellar mass: (a) Observed frequency from RV-surveys. Red boxes: planets, violet boxes: planet candidates. Black line: Fit of all stars with same metallicity to point out the differences due to changing metallicity (from Reffert et al. (2015), Figure 5).; (b) Theoretical frequency of planets in different zones of the a-M diagram. Zones 1 to 4 refer to planets with masses larger than $30\,M_{Earth}$ and increasing distance. So contains zone 1 the hot Jupiters and zone 3 the majority of the RV-planets around 1 AU. Zone 5 refers to the class of close-in planets with lower masses, the hot Neptunes or super-Earths (from Hasegawa & Pudritz 2013, Figure 1).

From a theoretical point of view, Kennedy & Kenyon (2008) calculated the frequency that stars with a certain mass have at least one massive planet. This frequency increases with increasing mass, and they predict a peak around $3\,M_\odot$. However, this model does not include the effects of migration. Alibert et al. (2011) used planetary population synthesis based on the core accretion model. They found that the most important parameters are the properties of the discs of stars with different masses. The distribution of planets predicted by their model is defined if those properties are well known. Based on this model, Hasegawa & Pudritz
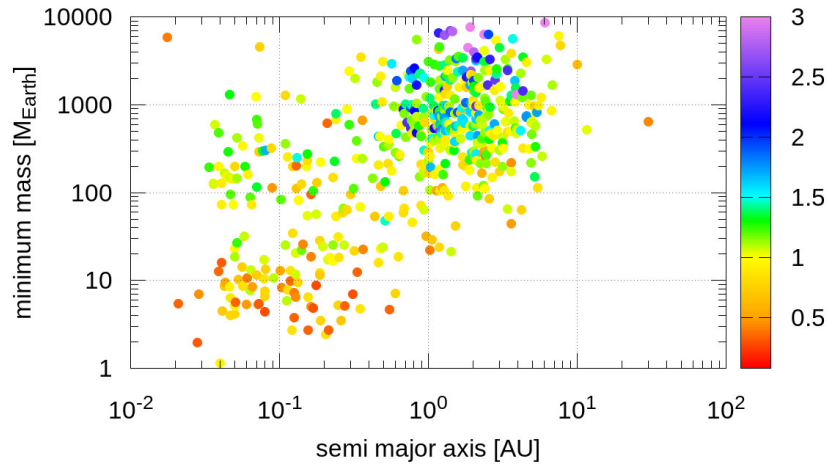
Figure 1.7: a-M diagram of known exoplanets from RV-surveys. The colours indicate the mass of the host star in solar masses. The data were obtained in 10/2015 from exoplanet.eu (Schneider et al. 2011).

(2013) included state-of-the-art properties of stellar parameters, disc parameters, as well as migration parameters. As shown in Figure 1.6 (b), they found that the frequency of close-in planets increases nearly linearly with increasing stellar mass.

Figure 1.7 shows the diversity of planets in the a-M plane for RV-surveys. Blue colours show host stars in the mass regime of IMSs and represent mostly the results from observations of evolved stars. The left part of the diagram represents the close-in planets and will be filled if the population of transit planets is added. But due to selection effects in the current transit surveys that tend to concentrate on solar-like stars, this sample is not representative to compare low- and high-mass stars. Generally, IMSs tend to harbour, first, more massive planets and, second, planets with larger orbital separations compared to solar-type stars. That was shown already by Ida & Lin (2005). Bowler et al. (2010) found that the frequency and mass-period distribution in this group of planets is different from planets of solar-type stars by a 4σ confidence level. The physical effects that cause this observation are widely discussed.

Lovis & Mayor (2007) explained that the larger masses of planets might origin from core-accretion in more massive discs of IMSs. This argument is supported by the observation that IMSs have in fact larger discs than solar-type stars. Nevertheless, Jones et al. (2014) alternatively pointed out that this observation might be biased from the fact that the RV-surveys are based on evolved stars. Planets around these stars might accrete mass from the stellar wind or via direct mass transfer from the host star. The other open question is: What causes the observed discrepancy in orbital separations? Up to now, from all planets orbiting giant stars, only 7% have semi-major axes smaller than 0.5 AU (Wittenmyer et al. 2015). We have to keep in mind that the compared samples of stars have not only different mass regimes, but at least for the planets detected from RV-surveys also different states of evolution.

If the observed discrepancy in orbits is an effect of planet evolution, migration would be on average not efficient enough to produce planets with small separations. In the framework

of disc migration, that might be caused by a stop of migration due to the short lifetime of the disc. Therefore, close-in planets would not form around IMSs, or they are formed with lower probability. Currie (2009) calculated that for IMSs ($M > 1.5\,M_\odot$) the probability to find planets that orbit at larger separations than $0.5\,\mathrm{AU}$ is about $8\,\%$, while the frequency for close-in planets ($a < 0.5\,\mathrm{AU}$) should be less than $1.5\,\%$.

Villaver & Livio (2009) used theoretical models to address the effects of stellar evolution on the distribution of the orbits. They considered the effects applied by mass change of the planet due to accretion of the planet and of the star due to mass loss, tidal forces, and dragging from gravitation and friction. They concluded that all planets that orbit within the maximum stellar radius during the RGB phase will be engulfed. More massive planets are engulfed earlier since they are exposed to larger tidal forces. They found that the stellar evolution can quantitatively explain the observed lack of close-in planets. In 2014, they recalculated these dependencies with current stellar evolution models and the observed eccentricity distribution of the planets. They found that planets orbiting closer than three times the stellar radius experience strong tidal forces once the star leaves the main sequence (Villaver et al. 2014).

This engulfment of close-in planets has strong consequences to the evolution of the star itself. According to Guenther & Geier (2015) (and references therein), I will briefly point out the current picture of planets that are engulfed by their stars. Massive planets or brown dwarfs that survive the common envelope phase lead to the ejection of the envelope. These planets can be observed as companions orbiting the helium-burning cores of former red giants, so-called hot sub-dwarf (sd$B$) stars. Planets with smaller masses will probably evaporate or merge with the stellar core. Single sd$B$ stars and He-rich white dwarfs (He-WDs) are seen as the possible results of such engulfed close-in planets.

Misalignment of planets

Rossiter (1924) and McLaughlin (1924) observed eclipsing binaries spectroscopically. While the eclipse occurs, one of the stars occults a part of its rotating companion. The shape of the broadened profile is changing. Therefore, a RV-shift of the rotating star occurs, even if the profile variation is not resolved. The maximum amplitude of this shift for an edge-on orbit is given by (Perryman 2011):

$$\delta V = \left(\frac{R_{Pl}}{R_\star}\right)^2 * v\sin i_\star \tag{7}$$

with the inclination $i_\star$ of the stellar rotation axis. This effect is called the Rossiter-McLaughlin (RM) effect. It allows one to measure the projected angle between the orbital plane of a companion and the rotation axis of a fast rotating star. This angle is denoted as the obliquity of the orbit. The RM effect can also be used to analyse transiting planets if the host star is a fast rotator. Transiting planets have already been detected around stars with different masses. Winn et al. (2010) analysed the alignment of 28 transiting planets. They found for solar-type stars that planets show on average small obliquities. That means, they are well aligned to the stellar spin. For stars with $T_{eff} > 6250\,K$ (earlier than spectral type $F8$), the planets show a wide spread of obliquities. This is surprising and very different to the planets in our Solar System. What is the fundamental physical effect that causes these high obliquities? Winn et al. (2010) pointed out that the transition from planets with small to high obliquities is at a temperature, where the star stops to have a noteworthy outer convection

zone. One explanation might be that tidal forces from the convective envelope lead to an alignment with the spin axis. These would act as restoring forces to keep the orbit aligned. But which effects cause high obliquities of planets of early-type stars? Candidates for such effects are, for example the gravitational interaction with a third, massive body due to the Kozai-mechanism. This mechanism was discussed for asteroids by Kozai (1962). Nagasawa et al. (2008) showed that the Kozai-mechanism could also explain misaligned orbits of close-in planets if they are the result of planet-planet scattering and tidal circularisation (scattering model). They also predict that the discovery of planets with retrograde orbits would prove the contribution of the scattering model, since disc migration cannot produce them. Nevertheless, Guenther & Geier (2015) state that the scattering model can only be valid if not all planets in a multiplanet system have the same misalignment. That could observationally be proven by measuring the obliquities of a close-in transiting planet as well as a planet in a wider orbit of the same star.

If in such a case all planets would be misaligned, a possible model to explain that is the so-called spin-disc misalignment (Fielding et al. 2015). That occurs in the turbulent environment, where a star is formed. In that model, even retrograde orbits could be explained by disc migration. The misalignment of planets of IMSs is still a topic under discussion.

Another explanation for the high obliquities of close-in planets was discussed by Iorio (2011). He pointed out that fast rotating stars have a certain oblateness due to rotational flattening. That induces a quadrupole mass moment that leads to orbital precession. They estimated that for a close-in planet with a highly misaligned orbit around a fast rotating star, the change in the obliquities due to precession could be in the order of $1.5\,^{\circ}$ per yr.

Since those effects can be proven efficiently by observing close-in transiting planets, every discovered close-in planet orbiting an IMS would help to shed light is this discussion.

Discoveries of transiting close-in planets

From a few discoveries, we know that close-in planets of F and A stars exist. Christian et al. (2006) reported that 1SWASP J022651.05+373301.7 (HD 15082) is an early-type star that shows a transit candidate with a 1.22-d period. It was confirmed by Cameron et al. (2010) to be a close-in planet. This planet is of particular interest in my study, since it is the first close-in transiting planet that has been found orbiting a pulsating, A5-type, main-sequence star. The reduced accuracy of the RV-measurements due to the spectral type (see chapter 5) and the pulsations only allowed us to derive an upper mass limit of $4.1\,M_{Jup}$. Lehmann et al. (2015) used a set of 287 spectra and finally found an orbital solution with a mass of $2.1 \pm 0.2\,M_{Jup}$. Fortunately, the star has an apparent magnitude of V=8.3 mag, thus the planet could be studied with great effort in the past years. Herrero et al. (2011) found that the star shows δ-Sct-like pulsations with an amplitude of 1 mmag. Lehmann et al. (2015) concluded empirically that the density fits well into the density-temperature distribution of close-in transiting exoplanets with masses larger than $1.4\,M_{Jup}$. von Essen et al. (2015) found from infra-red observations of the secondary transit that the planet has an equilibrium temperature of 3358 ± 165 K. This temperature makes it one of the hottest exoplanets known up to now. Cameron et al. (2010) determined an obliquity of about 251°, indicating a misaligned system with a retrograde orbit. Furthermore, Johnson et al. (2015)

found that the projected obliquity has slightly changed from 2008 to 2014, indicating an orbital precession. These measurements can be explained by a precession of the orbit of $0.7 \pm 1.6°$ per yr (Iorio 2016). Further measurements will proof or disproof these results.

Another interesting case is Kepler-13A. The transiting planet orbits the brighter component of a binary of fast-rotating early A-type stars. Szabó et al. (2011) analysed the light curve and found a modulation of the light outside of the transit signal. This modulation is the signature of reflected light from the day-side of the object. They found furthermore that the object is misaligned from the stellar spin, but concluded that it is unlikely a planet due to the transit depth, which would be consistent with a radius of $2.2\,R_{Jup}$. Shporer et al. (2011) and Mazeh et al. (2012) discovered, nearly at the same time, the planetary signal in the Kepler light curve. They used the precise space-based light curve in order to search for the combined effects of reflection, Doppler beaming, and ellipsoidal flux modulations.

Doppler beaming is an effect of the reflex motion of the star. The Doppler shift of the light is usually measured with RV-techniques. Nevertheless, this Doppler shift is also a small shift to its bolometric flux. That leads to a measurable net effect in the stellar brightness and, therefore, in a detectable flux variation (Loeb & Gaudi 2003). Ellipsoidal flux variations are caused by tidal distortions due to the close-in companion. The regions on the star with these tidal waves appear less luminous. This effect is also called gravity darkening and is well known from binary stars (Morris 1985). Since both effects depend on the mass of the planet, the planetary mass can be derived only from these flux modulations. The advantages of this mass-determination are, first that planets can be detected, even if they do not exhibit a transit, and second that this method provides an independent mass determination. For Kepler-13A b, the masses calculated in both papers are comparable with about $8-12\,M_{Jup}$. That makes it to one of the biggest and most massive planets detected so far with a density almost similar to that of Jupiter. More recently, Hartman et al. (2015) published a planet found by the HATnet survey. It orbits the fast rotating $A8$ star HAT-P-57. With a $v \sin i_\star$ of $102\,\text{km/s}$, this star is up to now the most rapidly rotating star hosting a planet. The measured RM-effect indicates a high obliquity of the orbit, although an aligned orbit cannot be excluded. The true obliquity will be derived from further measurements. Its mass cannot be determined from high-resolution spectra, but an upper limit of $M_{planet} < 1.85\,M_{Jup}$ indicates the planetary nature of the object.

2   A Survey for close-in planets of IMSs

Planets of IMSs are at the borders of the known planetary population. The planets found so far have on average larger orbital separations and higher masses than planets of solar-type stars. Furthermore, close-in planets have extreme hot atmospheres, large sizes, and high obliquities. One of the most fundamental observations is the apparent lack of close-in planets.

Two main explanations are discussed: First, it is a selection effect from the observation of evolved stars. These planets form in the protoplanetary disc and migrate inwards, for example by planet-planet scattering or disc migration. In this case, Hasegawa & Pudritz (2013) predict that the frequency of main-sequence stars with close-in planets increases linearly with stellar mass and can be about 5-11 % for IMSs. This is one order of magnitude higher than for solar-mass stars. When these stars evolve, their close-in planets are engulved. The second explanation is that the migration processes are less effective for IMSs. For example, the lifetime of the protoplanetary discs of IMSs is on average smaller than those of solar-mass stars. Thus, the disc migration time-scale might be too short to form a large sample of close-in planets. From this scenario, Currie (2009) predicts a frequency of main-sequence IMSs with close-in planets of less than 1.5 %.

Thus, the main goal of this work is to answer the question: "What is the frequency of close-in planets of main-sequence IMSs?" Although close-in planets of main sequence IMSs have been found, this frequency is not known up to now.

Most of the detections of close-in planets of IMSs are achieved by transit surveys. This is due to the fact that (i) they are unaffected by the rotation of the star, and (ii) RV-surveys typically do not cover IMSs because of their rapid rotation. For transit surveys, the geometric probability to see a transit of a planet to a $1.7 - R_\odot$ star in a 6-d orbit (a = 0.08 AU) is about 10 %. This means, if the frequency would be less than 1.5 %, one would expect to find statistically only one transiting close-in planet among a sample of 1000 main-sequence IMSs. This would correspond to the observed frequency of close-in planets of solar-type stars. If the lack of close-in planets is only a selection effect, one would expect more than 10 planets in the same sample. To calculate the frequency of close-in planets of IMSs, a dedicated transit survey is essential.

Nevertheless, driven by the aim to find planets of solar-type stars, transit surveys typically do not cover a large number of IMSs. For example, Kepler-13A b was not an interesting candidate at first glance, since its host star is an IMS. Furthermore, a ground-based survey, like SuperWASP has a typical accuracy of about $\lesssim 1\%$ for stars brighter than 11.5 mag (Christian et al. 2005). Both close-in planets of IMSs, found with ground based transit surveys, show transit depths of about 1%. As shown in Figure 1.2, a limit of 1% will only allow one to find the largest transiting planets of IMSs. The detection of CoRoT-7b (Léger et al. 2009) with a transit depth of 0.03% showed that space-based transit surveys are much more efficient to detecting shallow transits. According to Moutou et al. (2013), the noise limit of CoRoT, after several years in space, was still about 0.1 % for a 15-mag star. By phase-folding the light curve to the transit period and assuming a transit duration of 3 h, a period less than 6 d, and a continuous monitoring of about 150 d, the noise limit of the transit would be 0.06 %. A Jupiter-sized planet orbiting an $A5$ main-sequence star with $R = 1.69\,R_{Jup}$ (Gray 2005)

shows a transit depth of about 0.3%. This means that transits of planets around IMSs can be detected with 5σ even for the faintest stars in the CoRoT sample. The CoRoT survey is, therefore, perfectly suited to detect all transiting, close-in planets of IMSs with $R_P \gtrsim 1\,R_{Jup}$. To carry out a dedicated survey, I specially focus on the IMSs in the survey. The strategy is: First, characterise the stellar sample observed by the CoRoT satellite and derive the absolute number of IMSs. Second, find and characterise all close-in transiting planets in the CoRoT survey. Third, normalise the number of detected planets with the distribution of stars observed in the survey and calculate the absolute frequency of planets for stars with different masses.

This work is, thus, structured in the following way: As a first step, I do a spectral classification of a representative amount of stars to calculate the distribution of stellar masses in the CoRoT survey (see chapter 3). In chapter 4, the CoRoT light curves are studied to find transit candidates of IMSs. These transits are further characterised to obtain the parameters of the candidates and filtered to lower the rate of false positives among the candidates. In chapter 5, I introduce the instruments and methods used to perform RV-follow-up observations. To keep all the information provided within $4\,\mathrm{yr}$ of RV follow-up, I show the results of the RV-measurements in chapter 6. Further results as well as the discussions are subject of chapter (7). Finally, in chapter 8 I give a summary of all results of the survey and compare these to expectations.

To carry out this survey efficiently (spectral characterisation, light curve analysis, and the RV follow-up) Eike W. Guenther and I started a collaboration with the Dr. Remeis Observatory Bamberg of the University Erlangen-Nueremberg and the CoRoT team. Tasks that were done by collaboration partners are explicitly indicated.

3 The stellar population observed by CoRoT

The CoRoT planet finding programme was originally optimised to observe stars with spectral types F, G, and K. Furthermore, the intention of the programme was to detect the first rocky planet (Boisnard & Auvergne 2006). A goal that could only be achieved by concentrating on late-type stars that exhibit deeper transits for Earth-sized planets than IMSs. Nevertheless, avoiding red giants, CoRoT observed all stars in the fields. In order to derive the frequency of planets for stars with different masses, the true distribution of stars observed with CoRoT has to be known. Several surveys have already been conducted to classify the observed stellar population. This chapter is an overview on, first, the photometric and spectroscopic surveys already done in the CoRoT fields and, second, the results of the classifications done in this work.

3.1 Photometric spectral types

All target stars in the long runs and a part of the targets in the short runs that were observed with the CoRoT satellite were also photometrically observed in the framework of the mission preparation. The results were placed in the database EXODAT (see Deleuil et al. 2009). The database lists observed magnitudes in different bands (B, V, and R for the brightest stars), coordinates, links to other surveys, like the near-infrared survey 2MASS (Skrutskie et al. 2006), which provides magnitudes in the bands J, H, and K, and the calculated photometric spectral types. It allows the community to have easy access to the data. The photometric spectral types were calculated using a fit of the spectral energy distribution of template stars to the photometric colours, including the extinction. The extinction (also called reddening) describes the effect of scattering of light with short wavelengths due to the presence of interstellar dust. Thus, the photometric classification is confined to the measurement of continuum features, like the slope of the Paschen continuum of IMSs. This method also allows one to distinguish between giants and dwarfs for bright stars. This classification has some limiting factors. The main uncertainty in the classification is the interstellar reddening. Since in these fields the reddening is very inhomogeneous and the stars have different distances, this parameter was kept free in the fit. Another limiting factor is the fact that the observations in different bands were not done simultaneously. For pulsating IMSs that show a time-dependent flux, this method produces less precise spectral classifications.

Nevertheless, the photometric classification is the only method that allows one to classify all stars in the CoRoT fields in a homogeneous way. Therefore, it is the most important source to search for IMSs in the CoRoT fields. For the anticentre fields, Deleuil et al. (2009) found that 80 % of the stars are dwarf stars. FGK main-sequence stars are 50 % of the population and A-type main-sequence stars are the most common types in the fields. As first selection criterion, I used the spectral photometric types to identify IMSs by selecting all stars with spectral types between $B4$ V and $F5$ V.

3.2 Spectroscopy with FLAMES/GIRAFFE

Gazzano et al. (2010) carried out a survey to obtain stellar parameters in three CoRoT fields. They observed the first long-run (LR) in the anticentre (a) direction. This field is denoted

as LRa01. Furthermore, they observed a long-run and a short-run (SR) field in the centre (c) direction (LRc01 and SRc01). In order to analyse a large sample of stars they used the multi-object spectrograph FLAMES/GIRAFFE mounted at the VLT (Pasquini et al. 2002). Prior the observations a pre-selection of stars in sub-fields around planet candidates was done and, furthermore, they used photometric classifications from EXODAT to select stars that were classified as solar-like dwarf or sub-giant stars. They found a general agreement to the photometric classifications, but also some mis-classifications in the luminosity and pointed out that the distinction between giants and dwarfs is a general limit of photometric classifications. Since this survey did not include IMSs, the overlap with this sample of photometrically determined IMSs is rather small. Just one star (CoRoT number: 102677302) classified by them is in this sample. To determine statistically how well this photometric classification works for IMSs, an unbiased sample of stars has to be classified spectroscopically.

3.3   Multi-object spectroscopy

To verify the stellar population analysed by CoRoT, a magnitude limited sample of stars has to be observed. In the three anticentre fields IRa01, LRa01, and LRa02, all stars brighter than 14.5 mag were observed spectroscopically by Eike Guenther. IRa01 stands for Initial run, the first field observed by CoRoT. These observations were only possible using the multi-object spectrograph AAOmega (Saunders et al. 2004; Smith et al. 2004) at the Anglo-Australian Telescope (AAT) in Siding Springs, Australia. Almost 20 000 spectra were obtained in two observation runs in 2008 and 2009. With the 2df-facility attached to this telescope, it is possible to observe typically 350 stars in a 2-degree field of view. This is almost the size of the CoRoT fields. I did the classification of the spectra. Due to overlapping of the 2df-fields, some stars were observed several times. 11 466 stars in these anticentre fields were finally classified successfully. The results and analysis are presented in the following paragraph and were published in Sebastian et al. (2012) and Guenther et al. (2012b).

3.3.1   Computer-based spectral typing

To classify all the photometrically identified IMSs in a homogeneous way I developed a semi-automatic computer-based procedure. The basic idea is to compare each observed AAOmega spectrum to a set of well-known template spectra from a library. Each AAOmega spectrum is fitted to each template spectrum separately. This is done by minimising the velocity drift, the continuum value, and the slope. After the reduction, the spectra often show bad pixels. By analysing the derivative of each spectrum, the procedure removes automatically these bad pixels. For comparison, I selected regions of the spectrum (chunks) that contain sensible lines for the spectral classification. In the next step, the chi-square was calculated and compared for each template spectrum. The five best-matching templates, together with the AAOmega spectrum were saved and visually evaluated. This step was done to rule out false classifications due to a low signal-to-noise ratio (S/N), stellar activity, or unusual distortions of the spectra. The spectral type of the best evaluated and matching template was finally adopted to the observed spectrum.

For this survey, the goal was to classify all stars in the fields, regardless of their photometric spectral type. I adapted the programme, and did the classification for all stars observed with

status	luminosity class	O [%]	B [%]	A [%]	F [%]	G [%]	K [%]	M [%]
stars observed	IV+V	< 0.01	3.9 ± 0.2	15.9 ± 0.5	34.8 ± 0.7	15.1 ± 0.5	5.0 ± 0.3	< 0.01
with CoRoT	I,II,III	< 0.01	1.5 ± 0.1	3.0 ± 0.2	4.8 ± 0.3	9.6 ± 0.4	6.0 ± 0.3	0.3 ± 0.06
stars not observed	IV+V	0.02 ± 0.02	4.7 ± 0.3	18.9 ± 0.7	27.7 ± 0.8	13.9 ± 0.6	4.6 ± 0.3	< 0.02
with CoRoT	I,II,III	0.02 ± 0.02	1.5 ± 0.2	2.8 ± 0.3	4.8 ± 0.3	11.1 ± 0.5	9.1 ± 0.5	0.8 ± 0.1
all	IV+V	0.01 ± 0.01	4.2 ± 0.2	17.0 ± 0.4	32.1 ± 0.5	14.6 ± 0.4	4.9 ± 0.2	< 0.01
stars	I,II,III	0.01 ± 0.01	1.5 ± 0.1	3.0 ± 0.2	4.7 ± 0.2	10.2 ± 0.3	7.2 ± 0.3	0.6 ± 0.1

Table 3.1: Frequency of stars in IRa01, LRa01, LRa02.

AAOmega. The error of this classification method depends on the spectral type and the spectral library used. I tested several libraries and decided to use the CFLIB (Valdes et al. 2004), because all relevant spectral types, luminosity classes, and metallicities are covered. Furthermore, I analysed the accuracy of the method. This was possible since 33% of all stars were observed twice or several times. I used this overlap to classify all spectra of the same star independently. The differences between the results were determined for all stars repeatedly observed. The FWHM of the Gaussian fit to the resulting distribution is the precision of the method. I found that the precision of this classification of those low-resolution spectra is on average two subclasses. It is slightly better for early-type (B and A) stars (1.3 subclasses) and less precise for solar-type stars (2 - 3 subclasses). Different rotational velocities from templates with respect to the spectra might bias the classification for higher resolution. Since the resolution is too low to resolve the line profile even for the broad lines of rapidly rotating stars, the classification is not affected by this effect. The resolution is sufficient to distinguish between luminosity classes III and V, but not IV and V.

3.3.2 Spectral types in the CoRoT anticentre fields

The most important sample amongst these 11 466 classified stars are the 7 131 stars that were finally observed with the CoRoT satellite. These observations entail very precise photometric CoRoT light curves, which are analysed afterwards to find out how many IMSs can be expected in the anticentre fields. Table 3.1 lists the result of the classification. Amongst the stars that were observed with CoRoT, 50% are F- and G-type main-sequence stars. That is half the sample of the analysed fields. This is in good agreement with the findings from the photometric classification. I also found that 32.8 % of all main-sequence stars in the fields are IMSs. Eike Guenther searched for differences in the sample of stars observed with CoRoT to the sample not observed with CoRoT. He found that the stellar population is more or less the same, but the sample observed with CoRoT contains slightly more F and G dwarfs. This is due to the pre-selection which favoured FGK stars.

The detailed comparison to photometrically determined spectral types (from EXODAT) shows that for about 25% of the stars the accuracy is less or equal to one subclass. For more than 62% the accuracy is less or equal to 5 subclasses. A small fraction of 11% was classified with a difference of more than one spectral class. It is likely that these are misclassified, because of their unknown reddening, or because of intrinsic physical properties, like binarity or pulsations.

Figure 3.1 shows the comparison of the spectral types determined photometrically to those

determined spectroscopically. Negative values represent stars with a photometric type later ("lower temperature") than the spectroscopic one. For example, a photometrically determined *A*-type star is a spectroscopic *B*-type star. Positive values represent stars with a photometric type earlier ("higher temperature") than the spectroscopic one.

The comparison shows a systematic trend for *B* stars: The maximum of the distribution is at a difference of about -7 subclasses. This means, more than 98% of all *B* stars are photometrically classified as later-type stars, like *A* stars. Although the reddening of the CoRoT field was fitted as a free parameter, it is most probably underestimated for these stars. However, the distribution for *A*- and later- type stars does not show any tendency.

For the survey of IMSs, the important finding is that for more than 72% of all photometrically classified *A* and *B* stars, the spectroscopic type is earlier than *F*3. This means that essentially any star classified in EX-ODAT as an early-type star is really such a star. This result allows me to select the targets for this survey in a much easier way than it would be necessary to obtain spectra of all CoRoT targets. In conclusion, I found a relative high number of IMSs in combination with the high fraction of main-sequence stars among them as well as the fact that photometrically classified stars have in general the right spectral type. This supports the previous assumption that (1.), the CoRoT survey is perfectly suited to analyse IMSs and (2.), the photometric classifications from the EXODAT database can be used as input catalogue for the planned survey.

However, I assume that the stellar population is the same in both directions. Strictly speaking, this is only valid for the anticentre field. For example, Huang et al. (2015) mapped our galaxy by the spectroscopic analy-

Figure 3.1: Comparison of spectroscopically classified stars to their photometrically determined spectral types.

sis of about 70 000 red clump giants. This large sample was made possible by using LAMOST (Cui et al. 2012), the most efficient multiobject spectrograph that has been built up to now. One result of this survey was the homogeneous determination of a negative metallicity gradient of the stars in the anticentre direction. Santos et al. (2004) showed that giant planet formation depends strongly on the metallicity of the host star. Such an effect could lead to a higher rate of detected planets in the centre direction. Nevertheless, according to Deleuil et al. (2009), the number of targets in the centre fields that are observable by CoRoT is decreased by about 30 % due to the larger crowding and a resulting higher false positive probability. A dedicated spectroscopic survey could determine whether this effect results in a significant different stellar population observed in the centre and anticentre fields. LAMOST
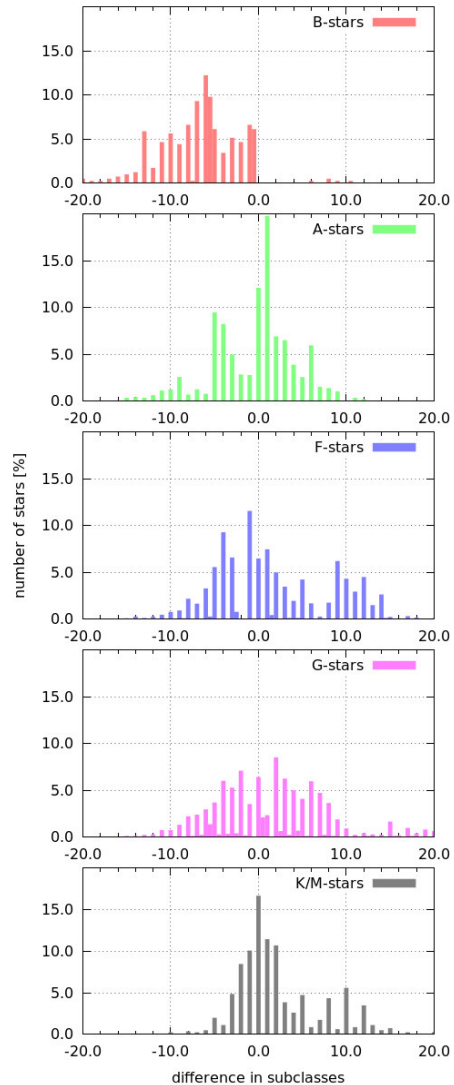
cannot observe the centre- direction due to seasonal weather conditions (Zhao et al. 2012). An ideal proposal would be to use the instrument FLAMES/GIRAFFE in a similar configuration (HR09B), as Gazzano et al. (2010). By analysing all spectral types including IMSs, an additional low-resolution setup (LR03) should be used, which allows one to analyse the blue spectral range around the H_β line, to derive the stellar parameters more accurately. Since this multi-object spectrograph allows one to obtain spectra of 130 separate objects simultaneously (including sky-fibres) in the field of view (Pasquini et al. 2002), one pointing per CoRoT field would be enough to characterise the stellar population in the 10 centre fields within 15 h of observation time. Nevertheless, Gazzano et al. (2010) found in their sample towards the centre direction a slight change in the metallicities of giant stars compared to those in the anticentre direction, but no change in the population of main-sequence stars. This finding supports the assumption that the stellar population is almost the same in both directions. Therefore, it is a valid assumption that the stellar population derived from AAOmega spectra is representative for the stellar population in the CoRoT fields.

4 Identification of transit-candidates

To find all close-in transiting planets of IMSs in the CoRoT survey, all CoRoT light curves of identified IMSs have to be analysed for candidates. Promising candidates are all stars that show several transits, with parameters that are similar to those of transiting planets (section 1.3) and can be ruled out to be false alarms (section 1.3.3). For every identified IMS, at least one CoRoT light curve is available via the CoRoT archive[2]. Some CoRoT fields are observed twice or have an overlap (e.g. LRa01 & LRa06). Therefore, for some stars also two or more light curves are available. One reason for observing many stars in the field LRc01 again was the discovery of CoRoT 7b, the first transiting exoplanet with rocky composition. During the observations in 2008, the star was active, making the discovery of the transit difficult (Léger et al. 2009). Also, the mass of the planet was a matter of debate for several years (Hatzes et al. 2011). Due to the re-observation in 2012, the parameters of the system have been re-analysed and calculated with higher precision. Barros et al. (2014) found, for example, that the activity level of the star was less than in 2008 and concluded that the transit shape in 2008 was strongly affected by spots on the star.

To find all transit candidates in this sample of light curves, I had two possibilities. First, downloading all light curves of photometrically classified IMSs and re-analyse them using well developed filtering and transit-search codes. Second, using the candidates of IMSs found already by the CoRoT team. This is more effective, since the transits were (i) already detected by several detection teams using different algorithms and (ii) not biased towards slow rotators. Nevertheless, IMSs are typically discarded, due to the photometric spectral type or if the star turns out to be a fast rotator from spectroscopy. If all light curves were analysed without any bias by the CoRoT team, the latter approach is fully appropriate. The re-analysis has the advantage to find out, whether the detections by the CoRoT team are really unbiased, for example, to pulsating stars. To be sure not to introduce any selection effect in this survey, I re-analysed the light curves for the long-run fields, observed by AAOmega as well as seven centre fields. This approach as well as the results are described in this chapter.

4.1 Light curve analysis

The reduced light curves are available online as Flexible Image Transport System(FITS)-tables. For all stars that are bright enough (roughly $< 14.5\,\mathrm{mag}$), the light curve is available in three colours as well as in combined (white) light. To increase the S/N, fainter stars are only processed as white light curves. The main goal of the planet detection algorithms is to (1.) find a transit-like signal, (2.) characterise its properties as a planet candidate, and (3.) calculate its ephemerides to predict the next observable transit, to be followed-up from ground. To do this, the time and date format of the light curves is essential. Since the on-board time of the satellite for technical reasons has an offset of about 1545 days, a correction factor is applied to get the correct Julian date. I shortly discuss the properties of the CoRoT light curves using the information in the review published by Moutou et al. (2013). The long-run light curves have an average duration of 78 days and in maximum 152 days. In the normal mode, CoRoT obtained one data point every 32 s. For a sample of 500 targets, this sample rate was directly stored. For the "normal" light curve, 15 data points

---

[2]The CoRoT archive is available online: http://idoc-corot.ias.u-psud.fr/

were combined from the on-board software to an 8 min interval (Boisnard & Auvergne 2006). Typically, the processed light curves (denoted as N2-data) were reduced and calibrated to be used for scientific research. Nevertheless, they still have to be filtered, to remove several kinds of distortions affecting the light curves. The most characteristic effect originates from the fact that the satellite is in a low-Earth orbit. This results in intensity combs in the time series due to periodic electromagnetic interferences from passing through the Earth's radiation belts like the South Atlantic Anomaly. Other effects are pointing jitter (Aigrain et al. 2009) from slight pointing variations due to varying thermal conditions between the night and day side of the orbit, or jumps due to hot pixels. These jumps origin from atomic displacements in the CCD due to hits of charged particles. The explanation is that highly energetic particles collide with the silicon structure and are energetic enough to create atomic defects. This leads to new energy levels and therefore to a different dark current. This dark current is not stable, but changes slowly due to movement of the silicon defects to more stable configurations. It means that the intensity of some pixels can increase suddenly (jump) and will decrease slowly, but there are also cases where the intensity changes very fast several times due to rearrangements of silicon defects (Pinheiro da Silva et al. 2008). Many effects are already detected in the reduction process, and the affected data points are flagged as outliers. The noise of the detectors increased due to ageing of the detectors. The noise exceeded the photon noise by a factor of two in the beginning. After four years of operation, the noise exceeds the photon noise by a factor of three (Moutou et al. 2013). Also, the number of pixels with different dark current increased with time, leading to an increased number of jumps in the light curves.

Several detection groups within the CoRoT team analysed the light curves independently. This approach has the advantage that different filters as well as transit-search algorithms produced independent lists of candidates. The transit candidates were ranked by each detection group and compared. Good candidates that were found by several groups got a higher ranking. Therefore, good candidates were selected for further follow-up. Candidates that were false positives or candidates that were too faint for follow-up with high-resolution spectrographs were discarded. This procedure leads to a very effective collaboration, where every step from light curve analysis to follow-up has separated by the best expertise. Six teams did light curve analysis in the CoRoT team, two of them in Germany. One works at DLR in Berlin (Cabrera et al. 2012) and one at Rheinisches Institut für Umweltforschung (RIU) in Cologne (Grziwa et al. 2012).

4.1.1 EXOTRANS - Transit search

Grziwa et al. (2012) developed EXOTRANS, a light curve filtering and transit detection program. The software applies first a trend filter to remove disturbances that are common in the light curves in a sample of ∼200 surrounding stars. Some jumps are removed in this way. Afterwards, a harmonic filter is applied to remove known frequencies like the orbit period of the spacecraft. Also other strong sinusoidal variations like pulsations or rotational modulations from star-spots are filtered out, but not transit-like periodic events. Transits are finally detected by searching for a box-like event in the filtered light curve. We worked together to re-analyse all light curves of intermediate-mass stars visually. Therefore, all

filtered light curves were phase-folded by Sascha to the periods found by EXOTRANS, as well as to multiples of these periods. Figure 4.1 (a) shows the filtered and phase folded light curve of LRc02_E2_0307. Note that this light curve is produced by the transit search programme, not the programme that is used to analyse the transit. Because of the filtering, the transit search programme changes the shape of the transit. Transits are confirmed, if they are also visible in the light curve that is phase folded by twice or four times the period. The light curves were visually inspected by Sascha Grziwa, Eike Guenther, Raoul Gerber and me. The candidates were distributed in pulsations, obviously binaries, transits and small, planet-like transits. We compared and discussed our resulting list to minimise false detections and compiled a list of candidates that I analysed further.

4.1.2 Multicolour analysis - Removal of false positives

At this point, we just selected IMSs, but did not apply any strong selection criterion to evaluate the filtered transits. One very important hint is given by the transit depth. Since a Jupiter-size planet orbiting a 1.7-$R_\odot$ star would cause a transit depth of $0.2\,\%$, the smallest transits are of high interest. Nevertheless, Kepler-13A b shows a transit depth of about $1\,\%$, for example. This indicates that even larger transits of IMSs can be extremely interesting, since they might be produced by very large planets. Due to the filtering process, the transit
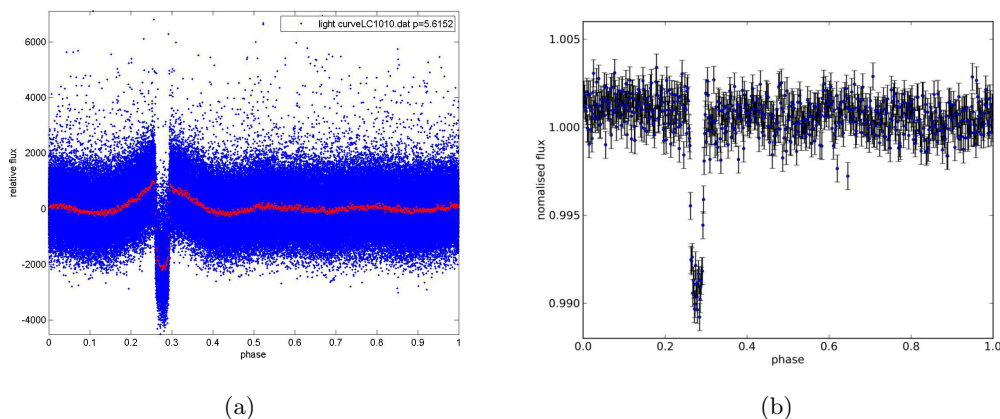

(a)   (b)

Figure 4.1: Light curve of the candidate LRc02_E2_0307 phase folded to the transit period of 5.6152 days. (a) Light curve filtered by the detection algorithm EXOTRANS. The transit was obviously detected and the period was determined. The filter affects the shape of the light curve; image by Sascha Grziwa (private communication), (b) Unfiltered light curve after detrending and binning. The shape and the transit depth of $\sim 1\%$ can easily be measured.

depth in the filtered light curve is not corresponding to the real transit depth. Using the now known orbital periods, I analysed the unfiltered CoRoT light curve for all candidates with small transits. In order to discern and analyse the light curve of the transit, the data are de-trended, the jumps are removed, and the data are finally phase-folded and binned. To do this, I developed a small python plotting tool. It phase-folds the light curve according to the already known period, fits a line to each phase interval to remove trends and long-term pulsations, and adopts finally a free adjustable binning to the data. Figure 4.1 (b) shows the unfiltered, but phase folded light curve of the candidate LRc02_E2_0307. The error bars are the statistical errors, calculated from the binned data. Thus, the three-colour light curves

can be analysed separately using the same binning, and differences in the transit depth can rule out false positives. The measurement is done quickly by hand using a cursor tool.

Finally, after combining the results of all colleagues from the visual inspection of the filtered light curves, I found 125 stars that showed transits. Afterwards, I inspected the unfiltered light curves of the candidates using the python tool described before. Candidates for planet transits were selected on the basis of the exclusion principle. I found 52 binaries that show transit depths between 0.6 and 44%, ellipsoidal variations, or v-shaped transits that are hints for gracing occupations by binary stars. Some candidates were false alarms due to pulsations that mimic transits in the filtered light curve. Since the transition between contact binaries and pulsating stars is fluent, it is not easy to distinguish between both kind of objects. Finally, I found 25 candidates with small transits between 0.2 and 3%.

4.2 Database search

After analysing the light curves from early-type stars of the AAOmega sample, I added also candidates from the internal database of the CoRoT team. The database is used to provide the team members with all important information of the candidates and the status of the follow up. Since the main scientific goal of the CoRoT team is to find planets orbiting solar-like main-sequence stars, candidates are discarded if the follow-up shows a high $v \sin i_\star$, indicating a rapid rotating host star. These candidates turn out to be quite often IMSs. Therefore, I included them in the candidate list.

4.3 Spectral typing of candidates

We have seen that the photometric classification is mandatory to derive the stellar population for many stars. It is however possible that the spectral types of some individual stars in EXODAT are incorrect. Especially the photometric determination between giants and dwarfs is not reliable for faint stars. As shown in section 1.3.3, a dwarf star that orbit a giant star can mimic a planet-like transit. It is therefore necessary to obtain spectra for all transit candidates to confirm their spectral type and luminosity class, but luckily not for all stars in the CoRoT sample. For stars not spectroscopically observed with AAOmega, the candidates were observed with longslit spectrographs. For the most interesting candidates, I combined the high-resolution spectra from the RV-measurements. They were analysed afterwards by the CoRoT team or by Christian Heuser who used grids of synthetic spectra. In these cases, accurate stellar parameters as well as metallicities were determined.

4.3.1 Data from Tautenburg

Furthermore, I initiated a campaign to re-observe candidates with the Nasmyth spectrograph mounted at the 2.0-m telescope at the Tautenburg Observatory. Between 2012 and 2014 we observed 66 candidate stars between 11 and 16 mag. I adapted my code for stellar classification, which I used to classify the AAOmega spectra, and analysed them by comparison with a catalogue of template spectra. These templates were obtained with the same instrument. The first results of this campaign were already published in Ammler-von Eiff et al. (2015).

Observations with the TLS Nasmyth spectrograph

The spectrograph used for these observations is mounted at the Nasmyth focus of the 2.0-m Alfred Jensch Telescope at the Thüringer Landessternwarte Tautenburg (TLS). It is a low-resolution spectrograph, specially designed to observe faint objects down to $V = 16 \, mag$ or even fainter objects, if they have strong emission lines. The slit that was used had a width of 1 arcsec. In combination with the grism "V200" provides a wavelength coverage from 360 to 935 Å and a resolution of $R \sim 1000$. Matthias Ammler-von Eiff and I carried out five observation runs in February and July 2012, in February and July 2013 as well as in February 2014. This allowed us to observe candidates in both viewing directions of the CoRoT satellite.

Vmag	10	11	12	13	14	15	16
S/N	300	200	120	70	48	29	17

Table 4.1: Nasmyth spectrograph: S/N for 1200 s exposure time.

Due to offset guiding and field rotation the longest exposure time is 1200 s for science observations. The S/N that can typically be achieved with 1200 s exposures is shown in Table 4.1. Given the necessary S/N of ~ 100 for a good classification (Ammler-von Eiff et al. 2015), the complete exposure time for a $V = 14 \, mag$ star is about 1.5 h. Under good weather conditions and the lowest possible airmass of 1.5 for the latitude of the site of 51°, typically 4 exposures of 1200 s are required to reach this S/N for a $V = 14 \, mag$ star. In 2.5 years our program was granted 500 hours of observing time. Due to weather only 20% of the time was useful. Finally, we were able to observe 66 faint CoRoT targets. These candidates were mostly photometric IMSs whose CoRoT light curves had a planet-like transit, but also CoRoT candidates with late photometric spectral types.

When the CoRoT field was too low, or the weather conditions were not good enough, we observed bright stars with well-known spectral types and stellar parameters to obtain a catalogue of template spectra. To observe also the templates for classification with the Nasmyth spectrograph has the advantage that I can use template spectra with similar instrumental profile and resolution. Therefore, we complied a spectral catalogue from the STELIB library (Valdes et al. 2004). Additionally, we added spectra of FGK stars analysed by Fuhrmann (1998, 2004, 2008, 2011), to increase the sensibility of the method in the temperature regime, where CoRoT has the most candidates. We also added well-classified spectra of K giants from Döllinger et al. (2011) to compensate the lack of those in STELIB. Finally, we observed 321 bright stars with high S/N and complied a library that contains a wide coverage of spectral types as well as metallicities.

Calibration and Data-reduction

The CCD of the spectrograph is cooled with liquid nitrogen, thus the dark current is negligible. Bias frames taken with a zero exposure time are used to determine the read-out noise. They were obtained regularly to monitor the stability of the detector. I measured a maximum flux change of the bias level of 0.03 % for consecutive frames and a maximum change of 0.6 % between evening and morning. This means, the detector of the spectrograph is very stable. Flat exposures are the second "standard" calibration. Such a flat-field contains information

about the spatial efficiency of the detector originating from a slightly different sensitivity of each pixel (pixel-to-pixel variations) and from the throughput of the spectrograph itself.

An ideal flat-field is taken with a source that uniformly illuminates the slit and that has a spectrum that is flat. A flat is obtained by observing a white screen, illuminated by a tungsten lamp in the closed dome, while using the same grism and slit width as for the science observations. Thus, the intensity of the flat-field depends strongly on the illumination in the dome and the position of the telescope. To reproduce the same illumination, the telescope was always pointed to the same position, and the same stabilised lamp was used. Since the lamp had to be positioned by hand, slight changes in the spatial intensity of the flat exposures were observed every night. Thus, these can not be used to correct for the throughput of the spectrograph.

The data reduction is based on Image Reduction and Analysis Facility (IRAF) scripts (Tody 1986). I combined specially adapted scripts using IRAF commands to a well-documented reduction pipeline. My pipeline is publicly available and is now used by other observers as well. It can widely be used completely automatic, but also an interactive reduction is possible. This allows the user to monitor the calibration or to change parameters for certain data. The script does the standard reduction, like bias subtraction, correction of pixel-to-pixel variations by flat-field division, trimming of the data, and automatic removal of cosmic rays. Cosmic rays are single spots or tracks with high exposures on the CCD. These mostly origin from hard radiation, like muons with an energy spectrum of $300\,\mathrm{eV}$ to $100\,\mathrm{keV}$ (Florentin-Nielsen et al. 1995). The cause of this radiation is mostly cosmic radiation, but also weakly radioactive material from the CCD dewar causes cosmic ray-like features.

Cosmic rays can be removed by averaging several frames using a median filter or by doing a sigma-clipping procedure that searches for outliers and removes them. As a first step, I subtract a mean bias to remove the cosmic rays. This can be done due to the high temporal stability of the bias level. The flat-field is not used for flux calibration, but to correct for pixel-to-pixel variations. I did the wavelength calibration, using He and Kr spectra that were observed once per run in the afternoon, when the dome was closed. After identifying prominent lines, I derive a wavelength solution for the spectra. This wavelength solution is first applied to the 2D frame. This has the advantage that the sky-background can now easily be fitted and removed from the frame. Since the wavelength solution was done only once per run, the solution can show an offset from night to night of up to $2\,\text{Å}$. This offset origins from temperature drifts and deflections in the optics. It is possible to compensate for this offset, by using the lines of the sky-background for a real-time wavelength reference. The final 1D spectra are first extracted by tracing the maximum flux. Then the surrounding pixels are added-up. Due to the high airmass of most of the targets and the spectrograph's design, a flux calibration by observing flux standard-stars is not possible.

The main effect of the airmass on the flux distribution can be explained by the refraction of the stellar image due to the Earth's atmosphere. This causes each star to be a small spectrum on the sky that is always vertically orientated. Depending on how much of which part of this spectrum enters the spectrograph, the spectral flux distribution changes. The aperture of the spectrograph is given by the slit. Two main effects cause that the slit position on the sky changes and, thus, the spectral flux distribution changes continuously: First, the spectrographs slit can not be rotated in the Nasmyth focus. Due to the guiding of the

telescope in right ascension, the projected angle of the slit on the sky is, thus, continuously changing. Second, guiding is done using a small telescope mounted on the 2m telescope. Guide errors are thus larger for the Nasmyth mode, resulting in more motion of the projected slit on the sky. Finally, I normalise all spectra by fitting a polynomial function to the continuum and by dividing the spectrum by the fit. Thus, the classification relies completely on fitting of the stellar lines, but not on the flux distribution.

Data analysis and results

I classified all CoRoT targets obtained in this campaign. Therefore, I adapted my programme, which was already used to analyse the AAOmega spectra (see section 3.3.1). The wavelength coverage of the Nasmyth spectra is wider. This gave me the opportunity to use a different set of chunks (regions of the spectrum) that not only covers the same part, as used before (4200 to 6800 Å), but additionally also a short red part (8400 to 8880 Å). The latter contains less telluric absorptions. Telluric lines are absorption lines that originate from the Earths atmosphere (see section 5.3.3 for an overview). Furthermore, this chunk contains three strong Ca lines that are good indicators for the spectral type (Gray & Corbally 2009) and also some lines of the Paschen series of HI for IMSs. For low-S/N spectra, I set the blue edge to 4800 Å to avoid regions with higher noise in the classification. Figure 4.2 shows the chunks used
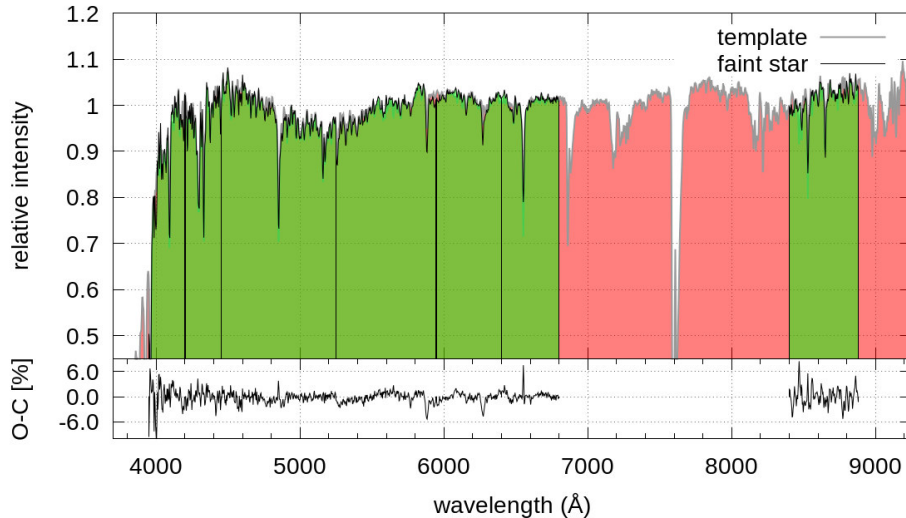
Figure 4.2: Best-fitted Nasmyth template of HD 215648 (F7 V) to the CoRoT target LR*c*07_*E*2_0482. The vertical lines symbolise the used chunks. Green areas are used for comparison, red areas are not used for comparison because of the large number of telluric lines. The lower panel shows the difference between both spectra.

for the classification with the Nasmyth templates. Each chunk was fitted separately and contributed to the calculated chi-square. The areas with strong telluric absorptions were not used. The increase of noise towards the blue edge is easily seen in Figure 4.2, although the mean S/N for this spectrum is 277. The throughput of the spectrograph is decreasing fast in this region. Since the physical parameters from all template stars are well known, I adopted not just the spectral type, but also the stellar parameters. Through this method, I obtained the stellar parameters from these low-resolution spectra rather than using a synthetic model. The spectral types of all observed stars are listed in Appendix A2.1. Since in this classifi-

cation the main source of errors is the quality of the templates, I additionally classified the spectra with the templates from CFLIB. This was done by adjusting the set of chunks to match the spectral coverage and by convolving them with a Gaussian kernel to match the resolution. This allowed me to have a second classification and to find out the quality of the classification from the S/N. I found that a minimum S/N of about 100 is required to obtain a classification with an accuracy of one to two subclasses. Low-S/N spectra often show strong discrepancies in the classifications in both the spectral type and the luminosity class. The accuracy of the classification achieved with both sets of templates is comparable for similar values of the S/N. Nevertheless, by using the templates taken with the Nasmyth spectrograph, the uncertain systematics from the convolution and the unknown instrumental profile can be avoided.

A comparison of this classification with photometric spectral types from EXODAT showed that seven candidates, photometrically classified as IMSs, turned out to be late-type stars. These were removed from this survey. This confirmed my previous result that about 28 % of the photometric IMSs are actually late-type stars. Two out of nine photometric giant stars turned out to be actually dwarf stars, making them good targets for further follow-up observations.The results of this campaign are available on a webpage to help the CoRoT community to decide which candidates are false positives, and which require more observations for the confirmation of a planetary companion.

4.3.2 Data from collaboration partners

Our collaborators from the Remeis Observatory in Bamberg observed IMSs with different low-resolution spectrographs and kindly provided the spectra for my analysis. I derived the spectral types using the same method and the semi-automatic programme described in section 3.3.1. In May 2012, Christian Heuser observed five nights with the TWIN spectrograph of the 3.5-m telescope on Calar Alto observatory[3] and took spectra of five stars in the low-resolution mode. They were reduced and kindly provided by Eva Ziegerer.

In December 2012, Thomas Kupfer and Christian Heuser observed with ISIS at the 4.2-m William Herschel Telescope (WHT), in December 2012 and June 2013, Christian Heuser observed additionally with IDS at the 2.5-m Isaac Newton Telescope. They observed and reduced 11 stars. A summary of these observations and the spectral types is given in Table A3.1 in the Appendix. Some candidates appeared to be late-type stars or giants and, therefore, can be removed from the candidate list of this survey.

For comparison, some stars were observed by our collaboration partners as well as in Tautenburg. The spectra have a high S/N (>100), but are obtained with different instruments, different spectral resolutions, and are compared with different template spectra. Therefore, the differences in the classification give a consistency check for the previously derived accuracy for the classification method used. Table 4.2 shows the differences for six stars. The standard deviation is 0.7 subclasses whereas the maximum deviation for solar-like stars is about 2 subclasses. This confirms again my previous result that the accuracy of the classification of low-resolution spectra is better than 2 - 3 subclasses for solar-like stars (see section 3.3.1).

---

[3]Centro Astronómico Hispano - Alemán (CAHA)

Object	Instrument	Spt	TLS Spt
SRc01_E1_0346	TWIN	$B5$ III	$B5$ IV
LRa01_E2_0203	ISIS	$F2$ IV	$F1$ V
LRc05_E2_0168	IDS	$F9$ V	$G0$
LRc07_E2_0146	IDS/ISIS	$F6$ IV	$F8$ V
LRc07_E2_0187	IDS	$F5$ V	$F7$ V
LRc07_E2_0482	IDS	$F6$ V	$F7$ V

Table 4.2: Comparison of different instruments.

4.4 Characterisation of the candidates

The next step is the characterisation of the candidates. This part is very important to exclude false alarms before an expensive photometric and spectroscopic follow-up and covers several steps from the analysis of each single transit up to high-resolution photometric imaging. The parameters found from the shape of the transit can already eliminate some non-planet scenarios. For example, for a planet orbiting a star with known mass and size, the semi-mayor axis as well as the maximum transit duration ($i = 90°$) can already be estimated and compared with the measured transit duration. This is done by using Kepler's third law and the assumption that the orbit is circular and the mass of the companion is small compared to that of the host star ($M_{companion} \ll M_\star$). This maximum duration should be almost the same or smaller than the observed duration. This discrepancy also allows one directly to calculate the inclination of the orbital plane. If the measured time is significantly longer than expected, it is probably a false alarm.

4.4.1 Estimation of the radius

The radius of the targets is directly measurable from the light curve, if the size of the star is known. To obtain a first estimate of the radius of the star, I used the spectral type from low-resolution spectroscopy and took the typical radius from literature (Gray 2005). By measuring the depth of the transits, I calculated the expected sizes of all candidates. These are typically in the regime of 1 to $2\,\mathrm{R}_{Jup}$. If a candidate is proven to be in the mass regime of sub-stellar objects, the stellar parameters are determined more precisely by using high-resolution spectroscopy. These parameters can be compared with evolutionary models (e.g. Girardi et al. 2000; Georgy et al. 2013) to obtain a more accurate stellar radius. Also, the parameters of the transit are then determined by fitting a model, including the influence of limb-darkening to the shape of the transit curve (Mandel & Agol 2002) to determine a more accurate radius of the companion.

4.4.2 Ephemerides of the targets

If the mid-times of the transits (ephemerides) are known with high accuracy it is, thus possible to predict future transits and schedule the follow-up accordingly. For example, it is possible to do on-off measurements (see section 1.3.3) to rule out false alarms. Also, it is possible to plan RV-follow-up observations efficiently. When RV-measurements are taken at the phases with estimated maximum blue-shift and maximum red-shift velocity, the velocity difference of both measurements can be used to efficiently exclude a binary scenario. In this

case the velocities would differ by several km/s.

The CoRoT light curve provides the only possibility to measure the ephemerides. By measuring the transit times for the full light curve and doing a linear fit to this times, the correct period is derived. Deeg (2015) determined empirically the formula of the period error (σ_P) derived from the light curve with N transits and the errors of the single time measurements σ_T:

$$\sigma_P^2 = \frac{12\,\sigma_T^2}{N^3 - N}. \tag{8}$$

He derived that the ephemeris error at the end of the light curve is:

$$\sigma_{T_{c,0}}^2 = \frac{(4N - 2)\,\sigma_T^2}{N^2 + N}. \tag{9}$$

The prediction of future transits can be done by using the ephemeris. But it raises an important limitation to the future prediction. The transit ephemeris has a small uncertainty that accumulates in time after the CoRoT photometry ends. Each new transit is counted by the epoch number (E). For the error prediction beyond the light curve, Deeg (2015) included the effect of the duration of the light curve. He showed that without doing this, the error is overestimated for long datasets. He concluded that, for the transit prediction, the error $\sigma_{T_{c,E}}$ depends on the epoch number counted from the first transit in the light curve. This can be derived as:

$$\sigma_{T_{c,E}}^2 = \sigma_{T_{c,0}}^2 + (E - N)^2\,\sigma_P^2\,; \; E \geq N. \tag{10}$$

For example, given a transit with a period of 4 d in a long-run field, the transit period can be obtained very accurately with an uncertainty of only $\sigma_P = 1.3\,s$ or $0.01\,\%$ of the 2.7 h transit duration. The ephemeris uncertainty is small with $\sigma_{T_{c,0}} = 25\,s$ because 37 transits were measured in the light curve of the long-run. After 6 years, the uncertainty of the predicted time is about 11 min. For the rocky planet CoRoT 7b, the uncertainty would be about 1.4 h (after 6 yr without measurements). With a transit duration of 1.2 h, this prediction might lead to a false time for the transit. If now the uncertainty of the period would not be 2 but 20 s the uncertainty of the transit time would be about 13 h. In this case, the transit prediction is not reliable anymore. For candidates in the first CoRoT fields with less accurate period determinations, the ephemeris are completely lost by now. Therefore, if the time of the transit cannot be recovered from photometry, then on-off photometric observations are not longer possible, as well as direct observations of the transit. However, another possibility to recover the ephemerides are radial velocity measurements. If the orbit solution might be adopted successfully, the ephemerides can be calculated from the RV-curve.

4.4.3 Identification of contaminants

The exoplanet field of the CoRoT satellite is specially designed to optimise the photometric search for planetary transits. Therefore, a prism disperses the light into low resolution spectra to obtain light curves in different colours. This in return results in a low spatial resolution, but also in high photometric precision. The masks are selected to avoid strong contamination by nearby stars. Nevertheless, especially in the centre fields, many masks contain faint contaminants, which affect the resulting light curves and can lead to false

positives if, for example the additional light comes from an eclipsing binary in the background. Also, if the transit is on the main target, this light influences the measurement and could lead to smaller transit depths and different depths in each colour. One solution is the comparison of the mask with high-resolution ground-based images. This has been done for almost all CoRoT targets in a photometric survey (Deleuil et al. 2009). The results are used to determine a contamination factor, available via EXODAT. Since it would not be possible to follow up the main target separately, I excluded candidates with very high contamination factors and obvious contaminants. Additionally, I used the library of the Canada France Hawaii Telescope (CFHT)[4] to identify the contaminants of interesting candidates within or nearby the CoRoT-masks. Several CoRoT targets were followed-up in the past years using the MegaPrime/MegaCam wide-field imager (Boulade et al. 2003) to check them for nearby eclipsing binaries via on-off photometry (Deeg et al. 2009).

Since the field of view is about 1 x 1 square degrees with 0.19″/pix resolution, this database provides excellent, high-resolution (seeing-limited, but typically $\lesssim 1''$) images of almost the complete CoRoT field. If a time-series of images was obtained with the CFHT, I co-added all available data to improve the S/N and got a deeper image of the target. In all cases, when I detected contaminants inside the mask, I estimated the brightness difference to the target star to calculate the contamination factor of the CoRoT light curve. For example, Figure 4.3 shows a part of a CFHT image of the candidate IRa01_E2_2721. The image was taken using the filter g.MP9401 (414 - 559 nm). The CoRoT mask covers two faint stars and a third one that is close
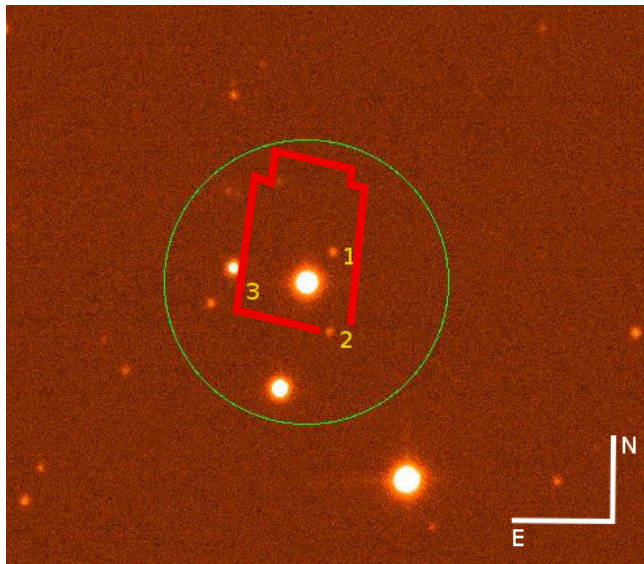
Figure 4.3: Part (1.75 x 1.75 square arcmin) of a ground-based CFHT image that includes the candidate IRa01_E2_2721. The main target is centred in the green circle (r=25 arc sec). The red overlay marks the shape of the mask of CoRoT and possible contaminants are labelled.

to the mask. As shown in Table 4.3, all of these three direct contaminants are three magnitudes or more fainter. They are too faint and too far away to be a problem for the spectroscopic follow-up. Nevertheless, the light of them could influence the measured transit depth. Furthermore, the blue part of the dispersed light from the bright star that is about 20″ south-east of the target could be visible in the red light curve.

4.5 Bringing it all together: The candidate list

Table 4.4 shows the measured parameters of all candidates that were followed-up with high-resolution spectroscopy (see chapter 5). It is divided in four main parts. The left row contains the WIN-*ID*s. These are internal CoRoT numbers that indicate the observed field

---

[4]CFHT data are provided via the Canadian Astronomy Data Centre; http://www4.cadc-ccda.hia-iha.nrc-cnrc.gc.ca/en/

star	brightness difference [mag]	distance ["]
1	5.6	5.6
2	5.9	~ 10
3	3.0	> 10

Table 4.3: Possible contaminants in the CoRoT mask of IRa01_E2_2721. The brightness difference is relative to the brightness of the target.

(as explained in section 3.2) and in which of the two detectors of the exofield the star was located (E1 or E2). The second row contains the spectral type (Spt) that was derived from low resolution spectra. The instruments used to obtain the spectra are indicated by numbers: [1] AAOmega, [2] NASMYTH(TLS), [3] ISIS, and [4] TWIN. The physical parameters, the radius ($R_\star$) and mass ($M_\star$) of the stars that follow from this classification are obtained from Gray (2005). The third set of columns list the parameters obtained from the light curve: The ephemeris, the orbital period (P), the transit depth (t_d), and the transit duration (t_τ). As explained above, these parameters can be used to cross-check the physical properties of the object that is causing the transit. The right part of Table 4.4 shows the calculated sizes, the semi-major axis (a), as well as the expected transit duration for the planet ($t_{\tau exp}$). The calculated distance to the star can be compared to the radius of the star. The two closest companions have, therefore, LRc02_E1_0132 (with $a = 1.8\,R_\star$) and IRa01_E2_2721 (with $a = 2.5\,R_\star$). For almost all candidates, the observed transit durations are of the same order as the calculated ones.

ID	Spt	$R_\star$ [$R_\odot$]	$M_\star$ [$M_\odot$]	Ephemeris [HJD]	P[d]	t_d [%]	t_τ [h]	Radius[R_{Jup}]	a [AU]	$t_{\tau exp}$ [h]
IRa01_E1_4591	A5 V[3]	1.69	2.04	2454141.4994	4.29	0.36	2.12	1.0	0.07	3.94
IRa01_E2_2721	A6 V[1]	1.69	1.97	2456298.7650	0.61	0.80	1.23	1.5	0.02	2.08
LRa01_E2_0203	F1 V[2]	1.5	1.6	2454572.9633	1.86	0.03	1.55	0.3	0.03	2.86
LRa01_E2_0963	F0 V[1]	1.62	1.66	2454398.0761	4.65	0.06	4.79	0.4	0.06	4.15
LRa01_E2_1578	F6 V[2]	1.35	1.35	2454467.7346	16.06	0.43	34.80	0.9	0.14	5.60
LRa02_E1_0725	A5 IV[1]	1.8	2.04	2454883.7168	9.09	1.40	9.09	2.1	0.11	5.38
LRa02_E1_1475	A5 V[3]	1.59	2.04	2454842.8223	2.12	0.30	2.62	0.9	0.04	2.93
LRa02_E2_1023	F3 V[3]	1.45	1.5	2454787.5496	0.78	0.12	2.85	0.5	0.02	2.12
LRa02_E2_4150	B4 V[3]	3.0	5.0	2454901.0701	8.17	0.65	3.41	2.4	0.14	6.42
LRc02_E1_0132	F6 III[4]	7.0	2.0	2454713.0140	3.69	10.35	9.19	21.9	0.06	15.61
LRc03_E2_2657	A7 V[4]	1.68	1.93	2454929.2877	5.15	0.20	6.00	0.7	0.07	4.23
LRc07_E2_0108	A9 IV[4]	1.7	1.8	2455673.1117	14.45	1.82	3.70	2.2	0.14	6.19
LRc07_E2_0307	F6 V[2]	1.35	1.35	2456712.8967	5.62	0.93	5.03	1.3	0.07	3.95
LRc07_E2_0482	F7 V[2]	1.25	1.3	2455737.8378	1.82	0.67	2.31	1.0	0.03	2.54
LRc08_E2_4203	F3 V[2]	1.45	1.5	2455753.4917	3.29	0.33	3.99	0.8	0.05	3.42
LRc10_E2_3265	F6 V[4]	1.35	1.38	2456118.9850	4.83	0.08	1.10	0.4	0.06	3.72

Table 4.4: Hot CoRoT candidates, finally followed-up in this survey

The difference can be due to eccentric orbits, companion masses that are in the stellar regime, or just due to a false stellar radius. One example is LRa01_E2_1578. It shows a shallow transit that is six times longer than expected, which leads to the conclusion that this transit cannot be caused by a planet. Since it shows a very interesting light curve with a strong interaction, I decided to keep it as a bad weather alternative for the McDonald observations (see chapter 5). Another example is LRc02_E1_0132. Its transit is much shorter than expected. This can be explained, if the orbit of the planet is not exactly aligned to the line of sight (i $\lesssim 90°$). It could also indicate that the observed luminosity and radius of the host-star are actual smaller than expected. A false classification can origin from a composite spectrum of both,

the star itself and the light of a bright stellar companion. Since the light curve shows a transit that is about 11 % deep as well as a secondary transit, its nature as binary is very obvious. Nevertheless, it is a relatively bright target, and I kept it in the list to prove the accuracy of the radial-velocity measurements while obtaining a binary orbit. The final sample contains 14 transiting CoRoT targets with periods ranging from 0.6 to 14 days. 57 % of them are located in the anticentre direction. The mean size of the objects is about 1.1 R_{Jup}. That means that these candidates have generally large radii and are probably massive. If confirmed, this tendency would be in agreement with the findings of Ida & Lin (2005) that more massive stars harbour more massive planets. The observational parameters like coordinates and brightness are given in the appendix (Table A4.1).

5 Radial velocity measurements

In the two previous sections, I showed that follow-up observations of transit candidates reveal plenty new information that can determine whether the transit is caused by a real sub-stellar companion. This verification is crucial to exclude possible false alarms (see section 1.3.3). Fressin et al. (2011) suggested a statistical approach to calculate the probability for false alarms. In their method, they derive a large number of possible configurations for blends due to false alarms and compare them with the actual shape of the transit. They then statistically determine the probability that the apparent transit shape is rather caused by a planet than a blend. If this probability is several orders of magnitude higher than that for a blend, the planetary nature is validated (Borucki et al. 2012). This method is currently used to verify planet candidates as real planets if follow-up observations do not allow a sufficient conclusion. This method is important, for example, for the Kepler mission, which allows the discovery of small rocky planets in or close to the habitable zone of solar-like stars (e.g. Jenkins et al. 2015). In such cases, with state-of-the-art instrumentation, it might not be possible to verify the planets otherwise (Fressin et al. 2011).

Nevertheless, the best way to characterise a candidate is to detect and analyse it with several methods independently. For example. after three years of high-resolution spectroscopic observations in August 1999, Mazeh et al. (2000) published periodic radial velocity variations of the star HD 209458. Motivated by these results, in September of the same year, precise photometric observations revealed an obvious transit. It was thus for the first time proven that this star has indeed a transiting planet. The combination of this two detection methods is a powerful tool to give access to a wide characterisation of the physical parameters of the system. Since the inclination of the orbit can be determined from the transit, the mass derived from RV-measurements is the true mass and the mean density of the planet can be calculated. Furthermore, a separate and independent detection gives the proof of the existence of the companion.

In the case of the CoRoT survey, all candidates are already known to show a planet-like transit. Before an object is published by the CoRoT team, an intensive characterisation is performed. This includes precise high-resolution spectroscopic measurements to calculate the mass and, thus, verify the sub-stellar companion.

5.1 Precision of RV-measurements

Radial velocity measurements are done by calculating the precise positions of stellar absorption lines in high-resolution spectra (see section 1.2). The accuracy of the RV-measurement depends strongly on the shape, the strength, and the number of analysed lines. A spectrum with very sharp lines that show little rotational broadening can be measured with much higher precision than a spectrum with some lines with wide shapes. This sharpness is limited by the resolution of the spectrograph. If the resolution is high enough to resolve single lines, it depends on different line-broadening mechanisms like rotational broadening (see chapter 1.5.2). Noise gives another uncertainty to this measurement. The measurement of a spectrum with many, but noisy lines can be as accurate as the measurement of a spectrum with high S/N and less lines. For solar-like stars or low-mass stars, it is in general very easy to calculate the radial velocity. Since these stars rotate slowly and their atmospheres exhibit

many elements to absorb the stellar light, their spectra show thousands of sharp lines.

In short, the precision of RV-measurements depends (i) on the signal to noise, (ii) the spectral type, (iii) the wavelength range, (iv) the rotational broadening, and (v) the resolution of the spectrograph. Bouchy et al. (2001) described the precision by the formula:

$$\sigma[m/s] = \frac{c}{Q * S/N},\qquad(11)$$

where S/N is the signal-to-noise ratio, c is a constant that is unique for each spectrograph, and Q is a quality factor that depends on the other factors mentioned above. This quality factor was calculated for several spectral types and $vsini_\star$. The precision decreases by a factor of two if the star is not a late $K7$ star but an early $F2$ star. For an early-type $F2$ star, the precision decreases by a factor of ten if the star rotates with $vsini_\star=20\,$km/s instead of zero rotation.

An empirical estimation for the precision that depends on these factors is given by Hatzes et al. (2010):

$$\sigma(m/s) = C\ S/N^{-1}\ R^{-3/2}\ B[\text{Å}]^{-1/2}\ [f(SpT)]^{-1/2}\ (vsini_\star[\text{km/s}]/2\,\text{km/s}).\qquad(12)$$

$f(SpT)$ is a function that takes the line density into account, and is 1 for solar-type stars and 0.1 for A stars. It allows me to calculate the precision also for hot and faster rotating stars. For C $= 2.4 * 10^{11}\sqrt{\text{Å}}\,\frac{m}{s}$, taking into account a spectral range of $2000\,\text{Å}$, a resolution of 60000 (typically for high-resolution Échelle spectrographs), a S/N of 150, and an A star with $vsini_\star = 20\,$km/s the expected accuracy is about 80 m/s. A massive planet with $M_{\text{Pl}} > 2\,M_{\text{Jup}}$ in a circular orbit with a period of four days, for example, would induce radial velocity variations with a semi-amplitude of $K = 170\,m/s$ for a 1.9-$M_\odot$ host star. Thus, the accuracy of 80 m/s would be sufficient to detect such a planet. Planets of IMSs with much larger separations induce smaller radial velocity variations and, thus, are below the detection limit of the RV-method.

5.2 Observations

Radial velocity measurements were taken from 2012 to 2014 with various instruments at different observatories. Table 5.1 lists all observations used for this work. The instruments have comparable resolution, but differ in spectral range, stability, and reachable S/N. Since most of the targets are 13 to 14 magnitudes, at least 2-m-sized telescopes are necessary to obtain high-resolution spectra with sufficient S/N. Because of this low S/N, the iodine-cell method cannot be used, since the absorption in the cell would further reduce the signal. Therefore, ThAr-calibration were chosen for all high-resolution spectra, taken in this programme.

5.2.1 Data reduction of Échelle spectrographs

High-resolution échelle spectra are significantly different to longslit-spectra. Furthermore, the required accuracy for the reduction is much higher than for low-resolution spectra. This section summarises the basis of the data reduction by using standard IRAF commands. First of all, bias frames of each night are combined. Then, the mean value in the overscan of the CCD is measured and removed. The resulting image is fitted in two dimensions with

a spline3-function of the order 3. This creates the so-called slope, a frame that shows the general structure of the bias frames, but not the intensity. Afterwards, the slope and the mean value from the overscan is subtracted from each frame to count in a possible change of the bias level.

The next step is to create a master-flat. To do this, first all flat-fields taken in one night are combined, then the slope and the bias-level are removed. One frame of a standard star with well defined orders is used to extract the orders of the combined flat. A legendre polynomial fit is performed to each order, to remove the blaze function. By dividing trough the master-flat, pixel to pixel variations, and fringes are corrected. Fringes appear in the red part of the flats as well as in the science spectra. It is an interference pattern that appears when the thickness of the layers of the detector are multiple of the wavelengths of the light.

The next step is to remove bad columns in the CCD frame. For this the IRAF task fixpix is used that removes distorted columns and interpolates the values from the neighbouring columns. Scattered light, which is visible between the orders, is removed using the IRAF task "apscatter". Cosmics are removed by the IRAF task "xzap", that uses a two dimensional sigma clipping method to remove high intensity outliers with none or very small spatial extension. Afterwards, the frame is divided by the master-flat and extracted by the IRAF task "apall". The most important part is finally the wavelength calibration. This step has to be very accurate in order to calculate precise RVs. The calibration spectra are wavelength calibrated using a catalogue of ThAr lines, the IRAF tasks "identify", and "reidentify". Using the tasks "refspectra" and "dispcor" the wavelength solutions are finally applied to the spectrum of the candidate.

5.2.2 SANDIFORD

Some of the data were collected using the Sandiford Échelle specrograph mounted on the 2.1-m telescope at McDonald observatory (McCarthy et al. 1993). Three observation runs were performed within this project. The first run was between third of January and 19-01-12. 13 candidates were observed several times to cover their orbital periods. The second run was between second of July and 08-07-2012 to observe the candidates in the centre fields. I observed and covered the periods of four candidates. The third run was from 28-12-12 to 07-01-13. Stephan Geier and Christian Heuser successfully re-observed three of the brighter targets.

The spectra have a wavelength coverage from 4000 to 4400 Å, which covers the hydrogen lines in the blue part of the spectrum. The spectrograph is mounted directly in the Cassegrain focus of the telescope and, therefore, moves together with the telescope. Using Formula (12) and the given parameters: the wavelength range, the resolution of 60 000 with $1''$ slit width, and a mean S/N of about 20 for most of the candidates the reachable RV-precision is about $140\,\mathrm{m/s}$. If the star rotates with $vsini_\star = 20\,\mathrm{km/s}$ the precision decreases to $1.4\,\mathrm{km/s}$. The instrument is, therefore, ideally suited to separate binaries from real planet candidates. For real planets, the accuracy would only be sufficient to determine upper limits.

Data reduction

In the afternoon of every day bias and flat-field calibrations were obtained. To correct for instrumental drift the flat-field exposures were done with another slit that has the same slit width but a 10 mm slit height instead of 2 mm. To follow possible RV-shifts due to bending of the spectrograph, I took ThAr calibration frames right before and after each exposure. I did the reduction by using a modified pipeline from the Tautenburg Échelle spectrograph. This pipeline was adapted to the chip size, position of the overscan, number of Échelle orders, and instrumental errors, like columns of dead pixels and scattered light.

(a) (b)
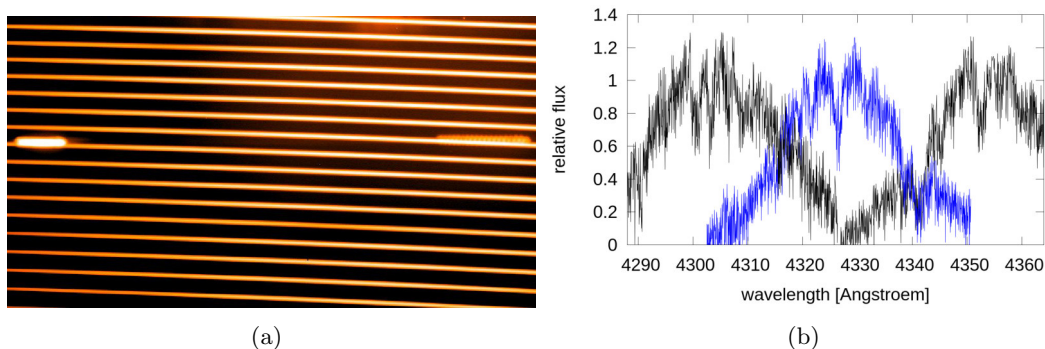
Figure 5.1: (a) Part of an Échelle frame taken with the SANDIFORD spectrograph at the 2.1-m telescope at McDonald observatory. (b) Reduced McDonald spectrum of $LRa01\_E2\_1578$.

Figure 5.1 (a) shows a well-exposed frame of the star HD 120315. Well-shown are the internal reflections that make some parts of the frame unusable. These parts are set to zero or, in case of the master-flat, to the value one. Also, visible is the scattered light between the orders. Figure 5.1 (b) shows a reduced spectrum of the star LRa01_E2_1578. Three orders of the spectrum are plotted. The overlap between the orders, as well as the blaze-function that remains in the spectrum are visible. The blaze function will be removed using a special blaze-fitting tool (see chapter 5.3.1).

5.2.3 CAFE

The Calar Alto Fiber-fed Échelle spectrograph (CAFE), Aceituno et al. (2013)) is mounted on the 2.2-m telescope at Calar Alto observatory. The instrument is fibre-fed and therefore not directly attached to the telescope. The spectrograph is situated in the dome and mechanically highly stabilised. The temperature in the spectrograph room is passively stabilised due to the thick isolation of the foundation of the dome. The overall wavelength ranges from 4000 to 9500 Å. After removing telluric features (atmospheric absorption lines, see section 5.3.3), I used a wavelength coverage of 2800 Å for radial velocity measurements. Given this coverage, a resolution of 60 000, and a typical S/N of ~ 20 for a 13.5 mag star the RV-precision is about 50 m/s for a slow rotating A-star. It decreases to 0.5 km/s for a fast rotator with $vsini_\star = 20$ km/s. By assuming a faint and fast rotating A star that shows a transit with a period of four days, this accuracy combined with the increased mechanical stability of this instrument allows one to detect massive planets down to $10\,M_{\mathrm{Jup}}$. Three observation runs using were performed. The first one was from 14 to 19-12-12. In these six nights I successfully observed five candidates. The ThAr calibration frames were obtained each, one before and

one after the target spectrum. The second run was in service mode and was carried out in the time between 22-11-13 and 11-12-13. This time, solely the candidate LRa01_E2_0963 was observed to cover its orbit completely. In this run the ThAr calibrations were taken in the afternoon and possible drifts over-night, were compensated by comparing the positions of the telluric lines. The last run for this project was from 26 to 30-12-14. Eike W. Guenther observed two target stars of this programme every night under very good weather conditions.

Data reduction

The maximum sensitivity of the instrument is in the red part of the spectrum. To obtain a flat-field exposure, that also corrects in the blue part with a sufficient high S/N, one has to take many flat-fields and combine them. In the first run 2012, I took every afternoon 60 flat-fields of 20 s and combined them. Figure 5.2 shows the red part of flat-field frame. Visible are the orders and the fringes. The broad wavelength coverage of the spectrograph means also

Figure 5.2: Part of a typical flat-field frame, taken with the CAFE spectrograph at the 2.2-m telescope at Calar Alto observatory.

that there are much more orders than in the SANDIFORD spectrograph. The Échelle frames contain 83 orders. The observatory provides a simple reduction pipeline for CAFE data that I used to reduce the data. The pipeline is based on IRAF scrips and was written by Uwe Wolter and Rainer Wichmann. The pipeline uses similar scripts as the Tautenburg pipeline and is optimally adopted to the CAFE-frames. In Summer 2013 the Dewar of the CAFE-camera had to be repaired. Due to the replacement, the CCD was slightly shifted in the focal plane. I had to adjust the pipeline for the data, obtained in November and December. This was easily achieved by re-identifying the apertures and the wavelength calibration. Thus, the wavelength-coverage has been shifted slightly towards the red part.

5.2.4 TWIN

The TWIN spectrograph[5] is a two channel Cassegrain instrument mounted at the 3.5-m telescope at Calar Alto observatory. It provides simultaneous observation in the blue and red part of the spectrum. It provides a large sample of different gratings from low to intermediate resolution for both spectrograph arms. Using the gratings T01 and T10, I got a resolution of $\sim 7\,000$ in both arms and with 30 min exposure time, a S/N of 80 for V= 14 mag targets. Considering this resolution, the RV-accuracy is about 3 km/s for an A star with $vsini_\star = 20$ km/s. This is perfectly sufficient to rule out binaries from my sample of stars.

Six nights were granted in service mode. For this spectrograph, the service mode observations have to assigned to complete nights or several nights, because the instruments has

---

[5]More information and technical data can be found on the homepage of the observatory: http://www.caha.es/CAHA/Instruments/TWIN/

to be mounted and the instrumental set-up of the telescope cannot be switched during the night. Six targets were observed successfully in this run. The data were calibrated with Helium-Argon exposures before and after the target spectrum was observed.

Data reduction

The spectrograph is a long slit spectrograph. The main difference to the NASMYTH spectrograph is that TWIN has two arms. Therefore, to reduce the spectra, I adapted and used the IRAF- pipeline, I developed for the NASMYTH-spectrograph in Tautenburg (see chapter: 4.3.1).

5.2.5 Other observational data

I analysed most of the targets, using data from the instruments mentioned above. Nevertheless, for the many interesting targets high-resolution spectra were kindly provided by collaboration partners, the CoRoT team, and online databases. I analysed all data in a homogeneous way to finally combine all datasets. UVES is a high resolution spectrograph mounted in the Nasmyth focus of the Unit telescope 2 (UT2) at the Very large Telescope (VLT) on Paranal Observatory (see Dekker et al. (2000)). The telescope has a main aperture of 8 m. By using ThAr-calibrations, the spectrograph reaches an RV-accuracy of 0.2 km/s for a V= 14.0 mag A star with $vsini_\star = 20$ km/s.

Four observing runs in service mode have been performed within this project. In summer 2013, time-resolved spectra of LRc07_E2_0307 were obtained to measure the radial velocity during the transit. From October 2013 to January 2014 the targets LRa02_E1_1475 and LRa01_E2_0203 were observed to cover their orbital periods. In Summer 2014, two candidates from the centre-fields were observed. Both were observed with TWIN before and revealed RV-variations that were consistent with companion masses in the brown dwarf regime. The last service mode run was performed in November and December 2014 to follow-up IRa01_E2_2721. This candidate was an extremely interesting candidate for a very close-in binary (see section 6.15).

In February 2012 and January 2013 the target LRa02_E1_1475 was also observed with the HIRES spectrograph at the 10-m KECK telescope (Vogt et al. 1994). The resolution of this spectrograph is about 67 000 and, thus, depending on the used slit width, in the same order as the UVES spectrograph. In addition Davide Gandolfi observed several targets with the FIES spectrograph (R=67 000 in the high and R=47 000 in the medium resolution mode, respectively), mounted at the 2.5-m Northern optical Telescope, at Roque de los Muchachos observatory (Telting et al. 2014). This telescope has only a slightly larger aperture than the used telescopes on Calar Alto and Mcdonald observatory, but It has a much better efficiency. The higher S/N obtained with this instrument combined with similar resolution increases the reachable RV-precision. The targets LRc07_E2_0307, LRa01_E2_0963, and LRa02_E2_4150 were observed and analysed. Furthermore, Christian Heuser kindly provided intermediate resolution spectra of the target LRc07_E2_0482. These spectra have a lower RV-accuracy in the order of some km/s, but are ideally suitable to distinguish between a binary or a planet solution. These were taken in May 2013 with the intermediate dispersion spectrograph (IDS). The instrument is a longslit spectrograph mounted an the 2.5-m Isaac Newton

Telescope at Roque de los Muchachos observatory. Finally I used for three objects the ESO[6] archive (Rossat et al. 2005) to search for available HARPS spectra. Some of my targets were observed by the CoRoT group, with Francois Bouchy as PI. It is a fibre-fed spectrograph, mounted on the 3.5-m ESO telescope in La Silla. HARPS is the most stable spectrograph used in this work.

ID	SANDIFORD	CAFE	TWIN	UVES	FIES	HIRES	HARPS	IDS
IRa01_E1_4591		6						
IRa01_E2_2721	4	4		25				
LRa01_E2_0203	18	8		5				
LRa01_E2_0963	3	18			7			
LRa01_E2_1578	4							
LRa02_E1_0725	5							
LRa02_E1_1475	2	4		15		5	17	
LRa02_E2_1023	4							
LRa02_E2_4150	15	7			10		2	
LRc02_E1_0132	6							
LRc03_E2_2657			7	4				
LRc07_E2_0108	7		13					
LRc07_E2_0307	3		18	12	29		6	
LRc07_E2_0482	2		8					3
LRc08_E2_4203			6	8			2	
LRc10_E2_3265			6					

Table 5.1: The 16 candidates in an overview of all RV-observations and number of useful spectra for this project.

5.3 Measuring radial velocities

The shift of one pixel of the CAFE spectrograph corresponds to a RV-shift of $2\,\mathrm{km/s}$. To measure a shift of $1\,\mathrm{m/s}$, one needs to measure a shift of about 0.005 pixels. Therefore, to find planets, one needs a method to measure shifts in the sub-pixel regime. To achieve this, the commonly used method is the comparison of the spectrum to a template spectrum with the same resolution. This can be, for example a synthetic spectrum calculated from model atmospheres with parameters that are similar to the observed star. To analyse the RV-drifts of the CORAVEL spectrograph, Baranne et al. (1979) used a box-shaped mask that is different from zero at the positions of the spectral lines. Every box is weighted to the relative depth of the spectral line. Alternatively, this template can be a spectrum of the same star or a known star with similar atmospheric parameters observed with the same instrument. Using such a "real" template has the advantage that the resolution as well as the instrumental profile are the same and therefore, are already ruled out as source of systematic errors. For this comparison different methods are applied. Typical used in the field of precise RV-measurements is the cross-correlation function (CCF) method. The CCF is a multiplication of the spectrum and a template in the Fourier-space. If the spectrum would be identical to the template, but is shifted by $d\lambda$, the CCF would have a peak of 1 at $d\lambda$ (Tonry & Davis 1979). Thus, the maximum of this function corresponds to the relative velocity drift and is usually obtained by fitting a Gaussian profile to the CCF peak.

Also, the method of least squares fitting is used to calculate the velocity drift between template and spectrum. In this case the optimal template should be a model or observed spectrum

---

[6]The archive of the European Southern Observatory (ESO) can be found online: http://archive.eso.org

rather than a box-shaped mask. Otherwise the fitting would not work. One example is the HARPS TERRA algorithm that was successfully applied to HARPS data and showed to be even more accurate than the CCF method (Anglada-Escudé & Butler 2012).

These methods allow me to derive the relative velocity in respect to the template spectrum. To calculate the real velocity we have to keep in mind that the telescope is located itself on a place on Earth. A body that rotates in 24 h, and orbits the Sun in 365 days. The orbital velocity of the Earth only is about 30 km/s. This leads to an additional velocity offset that has to be removed from the relative measurement. The correction that corrects for the movement of the earth with respect to the sun is called heliocentric correction. It can be calculated, if the position, of the observatory, the time and date of the observation is known (Eastman et al. 2010). I used the IRAF tool "rvcorrect" to calculate this offset and removed it from the relative velocity.

Both, the CCF method and the least squares fitting method show good results for determining precise RV-measurements. Nevertheless, the CCF method is most efficient for spectra with hundreds of sharp lines. Regarding the promising results of the HARPS TERRA project, and the targets in this survey, that have less spectral lines, than solar-type stars, which are rotationally broadened, I decided to use the least squares fitting method to derive the radial velocities of the IMSs observed in this work.

5.3.1 ASFIA - Automatic Spectral FItting Application

To analyse all spectra with the same method, I developed a new tool that performs a least squares fitting to a given part of the spectrum. In principle it consists of two mayor parts. The first part adopts the input spectra to the same format. The user can decide which part of the spectrum will be compared by selecting one or multiple wavelength ranges. This part also includes the removal of the blaze function, if needed. The second part calculates the least squares optimisation by Doppler shifting the spectrum, until it matches to the template best. As template, I use co-added spectra of the target star, if the S/N of the spectra allow to do this. Otherwise a model-spectrum of similar physical parameters is used. The result is a measurement of the relative velocity that is finally translated into the real radial velocity of the star.

The program is written in Python 2.7.2. The least squares fitting itself is done trough Fortran codes. This reduces the CPU time required for the calculation significantly. It is maintained and developed since 2012. Since the array-length are optimised, a normal desktop computer with at least 4 GB RAM and UNIX/Linux operating system is required. Since the spectra originate from different spectrographs, the program has to be able to read spectra in different data-formats. Échelle spectra that I reduced with IRAF, have the advantage that they are all in the same data format. So, typically it is a multi-order FITS file, with the blaze function still included. Other formats are multi-order FITS files with the blaze function already removed, or one-dimensional FITS files with all orders combined. As preparation spectra with low S/N can also be binned prior the comparison. Eventually included cosmic-ray hits can be removed using an internal sigma clipping algorithm. This algorithm divides the spectrum in chunks and calculates the local standard deviation. All pixels that exceed a freely adjustable value above the noise are excluded. All parameters of these processes are adjustable to match

each spectrum individually. If the blaze function is still included in the reduced spectra,
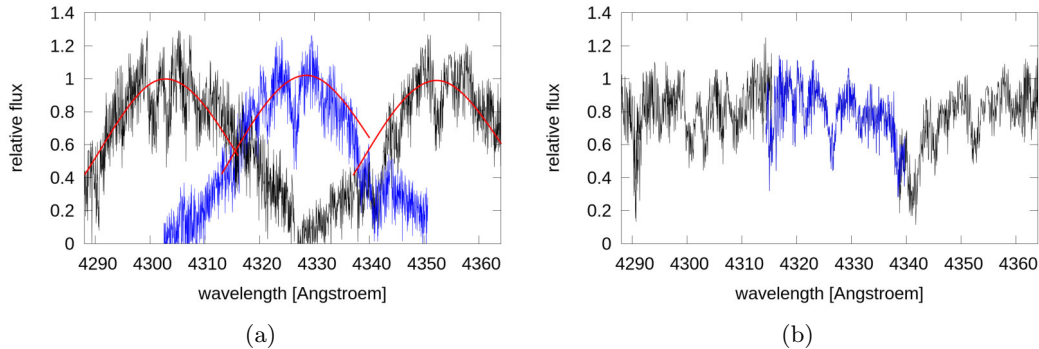
Figure 5.3: Three orders out of the reduced spectrum of the star *LRa*01_*E*2_1578 The middle order is highlighted in blue to distinguish between the orders. (a) The fitted Blaze function is shown as red line. (b) The same spectrum after the Blaze function is removed.

it has to be removed in the same way for all spectra. Different methods are commonly used to remove the blaze function from the spectra. Typically it is already removed, if the spectra are divided by the flat-field during the reduction process. Nevertheless, sometimes this procedure does not remove the Blaze function entirely and leaves residuals. To remove the Blaze function from reduced spectra one can, for example use a *sinc*-function, fit it to each order, and remove this function. Sometimes this method has the disadvantage that the Blaze function is not symmetric like a *sinc*-function. Therefore, I decided to use a well exposed stellar spectrum or a flat-field frame to extract the Blaze function. To obtain the Blaze, I first remove artefacts, the background, and the fringes from the spectrum and extract it. In the next step, I do a two-dimensional fit over all orders with a low order polynomial. The Blaze function obtained in this way includes all asymmetries that are contained in the spectra and match also changing asymmetries over the different orders. One has to keep in mind that it includes also the energy distribution of the observed star or flat-field lamp. This effect introduces a slope and a different amplification of the different orders than the Blaze function in the target spectra. This can easily be adjusted by fitting the blaze to the spectra, order by order. I first do a sigma clipping of the orders to exclude deep and small lines. Then, I combine the order with the two neighbouring orders by keeping the maximum flux. Using this, I exclude deep forests of lines and broad features like the Hydrogen lines from the fitting. To do the fit, I add a slope, a linear broadening, a intensity adjustment, and a simple Doppler shift to the function and search for the best least squares fit. This fit is done for each order. This method works well for spectra with a value of S/N high enough so that the blaze function is well defined. Intensive tests have shown that this algorithm is very robust. The method is primarily developed for spectra of IMSs. The result of this process are the Blaze functions for each order, stored as ASCII files, that optimally matches the spectrum. The values for the sigma clipping can be adjusted easily to remove deep forests of lines in late type stars. Nevertheless, for solar-type stars, the line density is so high that is is very difficult to recover the real continuum. In this case the automatic Blaze removal can be switched off and the correction can to be done by hand or other methods before the analyses. It can also be switched-off, if the Blaze is already removed from pre-reduced spectra and just an RV-measurement is desired.

In the second part of the program the relative velocity is calculated. At first the spectrum (y) is divided by the Blaze function (w), that was created in the first part of the program if this was not switched-off. The velocity calculation is done by shifting the spectrum until it matches to the template (f) best. All orders are Doppler-shifted by the same amount. As free parameters for each order of the spectrum, a slope (m) and the intensity (h) are fitted. To optimise this procedure the fitting is done iteratively in five steps, characterised by different step-widths in velocity. The step-widths vary from a large step-width, to find out roughly the drift (also if it would be about hundred km/s), to a fine step-width with $9\,\mathrm{m/s}$ separation. The latter determines the numerical accuracy of the program, which is much better than necessary for IMSs. Each step works in the same way: First the spectrum is

(a)   (b)
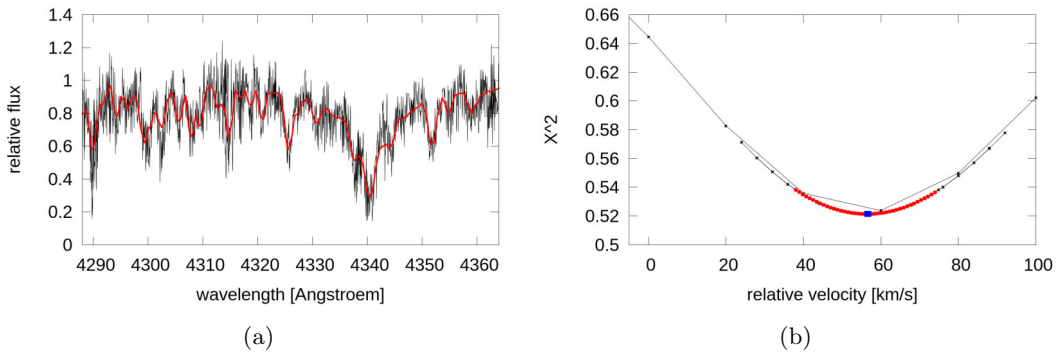
Figure 5.4: (a) Part of the reduced and Doppler-shifted spectrum of the candidate $LRa01\_E2\_1578$. The red line shows the fitted template. (b) The calculated χ^2 for the same spectrum. The different step-widths of the iterative method, are colour coded.

shifted by an initial value. This value is zero at the beginning and for each following iteration the "best shift" from the last, more rough, measurement is used. The best values for m and h are calculated by least square (χ^2) minimisation for each order. These values are adopted for the initial shift of the spectrum. Then the spectrum is shifted and the "best shift" is obtained by least squares optimisation:

$$\chi^2 = \sum_{j=1}^{norder} \frac{\sum\limits_{i=1}^{n} w_i (f_i - y_i(m_j, h_j))^2}{n}. \tag{13}$$

Equation 13 shows, how the χ^2 are derived. n is the length of one order, $norder$ is the number of orders used, for the fit. The Blaze-function w is used as a weighting function to account for the increasing S/N in the centre of the order. The calculation of m and h as well as the shifting is repeated 10 times, or until the "best shift" does not change anymore. This iterative procedure is done to optimise the calculation duration. It is much more efficient to calculate h and m separately than to optimise them together with the shift. Figure 5.4 shows an example of the fitting of the star LRa01_E2_1578. In this case a synthetic model is used to find the relative velocity. In the best case the determination of shift, m, and h is repeated twice per iteration, which takes 20 cycles. In the worst case it can increase to 50 cycles if no minimum can be found. This is only possible if the Template and spectrum are very different, for example if a template with a wrong spectral type was used or the S/N of

the spectrum is far to low. The algorithm has been tested with many spectra and has been shown to be very robust.

Finally the relative shift with a numeric precision of up to 9 m/s as well as the optimised parameters for m and h for each order are calculated. The output of this programme is the Doppler shifted as well as the not shifted spectrum with the blaze function removed, m, and h applied. This output is an ASCII table that still contains all values and the orders are separated. By combining the orders, an one-dimensional, rectified spectrum can be created. The shifted spectrum can be used to create a template of high S/N by combining all shifted spectra of the target star. The not shifted spectrum is just the rectified original spectrum in ASCII format. I can use it to cross check the results with other methods or do a line profile analysis.

5.3.2 Templates for comparison

As a first step, I use synthetic spectra derived from model atmospheres. The spectra were kindly derived by Holger Lehmann for several physical parameters and solar metallicity. The computed spectra cover $logg$ of 4.3 to 4.4 for T_{eff} from 6000 K to 8200 K in temperature steps of 200 K as well as $logg$ of 4.0 for $T_{eff} = 15500$ K for a B-star. He calculated all spectra for different $vsini_\star$ from 0 to 90 km/s. The line tables from the VALD database (Kupka et al. 2000) were used to calculate one-dimensional model-atmospheres with the assumption of local thermodynamic equilibrium (LTE). From these model atmospheres the synthetic spectra with a resolution of $R = 60\,000$ were calculated. This method and used codes are described by Lehmann et al. (2011). Since the spectral type of each candidate is known, I adopt the mean physical parameters of the spectral type (Gray 2005) and use the best matching synthetic spectrum as template. This template has the advantage that it can be used for the same star, even if it was observed with an other instrument. It also provides a zero point for the radial velocity determination. There can still be an offset of up to several hundred m/s, because of the different instrumental profile, which is not modelled in the synthetic spectrum. However, a constant offset in RV for all measurements is irrelevant for this work, because its aim is to detect companions by means of RV-variations, not to measure the absolute RV of the star.

Another approach is to use the stellar spectrum itself as template. The advantage is that the instrumental profile as well as uncertainties from the model atmosphere are ruled out as source of error. If the S/N is very high it is sufficient just to take one of the spectra out of the time series as template. With this approach, I obtain only a measurement of the relative radial velocity and have to apply an offset to match the dataset with the data from an different instrument.

If the S/N of a single spectrum is relatively low it is also possible to add all spectra of one target to get a high S/N spectrum for comparison. To do this, I first use the a synthetic spectrum as template to derive the RV-shift of each spectrum. Since the output of ASFIA is the shifted spectrum, I can now easily add all shifted spectra.

As a next step, I use it as template and calculate the relative velocity of each spectrum again. If the S/N is too low to create such a summed template, I use the synthetic spectrum as template only.

5.3.3 Measuring telluric lines

Ground-based spectroscopy suffers from the disadvantage that spectral features in the Earth's atmosphere are imprinted on the stellar spectrum. Kurucz (2006) published a high resolution spectrum of the absorption lines in the Earths atmosphere calculated by a model atmosphere. For a better visibility, the telluric features are increased in strength by a factor of ten.
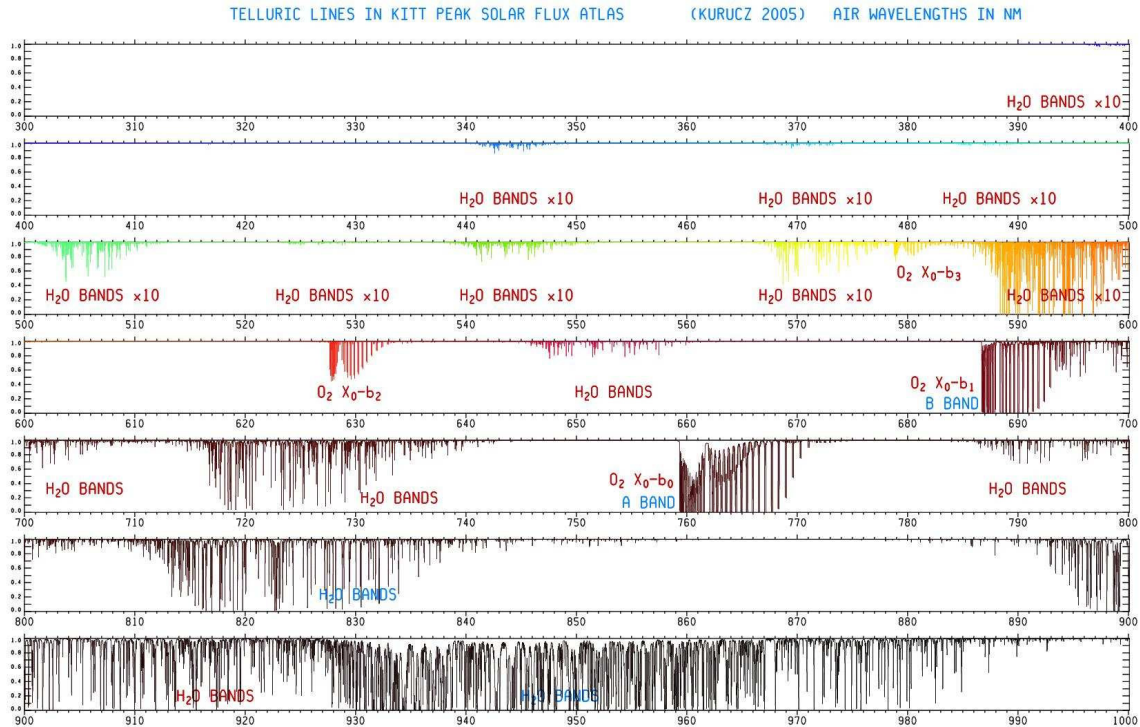
Figure 5.5: Calculated telluric absorption spectrum with labelled absorption features (Plot taken from Kurucz (2006)).

As can be seen in Figure 5.5 there are no telluric lines in the wavelength range, used for the SANDIFORD spectrograph. Telluric water vapour lines appear at longer wavelengths, thus, all high-resolution spectra taken with other instruments cover them. These lines are absorption lines from the atmosphere of the Earth. Starting from ~ 5880 Å, strong atmospheric lines from water vapour interfere the radial velocity measurement. Therefore, parts with strong telluric absorptions cannot be used for RV-measurements. Nevertheless, the telluric lines appear to be very useful. They do not follow the movement of the star and can thus be used as reference for wavelength calibration. Also if the ThAr calibration reaches high-precision it is still possible that systematic drifts are introduced. By monitoring the position of the telluric lines, I obtain a direct measurement of the difference between the internal ThAr calibration and the true shift of the spectrum applied to the instrument. Since telluric lines have the same path of light as the stellar spectra, they follow any drift introduced by the instrument or atmospheric distortions. For example, it is known that winds can introduce systematic shifts of ~ 20 m/s (Gray & Brown 2006).

So they appear as perfect markers to determine and remove these drifts in RV. Since early type stars do not show many intrinsic lines in the red and near infrared regions it is very easy to identify and measure the telluric lines accurately. I use ASFIA to measure the telluric

velocity and monitor the drift over the time series. Again, depending from the stellar flux of the target, I use as template either a synthetic spectrum or one spectrum composed from the spectra of the time series.In what follows, I will show typical drifts, observed with three spectrographs, used in this work. For CAFE, I use a time-series of the star HD 15082 that contains 7 consecutive spectra with S/N of about 60. For FIES, I use a time series of 18 consecutive spectra with S/N of about 30, taken from the star LRc07_E2_0307, during the transit of the planet (see section: 6.11). For UVES, I use a time series of 10 consecutive spectra, taken from the same star.

I also use the lines of three different O_2 bands for comparison, depending on the wavelength coverage of the instrument. Table 5.2 gives an overview on the wavelength ranges used to

Instrument	Lines [Å]	Mean drift [m/s]	Maximum difference [m/s]	Mean error [m/s]
CAFE	6276-6301.9, 6866-6904 and 7593-7642	31	90	17
FIES (med. res.)	6276-6301.9 and 6866-6904	42	135	16
UVES	6276-6301.9	89	288	16

Table 5.2: Telluric drift-measurements for three different spectrographs.

determine the telluric drift for the three instruments. The typical telluric drift as well as the maximum difference of the drift show, how strong these corrections are. The accuracy of the measurement depends on the S/N, the wavelength-range covered in the measurement, and the stability of the spectrograph. I measured the largest variations for the FIES spectrograph. In direct comparison to CAFE, this partly originates in the smaller wavelength coverage. Since the spectrograph is actively temperature controlled it is even more stable than CAFE. Nevertheless, Telting et al. (2014) pointed out that the RV-accuracy by using the medium resolution fibre is susceptible to variations of the seeing. This can be proven, by comparing the measured position of the telluric features with the airmass of the observation, as shown in figure 5.6. The instrumental shifts are systematically increasing with increasing
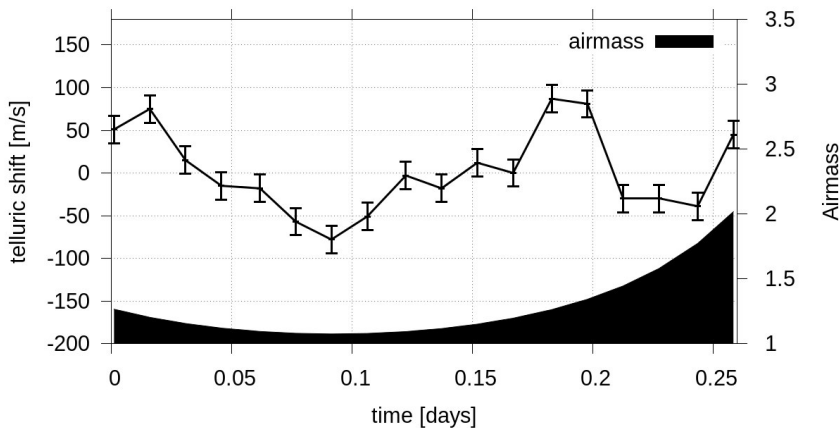
Figure 5.6: measured telluric shift of the FIES spectrograph over 6 hours consecutive observations.

airmass. This example shows that the correction of the telluric lines is very important to reach accuracies below 100 m/s. The largest shifts are measured with UVES. Within one night, the maximum difference is more than 280 m/s. This is consistent with D'Odorico et al. (2000), who measured a shift of ∼ 0.4 pixel/°C which corresponds to ∼ 200 m/s. The thermal

instability of UVES is the main limiting factor for this instrument. Except for spectra obtained with the SANDIFORD spectrograph, I thus apply the telluric correction to all spectra, by removing the measured shift from the RV-measurements.

5.4   Fitting Kepler orbits

To derive the mass of the companion from the RV-data, I implemented the least square fitting of the velocity curve to the data-points in a small python tool. To fit the velocity in the line of sight (see eq. (6) in Chapter 1.2.2) to a phase-folded dataset, K, e, and v_{r0} are constants, but the true anomaly is time depend and has to be calculated. I am starting from From Eq. (4) to calculate the mean anomaly. This introduces the orbital period as fixed parameter and the time after the pericentre passage. Afterwards, I have to solve the Keplers equation (5) to obtain the eccentric anomaly. This cannot be done analytically. I use a the iterative Newton's method to calculate it numerical (Meeus 1988). Newton's method is used to find the zeros of an equation. It is formally given by:

$$x_{n+1} = x_n - \frac{f(x_n)}{f'(x_n)}. \tag{14}$$

To find the zeros of equ. (5) this iterative method can be written as:

$$E_{n+1} = E_n - \frac{E_n - e\sin(E_n) - M}{1 - e\cos(E_n)}. \tag{15}$$

By using $E = M$ as start value this method converges typically with 3 to 5 iterations. Afterwards, I can calculate ν using equ. (3) and finally the velocity (equ. 6). Since the period is fixed, v_r can now be fitted to the data with $v_{r0}, K, e, t_p,$ and ω as free parameters.

The fit is weighted by the error-bars of the data-points. Up to three datasets can be fitted simultaneously by fitting their offsets due to different zero-points. Since often datasets obtained by different telescopes are combined, these can, thus, be fitted simultaneously. To lower the number of parameters, that are fitted, the eccentricity can be kept constant or zero. This is of practical relevance, since some time-series only contain a very few data points. The error of the fit is calculated if more than the minimum necessary number of data points are available. I use a bootstrapping method. That means one data-point is removed and the curve is fitted again. Then the next data point is removed an so on. This is done with all data-points to obtain a set of RV-curves. The maximum and minimum values of the fitted parameters are used to derive the error. Figure 5.7 shows the output of the tool. The data points are folded by the period and plotted as RV over the phase-angle. The ephemeris is given below as "T0". As This value corresponds to the transit time. Often the RV-values close to the transit are of special interest. Therefore, the plot is phase-shifted to show the transit at phase 0.5. It is marked by a black vertical line. Uncertainties in the orbital fit, calculated from the bootstrapping method, are shown as grey areas. Since the fit in Figure 5.7 is almost perfect those uncertainties are not visible. For example, Figure 6.1 in chapter 6 shows the uncertainties of the fit.

From the orbit-fit also a new value for the ephemeris is calculated, if the eccentricity is fitted as free parameter or kept different from the numeric zero (e.g. 10^{-7}).

From the parameters, P, K, e, and $M_\star$ the mass of the companion (M_P) is calculated. This is done by using the formula 1 in section 1.2. A first order determination of the mass can be derived by assuming that $M_P \ll M_\star$. This is true, if the companion is a planet. First I substitute:

$$L = \frac{K * P^{1/3}(1 - e^2)^{1/2}}{(2\pi G)^{1/3}}. \tag{16}$$

The mass can now be derived by:

$$M_P = L\, M_\star^{2/3}. \tag{17}$$

In the case of an eclipsing binary or a more massive companion this approximation is not valid anymore. To find the zeros of

$$0 = L\, (M_P + M_\star)^{2/3} - M_P, \tag{18}$$

the iterative Newton's method (14) can be written as:

$$M_{P,n+1} = M_{P,n} - \frac{L(M_{P,n} - M_\star)^{2/3} - M_{P,n}}{\frac{2L}{3(M_{P,n} - M_\star)^{1/3}} - 1}. \tag{19}$$

By using M_P, calculated from (17) as start-value this iterative method converges typically within 5 to 6 iterations. Since the spectral type of the host-star is known, the stellar mass (M_*) is taken from literature (Gray 2005). The planetary mass, as well as the error of the mass is calculated using these parameters.

5.5 Testing and accuracy of the RV-measurement

The accuracy of ASFIA can be tested by comparing the result obtained with this method to results obtained by other methods, found in the literature. It is also possible to obtain the error of the measurement by analysing the same spectrum in different wavelength regions and comparing the results. The errors, given in this work are statistical errors. They are obtained by the standard deviation of the values measured at different parts of the spectrum, divided by the number of measurements.

5.5.1 HD 209458

Mazeh et al. (2000) reported from RV-measurements the discovery of a close-in planet that orbits the solar-like star HD 209458. Furthermore, Charbonneau et al. (2000) discovered that it is a transiting planet. The star is a $G0$ V star and rotates slowly with $vsini_\star$ of about $4\,$km/s. It shows a radial velocity variation with a semi amplitude of $K = 86\,m/s$ in a $3.5\,$days period. This leads to a planetary mass of about $0.69\,M_{Jup}$. Wittenmyer et al. (2005) re-observed the star to include new measurements to the existing dataset. They confirmed the presence of radial velocity variations of $K = 83\,m/s$ which is within the errors of Mazeh et al. (2000). From this star 19 measurements were taken with HARPS between 2004 and 2010. Those were kindly provided during the ESO archive. This dataset was used to demonstrate the reliability of my method. The fitted values are given in Table 5.3.

I derived a semi-amplitude of $K = 82\,m/s$. With a mass of the host star of $1.16\,M_\odot$ this leads to a planetary mass of $0.68 \pm 0.01\,M_{Jup}$. This is in excellent agreement to the published

parameter	value	error
ephemeris [HJD]	2453344.78508	$+0.007 - 0.009$
v_{r0} [km/s]	-13.81905	± 0.00049
K [m/s]	82.03	± 0.79
e	1e-09	(fixed)
period [days]	3.52474859	(fixed)

Table 5.3: Parameters of the fit

ephemeris and semi-amplitude. Figure 5.7 shows the fit to the data as well as the deviations from the orbital solution. Since ASFIA is developed to analyse fast rotating stars with an accuracy of about $10^2 \, m/s$, a numerical resolution of $9 \, m/s$ is totally sufficient. The RV-deviation for HD 209458 is about $10 \, m/s$ and therefore, fulfils perfectly the expectations on the measurement. This test shows that my method works for the purpose of this work and even for very precise measurements on a solar-type star, for which it was not designed for.
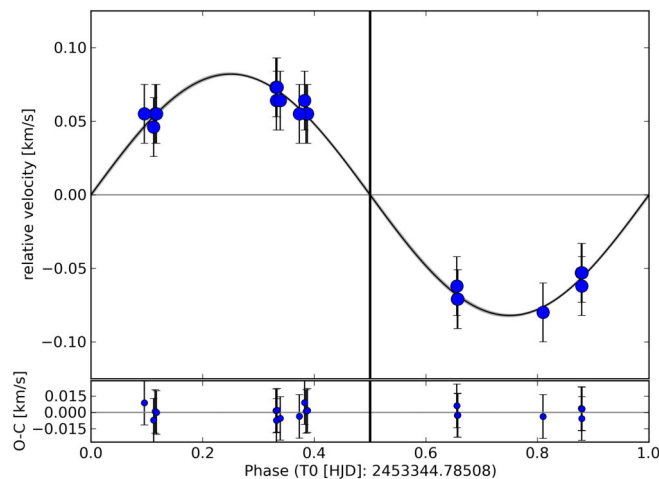
Figure 5.7: Radial velocity data of HD 209458. The black curve is the best fit to the data. The lower plot represents the residuals of the measurements.

5.5.2 Error estimates from early type stars

In a first version of ASFIA, each single order was fitted separately. Test values were obtained using the fast rotating A-star HD 15082, which is proven to harbour a close-in planet. I observed it with the CAFE spectrograph in 2012 before the CoRoT field was visible and in nights when the weather conditions were unsuitable to observe the faint targets. The star has a $vsini_\star$ of about $90 \, km/s$ (Cameron et al. 2010) and the CAFE spectra have a S/N of 50. The calculated shifts between the orders showed differences of about $4 \, km/s$.

This shows that for early-type stars it is not suitable to obtain the RV for each order separately, because each order contains a few lines only. For this type of stars it is much better to fit all orders simultaneously in a given wavelength range and use the blaze-function as weighting function to obtain RV-measurements with a reasonable accuracy. The error for each spectrum is obtained by comparing the blue part (3983.48 - 4940.5 Å) and the red part of the spectrum (4940.5 - 6863.23 Å+ 8680.5 - 8913.23 Å) separately using the same template.

Since there is no overlap in the used spectral region and the drift of the star is expected to be the same for all wavelengths both measurements can be taken as independent measurements of the radial velocity of the star. I calculate the statistical error for each spectrum and obtain an average error of 120 m/s for spectra with good S/N. Some spectra have lower S/N because of clouds, and have an error of up to 1 km/s. The target LRc07_E2_0307, is a medium fast rotating F-star of my sample. It has a $vsini_\star$ of about 20 km/s and by analysing the UVES spectra, I derived an average error of 50 m/s. These error estimates are consistent with the predicted accuracies, calculated above.

5.5.3   Significance of an orbital solution

An orbital fit based on RV-measurements is the best solution to the dataset. Especially, for RV-measurement with errors of the order of the measured amplitude it is important to find out, whether the calculated orbit is a significant fit to the data. An easy consistency check is to permute the RV-data arbitrarily and fit the Kepler orbit again. This is done for one million permutations. This simulates the influence of local errors in the data if for example the data from different times, but from almost the same phases are permuted in several parts of the RV-curve. The reduced χ^2 as well as the semi-amplitude from each fit is derived. If a solution with a smaller reduced χ^2 exists, the orbit solution is not unique and more data are needed to calculate the orbit. In this case from the maximum semi-amplitude the upper limit for the mass of the companion is derived. The false alarm probability is, thus, $P < 10^{-6}$ if no χ^2 exists that matches better to the data than the original fit. This method is used in cases with relatively large error-bars to prove the significance of the fit.

5.6   Doppler tomography

Both methods, the CCF and least-squares fitting method have considerable limitations. For pulsating stars with very high $vsini_\star$ the accuracy is limited not only by line-broadening, but also due to line-profile variations. For example, for the pulsating star LRa02_E1_1475, I used an other technique that focuses on the shape of the line-profile-variations and thus, on the source of the observed uncertainty (see section 7.2). The technique is another way to confirm that a transiting planet is not a false alarm. It has been developed by Cameron et al. (2010). In this method the star is observed spectroscopically while the planet is transiting. Because of the RM effect during the transit the planet causes a hump that moves though the line-profile.

By obtaining a time-series of spectra during the transit the presence of a transiting planet can be demonstrated. The motion of the hump can directly be translated and imaged into the movement of the object infront of the stellar disc. Therefore, this method is called Doppler-imaging or Doppler tomography. In contrast to the RV-method the advantage of this method is that is works best for rapidly-rotating stars. To measure the line-profile accurately, a mean line-profile is typically calculated using the method of Least-Squares Deconvolution (LSD). Basically, this method is a superposition of all spectral lines to increase the S/N. Assuming that the line-profile in velocity space ($Z(v)$) is the same for every line in the spectrum, than each spectrum can mathematically be described as a sum of delta-functions at the line-positions weighted by their relative strengths ($M(v)$), cross correlated by the line-profile.

In matrix notation this can be written as (Donati et al. 1997):

$$V = M \cdot Z. \tag{20}$$

To obtain the least-squares solution (Z), this expression can be re-written as:

$$Z = (M^t \cdot S^2 \cdot M)^{-1} \ M^t \cdot S^2 \cdot V, \tag{21}$$

while S is a diagonal matrix, containing the inverse uncertainty per pixel element in the observed spectrum, which is used to deconvolve the cross correlation and, thus, "clean" it. Actually, by using the calculated line-shape and optimizing the weights for the delta-functions, the spectrum can be re-modelled again with a factor of 5 to 15 higher S/N and without a loss of resolution (Tkachenko et al. 2013).

The limiting effects are the line strengths. The line strengths are calculated from synthetic stellar atmospheres that matches to the observed physical properties of the star. Due to different abundances the strength of single lines can therefore differ from the observed ones. Another limiting effect is the assumption that all lines in the spectrum show a similar line-profile. For example, the shape of the Hydrogen lines of stars with strong magnetic fields are affected by the Stark effect while other lines are not affected. Pulsating stars show distortions in the line profiles that change from line to line. This can be explained from movements of material due to the pulsations. Individual lines originate in different heights in the stellar atmosphere. Node-lines of pulsations lead to lines that are blue shifted or red shifted, according to the velocity field in the height where they are formed. Furthermore, the wings of the lines origin is deeper layers than the cores. Different velocities in different heights does not only lead to lines with shifted RV-velocity, but also to distortions of the line due to RV-shifts in different parts of the line. A careful investigation of the distortions of different lines can unveil the pulsation profile of the atmosphere (Kurtz et al. 2005). The LSD-profile in return gives an integrated line-shape that is imprinted by all visible frequencies of the star and will therefore, show time-depended line-profile variations. In the case of Doppler tomography this result can be used to directly map the pulsation pattern of the star and calculate the integrated stellar frequencies per velocity-bin.

I developed a small python tool that uses a line list, obtained by Timothy Van Reeth (private communication) from the Vienna Atomic Line Database (Kupka et al. 2000, VALD) with a weight for each single line. This weight is adopted to match the stellar properties of a star with T_{eff}=8000 K, logg=4,0, and solar metalicity. The tool averages all lines according to their weight in velocity space to obtain a singe mean-line profile. The lower panel of Figure 5.8 (a) shows an example for a LSD-profile which was calculated for HD 15082. I observed this star with the SANDIFORD and CAFE spectrographs. As a consequence of the δ-Sct like pulsations, each single spectrum contains several humps that move over the profile within several hours. The spectrum shown (blue in the upper panel of Figure 5.8 (a)) is the combined spectrum of all 77 SANDIFORD spectra with sufficient S/N, resulting in an almost symmetric line-profile. The Balmer lines as well as unsuitable parts of the spectra are not used for the deconvolution. The line list that I used for calculation is plotted for comparison as black line forest in the upper panel. I used this mean line-profile to remove it from all single profiles from the time series of spectra. This method allows me to visualise
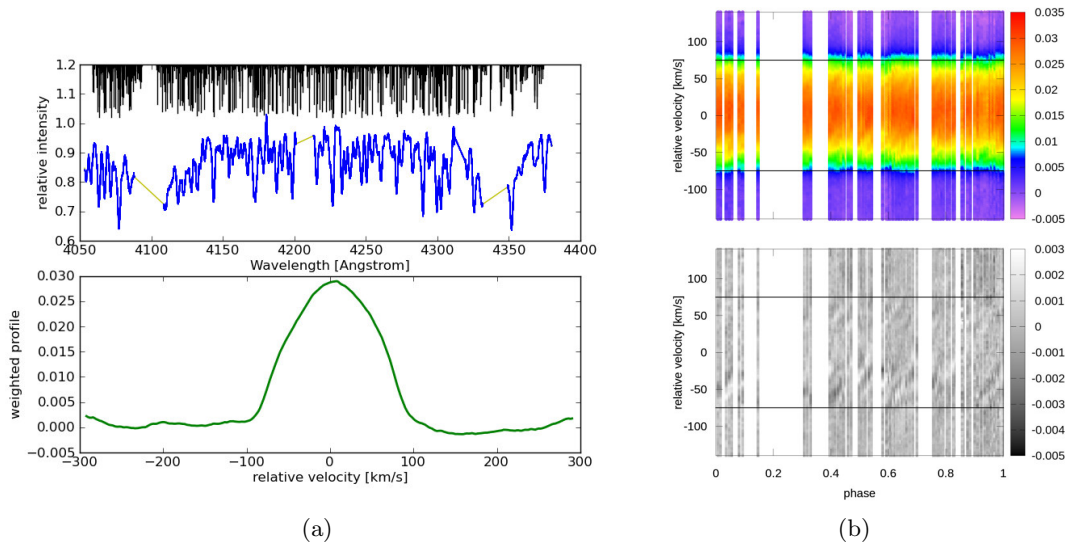
Figure 5.8: LSD-profiles of HD 15082, (a) Calculating of a LSD-profile. Upper panel: Mean spectrum of HD 15082, obtained with the SANDIFORD spectrograph (blue). The Balmer lines, as well as the scattered light at 410 nm is not used for deriving the LSD profile. Black lines: the line-list used for comparison. Lower panel: the mean line-profile; (b) All 77 LSD-profiles of HD 15082. Upper panel: the profiles, folded over the planetary orbit with black lines indicating the position of the line-wings, Lower panel: the same profiles in the same scale with the mean line-profile removed.

the pulsation pattern and also the moving hump during the transit. Figure 5.8 (b) shows the time series of line-profiles, phase folded to the transit period. I used the ephemeris $T_c = 2454163.22373$ HJD, published by Cameron et al. (2010) and phase shifted the transit mid-time to phase 0.5. In the lower panel of Figure 5.8 (b), I removed the mean line-profile to show the deviations over time. This figure shows the pulsations of the star. Unfortunately, the time resolution is not sufficient to see the planetary signal in this data.

Lehmann et al. (2015) finally used a set of 287 spectra of the high-resolution spectrograph at TLS to visualise and measure the frequencies of the star per mass bin, using the method described by Tkachenko et al. (2013). The basic idea of this method is that the line-profile not only contains the information of the pulsation, but also the RV-signal. In order to obtain precise RV-values, I measured the position of the profile in velocity space and included the distortion of the shape. I wrote a python-script for carrying out these calculations by using three different methods. The first method fits a simple Gaussian to the profiles. In the second method, I first derive the gradient of the profile and then determine the zero-point from it. To derive the gradient even from profiles with low S/N, I first fit a spline function with adjustable order to the profile. The third method is to derive the integral of the right- and left-hand side of the absolute value of the gradient and shift the centre until both integrals differ minimal from each other. The midpoints of all three method are calculated and can be compared. The last two methods are almost similar and can be called the "median of the profile". Strong differences between the first and the two other methods give a measurement how strong the profile is distorted. None of these methods gives a RV-value that is independent from the pulsation, but can be used in two ways. (1.) If many spectra exist the derived values can be compared to select spectra with low distortion of the line-profile. These spectra can finally be used to derive the radial velocity with CCF or least-squares minimisation. (2.) if

the pulsations are equally distributed over the line profile the integral method would give a precise RV-measurement which is independent from the pulsation pattern.

In a further approach the measured frequencies and amplitudes of the pulsations might be used to clear single profiles from the pulsation patterns and measure the radial velocity in detail.

6 Results of radial velocity measurements

RV-measurements were taken to obtain a confirmation and to derive the mass for each transit candidate in this programme. Therefore, the RV-measurements are first phase-folded to the orbital period known from the light curve. Second, the measurements are corrected for instrumental shifts and heliocentric velocities introduced by the movement and rotation of the Earth. Third, to calculate the semi-amplitude of the RV-velocity, the data taken from different observatories are merged and the RV-variation corresponding to a physical orbit is fitted. Finally, the mass of the companion is derived from the semi-amplitude of the fit to the data. This chapter gives an overview to all RV measurements of the transit candidates and, thus, some preliminary conclusions to the nature of the companion, like the companion mass or upper mass limits. The measurements can be found in Tab. A1.1 in the appendix. The first two objects that I like to discuss have been identified as stellar companions from the transit parameters and thus, serve as test cases for the mass-determination.

6.1 LRc02_E1_0132

A close investigation of the phase-folded light curve reveals that the main transit originates likely from a grazing eclipse. It shows an eclipse-depth of 11 %. Furthermore a secondary eclipse with a flat bottom is visible. That means the main component has a larger radius than the secondary component. Therefore, the secondary component is not visible during the secondary transit. The light curve shows intensity variations that origin likely from δ-Sct like pulsations. Since the system also shows pulsations during the secondary transit, those originate likely from the main component. From the analysis of the light curve, the object is very likely a binary with an early-type main component. Both stars have an extremely small separation with a semi-major axis of $1.8\,R_\star$. To find sub-stellar companions of a pulsating IMS with the used set-up very high precision is needed. This test shows the accuracy of the SANDIFORD spectrograph. As shown in Figure 6.1 the SANDIFORD spectra cover the orbit
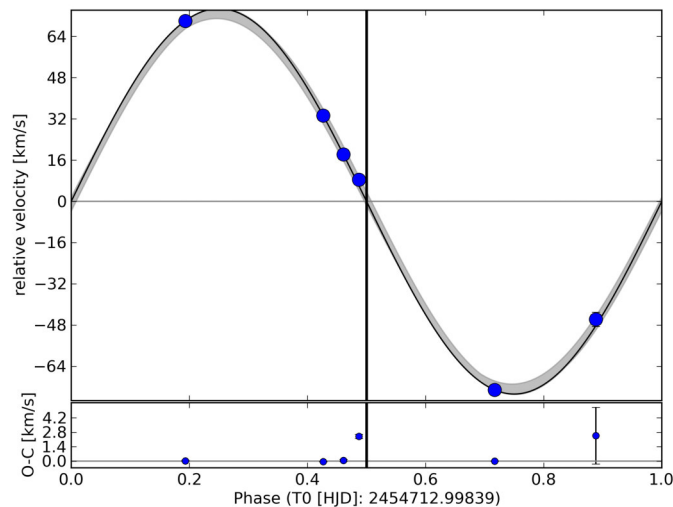
Figure 6.1: Orbital fit of LRc02_E1_0132

of 3.7 days very well. The semi-amplitude of 75 km/s is consistent with a binary-solution.

parameter	value	error
ephemeris [HJD]	2454712.99839	±0.031
v_{r0} [km/s]	-19.629	±2.86
K [km/s]	74.80	±2.018
e	1e-11	0.0
period [days]	3.6946	(fixed)

Table 6.1: LRc02_E1_0132: Parameters of the orbital fit.

The parameters of the orbital-fit are given in Table 6.1. The method to calculate the mass of the companion from the amplitude of the RV-measurement and the mass estimate for the primary component (see Table 4.4) is explained in section 5.4. I obtained a mass of the secondary star of $m \sin\ i = 1.173\,M_\odot$. Two data points do not match the fit perfectly. The one at phase 0.88 has a stronger uncertainty because of low S/N. The point at phase 0.49 was obtained during the transit of the object and, thus, indicates a drift due to the RM effect. The star was also observed spectroscopically by da Silva et al. (2014). Using stellar models they derived a mass for the primary component of $2.25\,M_\odot$. This is 12.5% higher than my first estimate. By using this higher mass of the primary, I recalculated the mass of the secondary and obtained $m \sin\ i = 1.253 \pm 0.084\,0.003\,M_\odot$. This is fully consistent to the secondary mass of $1.3\,M_\odot$ obtained by da Silva et al. (2014). Apart from the two outliers the mean deviation from the circular orbit is about $60\,\mathrm{m/s}$. This is sufficient to detect orbits with a semi-amplitude of $180\,\mathrm{m/s}$ with a $3\,\sigma$ accuracy and, thus, to detect a $2.2\,M_{Jup}$ planet in a $3.7\,\mathrm{days}$ orbit of a $2.0\,\mathrm{M}_\star$ with $v \sin\ i_\star \sim 20\,km/s$.

This demonstrates that using ASFIA I can derive the mass of binaries of early-type stars with high precision. Furthermore, it shows that the accuracy of the SANDIFORD spectrograph is sufficient to detect massive planets around IMSs.

6.2 LRa01_E2_1578

The analysis of the light curve of this star shows a shallow and v-shaped transit with a depth of $\sim 0.5\,\%$. The intensity increases by $\sim 0.3\,\%$ just before the transit. This increase in flux might be originated from the effect of periastron brightening. This effect is known from eccentric binaries (Hareter et al. 2014). It can be explained due to reflected light and gravitational distortions due to a nearby stellar companion during its periastron. Four SANDIFORD spectra have been obtained and show strong RV-variations with a semi-amplitude of up to $74\,\mathrm{km/s}$. A sub-stellar companion is therefore excluded. The orbital fit does not match a circular orbit, but has to be eccentric. Since only four spectra were obtained several eccentricities would fit the data. Thus, only the lower limit for the semi-amplitude of $45.4\,\mathrm{km/s}$ can be derived by choosing the orbital fit with the smallest possible eccentricity of e = 0.55 (see Figure 6.2 (a)). From this fit, I derived a lower mass limit of $m \sin\ i = 0.75\,M_\odot$ for the secondary companion. This measurement is consistent with the scenario of an eclipsing eccentric binary with a secondary component in the mass regime of a G -K type dwarf star. This example shows that an increasing intensity in the light curve before or after the transit is a strong indication for an eccentric binary.

(a)

(b)
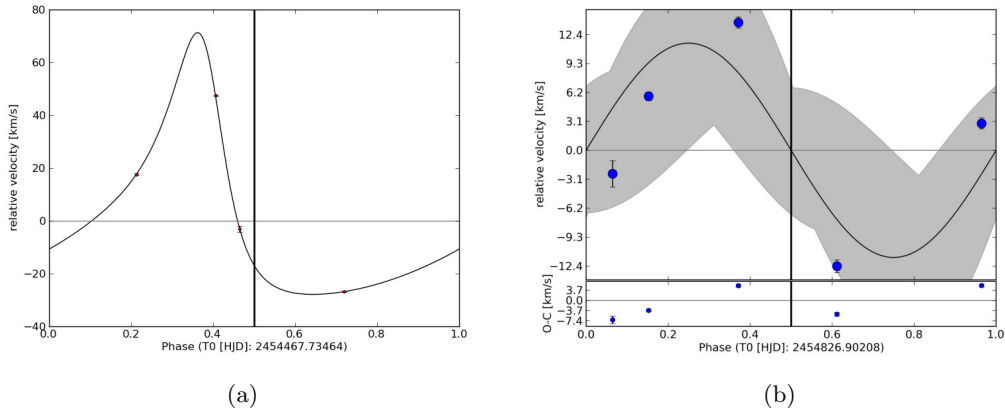
Figure 6.2: (a) Orbital fit of LRa01_E2_1578 (b) Orbital fit of LRa02_E1_0725.

6.3 LRa02_E1_0725

The light curve of this target shows an increasing intensity directly after the transit. This effect might be caused by periastron brightening, like in the case of LRa01_E2_1578. Nevertheless, the transit-depth, and shape with a flat-bottom, and the fact that no secondary transit is seen are in agreement with a 2.1-R_{Jup} object. Thus, the light curve shows characteristics an eccentric stellar companion or a massive sub-stellar companion. If this companion would be a planet, it shows extremely strong flux variations originating from reflection-, Doppler beaming-, or ellipsoidal variations. The five SANDIFORD spectra show a maximum RV-difference of 26 km/s obviously indicating that the star is a binary. The parameter for the best fit of the 9 days orbit are given in Table 6.2.

parameter	value	error
ephemeris [HJD]	2454826.9	-52.26 +1.27
v_{r0} [km/s]	31.69	±7.25
K [km/s]	11.47	±6.91
e	0	(fixed)
period [days]	9.0968	(fixed)

Table 6.2: LRa02_E1_0725: Parameters of the fit.

With a stellar mass of 2.05 $M_\odot$ for the main component, the companion is a stellar object with $m \sin i = 0.19 \, M_\odot$ -/+ 0.08 0.17 $M_\odot$. This is consistent with a very late M-dwarf. As shown in Figure 6.2 (b), the errors of the measurements are relatively small, but the deviations from the orbital fit are rather large. Since an eccentric orbit does not successfully fit to the data, these deviations cannot be explained only from an eccentric orbit. It could be caused by stellar activity (see section 6.16) or by a third body in the system.

6.4 LRa01_E2_0203

With an apparent magnitude of V=11.5 mag this star is relatively bright. The light curve shows a shallow transit with a transit-depth that would correspond to a size of only 3 R_{Earth}. This makes this object extremely interesting. The star exhibits a fast rotational velocity and a period of 1.86 days. With a mass of the host star of 1.6 $M_\odot$, a planet with 0.1 M_{Jup}

that corresponds to a dense planet with $3\,R_{Earth}$ would induce an RV semi-amplitude of only $12\,\mathrm{m/s}$. that means an accuracy of $8\,\mathrm{m/s}$ is needed to detect such an RV-variation. This is far below the accuracy of the SANDIFORD spectrograph, but the measurements can be used to exclude false alarms. Data were obtained in two runs with the SANDIFORD spectrograph separated by one year. There is no significant offset between the mean radial velocities of both datasets. The star was also observed with the CAFE spectrograph. To include the CAFE-data, an instrumental offset of about 7.5 km/s had to be added. As shown in Figure 6.3 (a) the RV-measurements differ in the order of several km/s. The blue and red data origin from the SANDIFORD runs and the green data from the CAFE run. For the period of the transit no significant orbital-fit can be applied. The upper mass-limit derived from the RV-variations is $m\sin\ i = 12\,M_{Jup}$.

(a) (b)
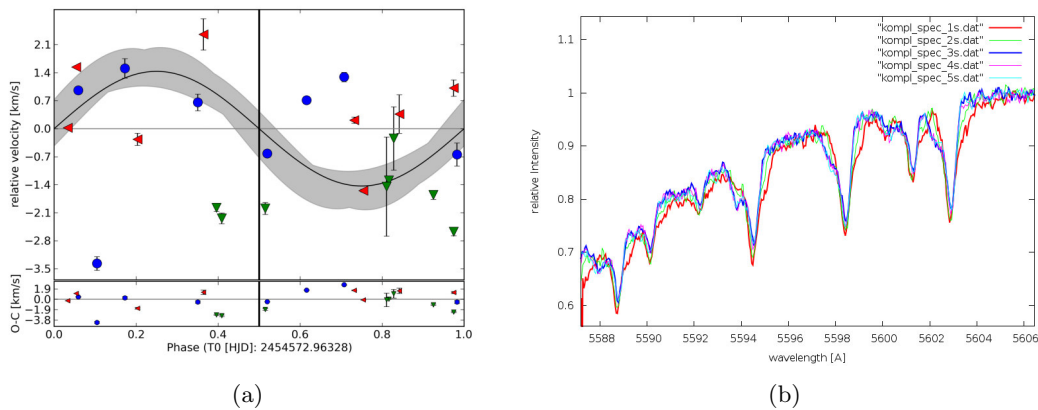
Figure 6.3: LRa01_E2_0203: (a) orbital fit to SANDIFORD (blue and red) and CAFE data (green) (b) UVES spectra, showing obvious changes in the line-shape, consistent with a double lined spectroscopic binary.

In order to derive the mass of the companion high-resolution spectra were obtained with the UVES spectrograph. Those have a much higher S/N than the SANDIFORD and CAFE spectra and, thus, allow one to measure the RV with higher precision. Surprisingly these data show variations of up to 10 km/s. This means that this object is a binary. Furthermore, the spectra reveal a double lined spectrum of a binary (SB2-binary). In Figure 6.3 (b) three UVES spectra are presented that show different orbital phases of the binary covered by UVES. The contaminating star is visible in the wings of the lines. The shape of the wings changes significantly with orbital phase. With P > 84 d the period of the binary is much longer than the transit period, but since the stellar companion affects the spectra, it is not possible to analyse the spectra with the accuracy needed to detect a planet. Furthermore, from a new analysis of the light curve pulsations with a similar frequency than the transit-duration were detected. The binary signature in the spectra as well as the pulsations confirm that this object is a false alarm.

6.5 LRa02_E2_4150

This is one of the most interesting candidates of this programme. The light curve is dominated by pulsations with an amplitude of $\sim\ 1\,\%$ and shows a planet-like transit (see section 7.2).

Since the period is 8.17 d the semi-amplitude of the companion would be in the order of 500 m/s by using the companion size and mass of the host star (see Table 4.4) and the assumption of a Jupiter-like density. Due to the fast rotational velocity ($v \sin i_\star \sim 80\,\mathrm{km/s}$) is not feasible to detect such a signal with the SANDIFORD spectrograph. Nevertheless, the accuracy of the spectrograph is sufficient to exclude a binary. Spectra of this star were obtained in two runs with SANDIFORD separated by one year. Although an orbital fit did not converged, I obtained an upper mass limit for the companion of about 70 M_{Jup} (see Figure 6.4 (a)). To obtain the mass of this object spectra were taken with the CAFE, FIES, and HARPS spectrographs. I first analysed the datasets from each spectrograph separately and obtained best orbital fits that correspond to a companion in the brown dwarf mass-regime.

(a)   (b)
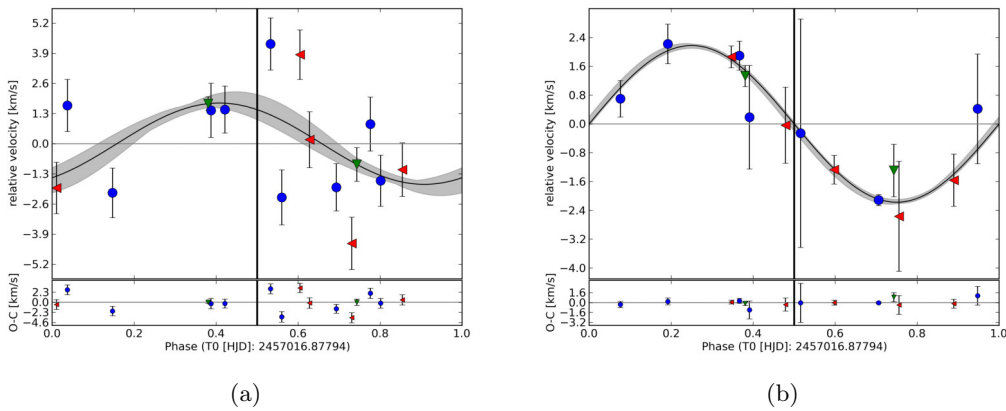
Figure 6.4: LRa02_E2_4150: (a) orbital fit to SANDIFORD data (b) orbital fit to CAFE, FIES, and HARPS data.

Run	Mean time [HJD]	Offset [km/s]
CAFE	2456280.93	0.0
FIES	2456284.18	-6.5
FIES	2456297.68	-9.62
HARPS	2456331.07	-9.34
CAFE	2457020.80	-14.53

Table 6.3: Offsets, used for different datasets.

To confirm the sub-stellar mass of the companion with high precision all data-sets are combined. Interestingly the offsets between different data-sets change almost linearly with time. This behaviour implies the presence of a stellar companion with a long period (see Table 6.3). Deviations of the offsets from the linear trend that origin from the stellar companion result from different data-processing and instrumental drifts. To correct for those effects the offsets from different observation campaigns and instruments are matched together with the orbital fit. The results are shown in Figure 6.4 (b). The CAFE-data are blue, the FIES data red, and the HARPS data are green. From this fit, I derive the mass of the companion of $m \sin i = 63.46^{+1.63}_{-2.23}\,M_{Jup}$. The parameters from this orbital fit are shown in Table 6.4. The ephemerides are calculated from the RV-orbit. These deviate only by 3.75% of the orbit period from the photometric ephemerides obtained from the CoRoT light curve. This confirms that the RV-variations are directly connected to the transits found with CoRoT. The

significance check to the orbital fit (see section 5.5.3) reached an χ^2 that is twice the value of the original fit after one million permutations. This means the orbital fit is highly significant with a false alarm probability of $P < 10^{-6}$.

parameter	value	error
ephemeris [HJD]	2457016.87794	-0.032 +0.116
v_{r0} [km/s]	42.98	±0.07
K [km/s]	2.17	±0.07
e	0	(fixed)
period [days]	8.1703	(fixed)

Table 6.4: LRa02_E2_4150: Parameters of the fit.

6.6 LRa01_E2_0963

The light curve of this candidate shows shallow transits with a depth of 0.06 % and a period of 4.8 days. Since this translates to a Neptune-sized object, it is a very interesting planet candidate. The upper mass limit derived from the SANDIFORD spectra is in the planetary regime. I therefore devoted the service observations with CAFE in 2013 entirely to follow-up this object and obtained finally a sufficient phase-coverage of RV-measurements. Unfortunately, in the service mode observations no attached ThAr exposures were taken. Nevertheless, using telluric features, I measured the instrumental drift within the night and corrected for it. I analysed the RV-data and found that the maximum possible amplitude is about 1.4 km/s using a circular orbit. The best eccentric orbit has an amplitude of 1.5 km/s with an eccentricity of e=0.55. From these results, I derived a maximum companion mass with $m \sin i = 17 \, M_{Jup}$. This places the object in the region of very massive planets and therefore in the transition-region towards brown dwarfs. This result is surprising. Since the size of the object is only about $0.4 \, R_{Jup}$, the density would be 260 times higher than the density of Jupiter. According to Hatzes & Rauer (2015), such a density is expected for objects at the border between massive brown dwarfs and low mass stars. This indicates that the stellar parameters of the star might be underestimated or the object is a false alarm. To solve this inconsistency, the star was observed using the FIES spectrograph. The combined observations lead to the conclusion that the star has to be a long periodic binary. As shown in Figure 6.5 (a), the influence of the binary in radial velocity can be corrected by removing an linear slope. Additionally an offset of 1.16 km/s has to be removed between the two instruments. As shown in Figure 6.5 (b), the orbital fit of 4.6538 days does not match to the final data. Red points are CAFE-, blue points FIES-, and green points are the SANDIFORD-measurements. A maximum semi-amplitude of 0.87 km/s is derived which corresponds to an upper mass limit of $m \sin i = 10 \, M_{Jup}$. In a revised analysis of the transit Sascha Grziwas pointed out that the transit might be caused by an disruption in the light curve and would therefore possibly be just an artefact. Given this new analysis of the light curve, it is very well possible that this object is a false alarm, rather than a star with a planet.

6.7 LRa02_E1_1475

With an estimated size of $0.9 \, R_{Jup}$ and a period of only 2.12 days, this is a good candidate for a close-in planet of an A-type star. Using ASFIA, I analysed high resolution spectra that

(a) (b)
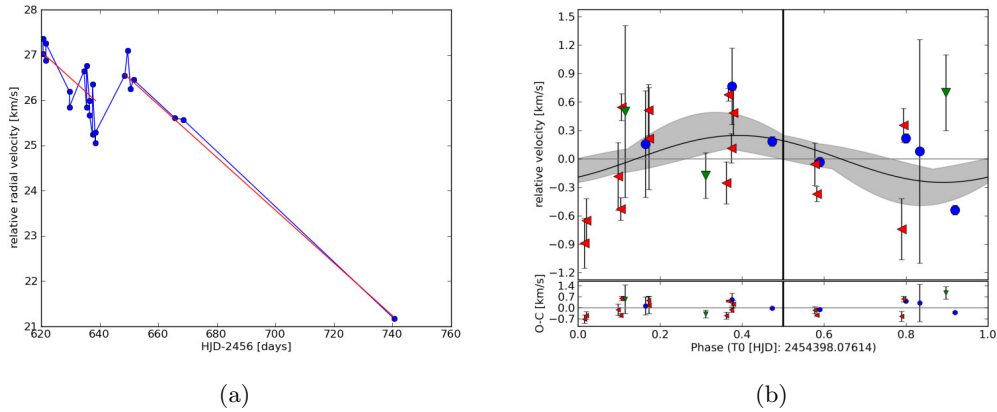
Figure 6.5: LRa01_E2_0963; (a) The data over a long time-series show a linear trend the binary signal (plus offset between data-sets). (b) Orbital fit to the data from different instruments.

were obtained with the HIRES-, HARPS-, and UVES- spectrographs. The star shows an very fast rotational velocity of about $v \sin i_\star \sim 160\,km/s$. As shown in Figure 6.6, the scattering between different measurements is in the order of several km/s, but the accuracies obtained for single spectra is in the order of $100\,m/s$ or less. A circular orbit with an semi-amplitude of $6.3\,km/s$ fits best to the HARPS data. Thus, by using a stellar mass of $1.98\,M_\odot$ (see section: 7.2) the mass of the companion is $m \sin i = 62.9\,M_{Jup}$. This result confirms a sub-stellar companion in the regime of massive brown dwarfs.

The deviations of the RV-measurements from the orbital fit are caused by pulsations of
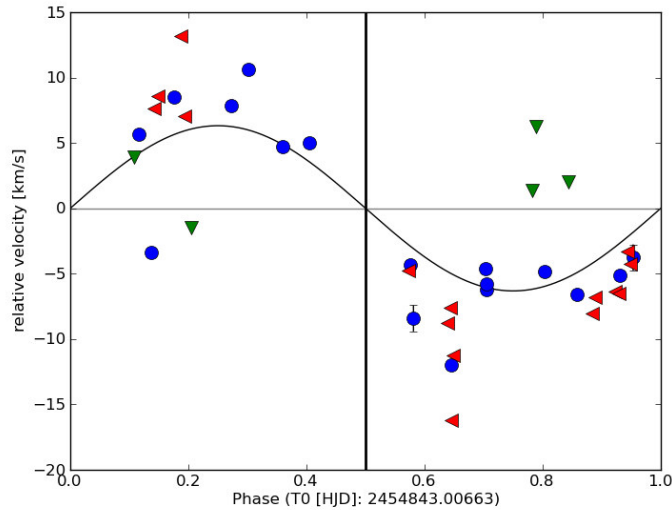
Figure 6.6: RV-measurements via the Least-squares fit method. blue: HARPS, red: UVES, green: HIRES.

the star. The CoRoT light curve shows pulsations with variable intensity. These have a period of $0.7\,d$, which corresponds to one third of the orbital period. These pulsations change the shape of the line profile. The RV-measurements are expected to be strongly affected by the oscillations. Particularly problematic is that the orbital period is a multiple of the pulsation frequency. To measure the effect of the pulsations to the line profiles, I analysed

the LSD-profiles of the spectra (The method is described in section 5.6). The line list was kindly provided from Christian Heuser who calculated it from his stellar analysis from high-resolution spectra. The centre of the line-profile was determined by two different approaches. First the median of the profile was calculated and second the profile was fitted to Gaussian function. The measurements are different in almost all spectra obtained from the star. Those variable differences occur from line-profile variations due to pulsations. To determine the RVs from the profile, I used the centre of the Gaussian fit. The error of the measurement is derived from the standard deviation of the two measurements. I analysed each dataset separately since I obtained an almost complete phase coverage from each instrument. Figure 6.8 (a-c) shows the separate orbital fits. The derived masses are in the transition regime of massive brown dwarfs and very low mass stars. For HARPS-, HIRES-, and UVES-data, I derived 91, 80, and 66.9 M_{Jup} respectively. By combining all datasets (see Figure 6.8 (d)), including instrumental offsets between them, I finally derived a mass of $m \sin i = 77.30^{+4.57}_{-4.07} M_{Jup}$. The parameters of the fit are given in Table 6.5.

parameter	value	error
ephemeris [HJD]	2454843.00843	$+0.033 - 0.019$
v_{r0} [km/s]	36.34	± 4.9
K [km/s]	7.702	± 3.46
e	1e-11	(fixed)
period [days]	2.1183	(fixed)

Table 6.5: LRa02_E1_1475: Parameters of the orbital fit.

The significance check to the orbital fit (see section 5.5.3) reached an χ^2 that is 1.3 times higher than the value of the original fit after one million permutations. Thus, the orbital fit is highly significant with a false alarm probability of $P < 10^{-6}$. Furthermore, since the measurements show the same signal for a time of 3,1 yrs, it is a robust confirmation that the companion is a sub-stellar object close to the border to a low mass star.

6.8 LRa02_E2_1023

From the light curve the companion might be a very close-in planet with half the size of Jupiter. The RV amplitude of a $1 M_{Jup}$ mass planet would be 180 m/s. The test on LRc02_E1_0132 showed that it is possible to detect such an RV-signal already with the SAN-DIFORD spectrograph. I obtained four consecutive spectra of this target with SANDIFORD. The star is relatively bright and a slow rotator ($v \sin i_\star \sim 12\, km/s$) with many sharp lines. The statistical errors obtained from the measurements are, thus, with about 25 m/s very small. Nevertheless, due to instrumental flexure the accuracy of the radial velocity measurements is on average 100 m/s. This accuracy can easily be measured by comparing the wavelength calibration before and after the measurement. This means this instrument is essentially limited by instrumental shifts. The first three spectra show a very small RV-variation. A circular orbit with a semi-amplitude of 0.9 km/s (see Figure 6.8 (a)) would fit to the data. This is consistent with a $5.3 - M_{Jup}$ planet orbiting in a 0.78 d orbit. Nevertheless, the last measurement does not match the fit. It differs by 17 km/s from the other measurements. Mathematically, it can only be fitted by an keplerian orbit with a high eccentricity of $e = 0.6$. As shown in Figure 6.8 (b), this orbit has a semi-amplitude of 9 km/s

(a)　　　　　　　　(b)　　　　　　　　(c)

(d)
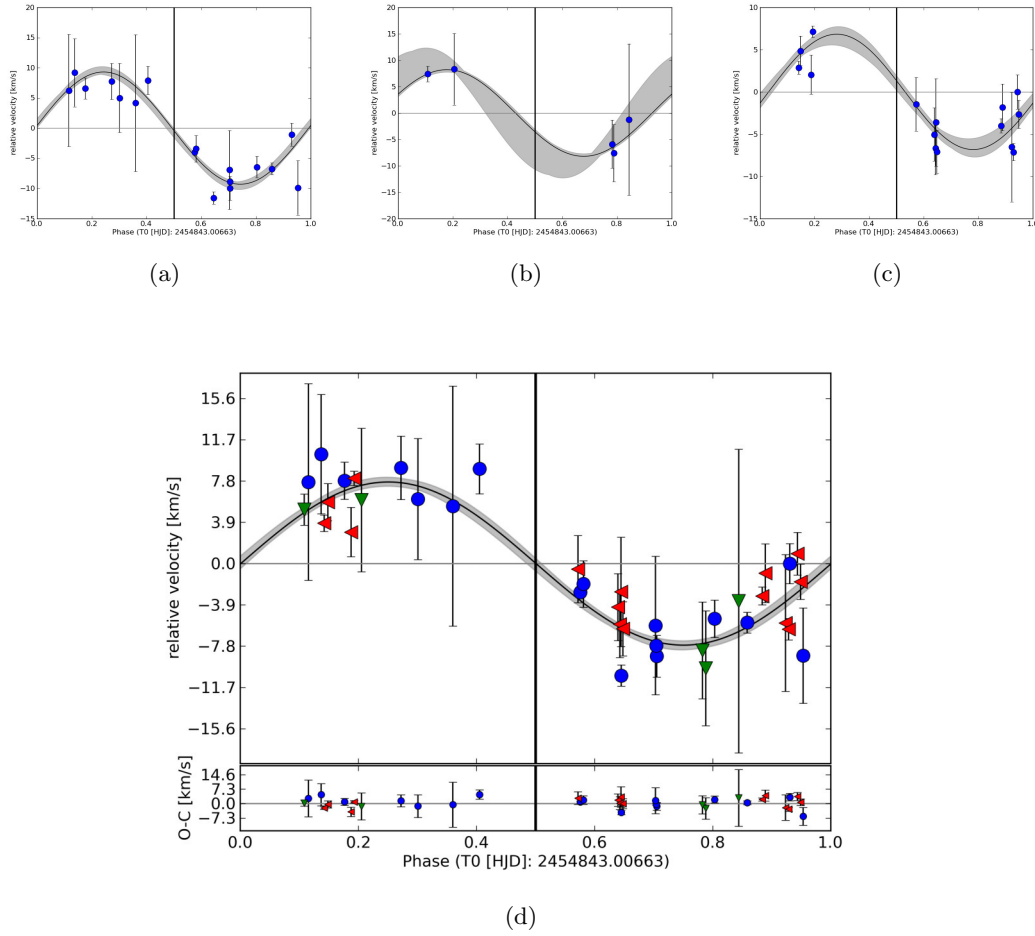
Figure 6.7: LRa02_E1_1475: orbital fits to RV-values from LSD-profiles; (a) only from HARPS (b) only from HIRES (c) only from UVES (d) combined fit of all instruments, Offsets to HARPS data: HIRES: -0.96 km/s, UVES: -1.0 km/s.

which is consistent to a companion with $m \sin i = 42\,M_{Jup}$. A very close-in brown dwarf in an eccentric orbit has to be very young. Otherwise its orbit would have been already circularised by tidal forces. Since the transit seems to be extremely v-shaped, the object is likely to be grazing. On the other hand, the observed transit-duration is comparable to the derived maximum possible transit-duration. This is inconsistent with a v-shaped transit. The observed transit-time for a grazing object is expected to be much shorter than the maximum duration. This behaviour is consistent with a background binary. The line-profile of the last spectrum is 28 % deeper and less broadened than the other spectra. This strong line profile variation cannot origin from the movement of a sub-stellar companion. Nevertheless, even if the CFHT-image does not show a nearby star, regarding up all the evidences, I conclude that this object is likely to be a false alarm than a planet.

6.9　LRc03_E2_2657

The analysis of the light curve shows a transit that is consistent to an $0.7\,R_{Jup}$ planet in a 5 d orbit. I first obtained spectra with the TWIN spectrograph. The accuracy of this spectrograph is not enough to detect the planet, but it would detect the RV-signal of an binary. From TWIN data I measured promising RV-variations with a semi-amplitude of
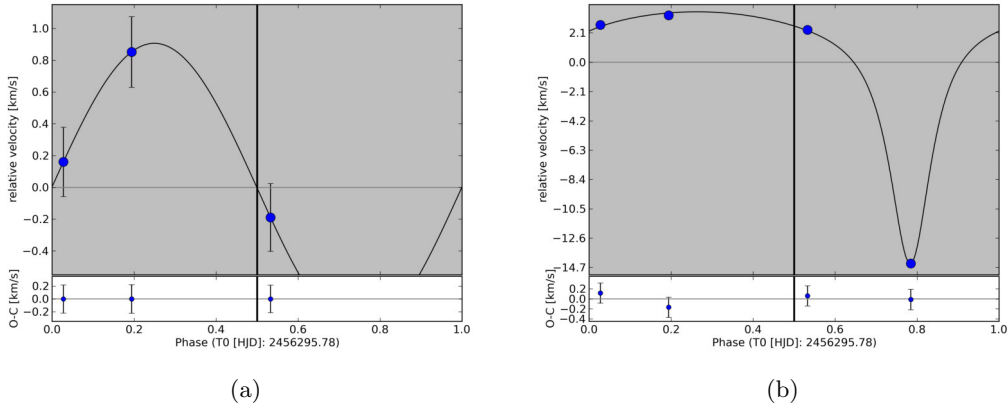
Figure 6.8: LRa02_E2_1023; (a) sinodial fit to three SANDIFORD spectra; (b) Fit of a eccentric orbit to all SANDIORD spectra.

4.8 km/s (see Figure 6.9 (a)). By using a stellar mass of $1.93\,M_\odot$ I derived a mass of the companion of $m \sin i = 60\,M_{Jup}$. To determine whether this interesting object is a low-mass stellar companion or a high-mass sub-stellar companion more data with higher precision are needed. Therefore, spectra were obtained with UVES and two HARPS spectra were provided from the ESO archive. To measure the RVs from these spectra is challenging. The
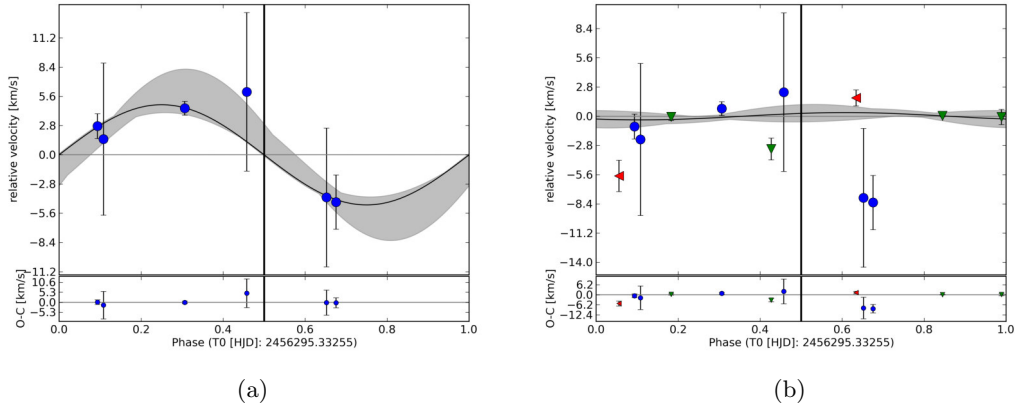
Figure 6.9: LRc03_E2_2657 (a) Orbital fit to the TWIN spectra ,(b) Orbital fit, including also UVES and HARPS spectra.

least squares and LSD methods show strong deviations from any orbital fit and furthermore, a distorted profile. I finally used the ccf-method. From the cross correlation, I obtained only very small RV-variation for the UVES spectra. On the other hand, the HARPS spectra show a variation of several km/s. As shown in Figure 6.9 (b), I cannot verify the RV-variations found in the previous TWIN measurements. Blue points are the TWIN data, red points the two HARPS measurements, and green points the four UVES data. from these data, I derived an upper limit of 6.4 km/s. This result excludes a massive stellar companion. The light curve shows intensity variations in the order of 1 %. This activity of the star might cause the observed distorted LSD-profiles.

6.10   LRc07_E2_0108

The analysis of the light curve shows a transit with a flat bottom that corresponds to an 2.2-R_{Jup} companion. The increasing light after the transit and a tentative detection of a secondary transit indicates a bright and massive companion in an eccentric orbit. On the other hand, the transit depth is similar in all bands of CoRoT. Furthermore, a secondary transit is not an exclusion criterion in this survey, since massive planets of A-type stars are highly irradiated that might show a measurable secondary transit. The indications for a massive object are confirmed from the spectra obtained with the SANDIFORD spectrograph. Within seven days the radial velocity changes linear by 14 km/s. Thus, the RV-measurements show that the star is a binary. To obtain a better phase-coverage of the orbit, I took TWIN spectra. By adding the TWIN measurements 60 % of the period of 14.45 d is covered.
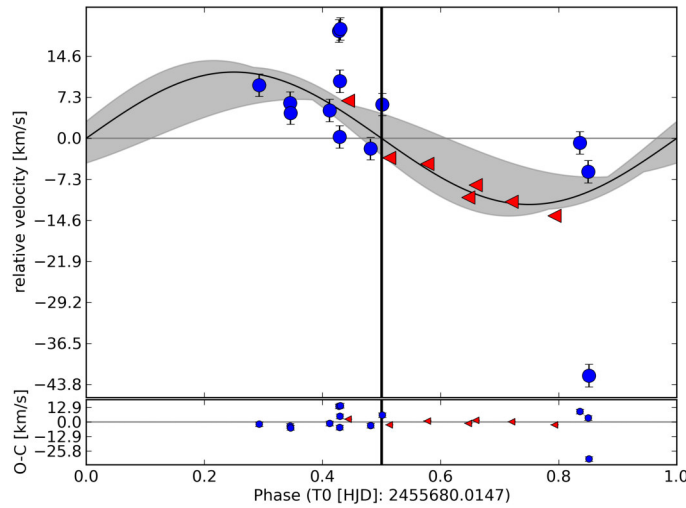
Figure 6.10: LRc07_E2_0108: Orbital fit to the RV-measurements.

parameter	value	error
ephemeris [HJD]	2455680.0147	$+0.25 - 0.79$
v_{r0} [km/s]	-23.26	± 4.9
K [km/s]	11.779	± 3.46
e	1e-11	(fixed)
period [days]	14.451	(fixed)

Table 6.6: LRc07_E2_0108: Parameters of the fit.

Figure 6.10 shows both datasets. Red points are the SANDIFORD data and blue points the TWIN data. It is possible to fit a circular orbit to the data. The scattering of the TWIN measurements is stronger since the accuracy of the TWIN spectrograph is smaller than that of the SANDIFORD spectrograph. One measurement at phase 0.85 deviates from the others by more than 30 km/s. An eccentric orbit fits to this data. This would confirm the increased intensity of the light curve as periastron brightening. Since this eccentric solution only depends on one measurement it has a low significance. Using all data, a circular orbit fits best. Thus, a mass of the secondary component of $m \sin i = 0.22 \, M_\odot$ can be derived. The parameters of the fit are given in Table 6.6.

Using the mass-radius relationship for low-mass stars (R $\sim$ M) and the stellar radius derived from the eclipse-depth, the companion mass would be $0.22\,M_\odot$. This is consistent to the mass obtained from the RV-measurements for an circular orbit. This confirms the assumption of an almost circular orbit and thus, the calculated mass has to be close to the true mass.

6.11 LRc07_E2_0307

This object shows a transit that is consistent with a planet with $1.3\,R_{Jup}$. I obtained three SANDIFORD spectra that show small RV-variations that would lead to an companion with $m \sin\ i = 17\,M_{Jup}$. Therefore, the star was followed-up with HARPS, UVES, and FIES. The FIES observations from summer 2013 covered almost a full transit and were taken from Davide Gandolfi. He noticed a possible RM effect during the transit. Together with the UVES spectra that cover another transit, I can confirm the existence of a red shift during the transit. The detected RM effect is shown in Figure 6.11 (a). The transit-duration is about $5.03\,$h, therefore it ends at phase 0.518. The RV-values after this phase are blue shifted by almost $350\,$m/s. This is in the same order than the maximum shift of $300\,$m/s (see equation. 7), that is expected from the RM effect. Since the star is a fast rotator ($v \sin\ i_\star$ is about $33\,$km/s) the accuracy of the RV-measurements are relatively low. UVES spectra can be measured with an accuracy of $0.19\,$km/s and FIES spectra with $0.35\,$km/s. The presence of

(a) (b)
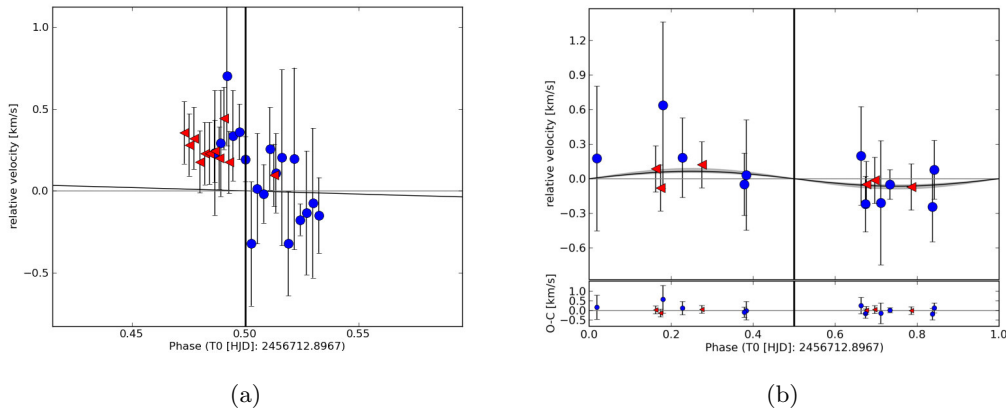
Figure 6.11: RV-measurements of LRc07_E2_0307;(a) possible RM effect during the transit, red: UVES and blue FIES-data, (b) tentative detection of RV-variations that corresponds to a $m \sin\ i = 0.7\,M_{Jup}$ companion. blue: FIES and red: HARPS data.

the Rositter effect and the fact that it is measured for two different transits confirms the presence of a transiting object. The mass can be obtained using further RV-measurements. The other FIES and HARPS spectra are taken out of transit and cover the orbit very well. Since they were obtained in different runs and with different set-ups, different instrumental offsets have to be applied to match the data.

I inspected the line-profiles and obtained changes in the core for each spectrum. The variations of the line profile are different for different spectral lines. Since pulsations can not be found in the CoRoT light curve, these variations might be explained by stellar activity. This results together with the rotational broadening in larger error bars. As shown in Figure 6.11 (b), the best fit gives a tentative solution with an amplitude of $65\,$m/s, corresponding to a $m \sin\ i$ of $0.72^{+0.27}_{-0.13}\,M_{Jup}$ using a Host-star mass of $1.43\,M_\odot$. The orbit parameters are

parameter	value	error
ephemeris [HJD]	2456712.896701	(fixed)
v_{r0} [km/s]	9.481	±0.016
K [km/s]	0.065	±0.018
e	0.0	(fixed)
period [days]	5.616598	(fixed)

Table 6.7: LRc07_E2_0307: Parameters of the fit. Offset between the HARPS and FIES data: -0.58 km/s.

summarised in In Table 6.7. This orbital fit is not highly significant. Therefore, from the maximal possible semi-amplitude of 0.25 km/s an upper mass limit of $m \sin i = 3.0 \, M_{Jup}$ can be derived from the data.

6.12 LRc07_E2_0482

With a spectral type of $F7$ V this is the latest star in this survey. It shows a small transit that would be consistent with $1 \, R_{Jup}$ companion. Two data points obtained with the SANDIFORD
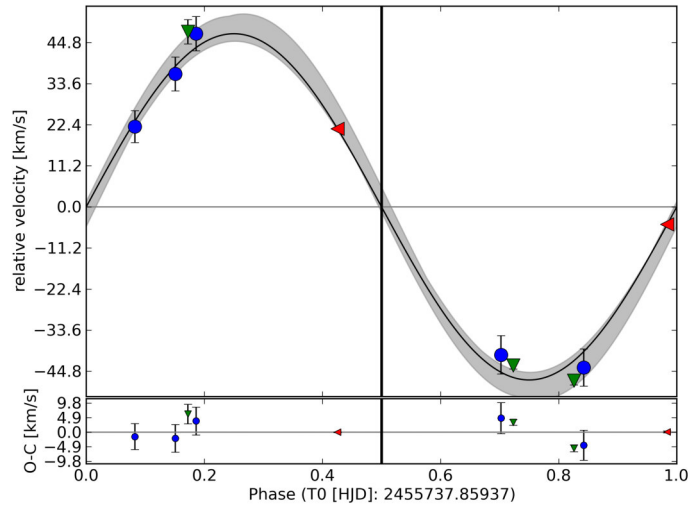
Figure 6.12: LRc07_E2_0482: Orbital fit to the RV-measurements. blue: TWIN, red: SANDIFORD, and green: IDS data.

spectrograph showed already a difference of 26 km/s. A stellar nature of the companion is therefore the only explanation. A more precise analysis of the light curve revealed a secondary eclipse as well as a v-shaped transit. The companion is grazing which explains the shallow transit-depth. Nevertheless, spectra were also obtained with the IDS and TWIN spectrographs. As shown in Figure 6.12, the RV-data can be fitted with a circular orbit to calculate the semi-amplitude. The parameters of this fit are given in Table 6.8. From the fit, I calculated the mass of the secondary component of $m \sin i = 0.483^{+0.065}_{-0.024} \, M_\odot$.

A literature search revealed that this star is also known as UNSW-TR-3 and was reported to be a binary by Hidas et al. (2005). They calculated a mass of 0.4 $pm 0.1 \, M_\odot$ which is fully in agreement with the mass, I obtained for this binary.

parameter	value	error
ephemeris [HJD]	2455737.85937	$+0.008 - 0.030$
v_{r0} [km/s]	27.44	± 3.54
K [km/s]	47.197	± 3.72
e	1e-11	(fixed)
period [days]	1.81739	(fixed)

Table 6.8: LRc07_E2_0482: Parameters of the fit.

6.13   LRc08_E2_4203

It is an early F-type star that shows a transit consistent to a $0.8\,R_{Jup}$ companion in a 3.3 d orbit. I obtained six spectra from the TWIN spectrograph and also analysed two spectra obtained by HARPS from the ESO-archive.

By considering the relatively low accuracy of the TWIN measurements, and the photometric ephemeris of HJD = 2455750.209082, both datasets supports RV-variations that matches a circular orbit. Thus, the mass of the companion can be derived with $m\sin\ i = 47\,M_{Jup}$. Figure 6.13 (a) shows the fit. Blue points are the HARPS and red points the Twin data. These measurements confirm that the companion is a brown dwarf.

Motivated by this result further observations were obtained with UVES. Interestingly, the UVES measurements do not confirm the RV-variations found from TWIN and HARPS measurements (see Figure 6.13 (b)). The maximum possible RV-variation is 5.6 km/s. This leads to an upper limit for the companion of $m\sin\ i = 66\,M_{Jup}$.

(a)   (b)
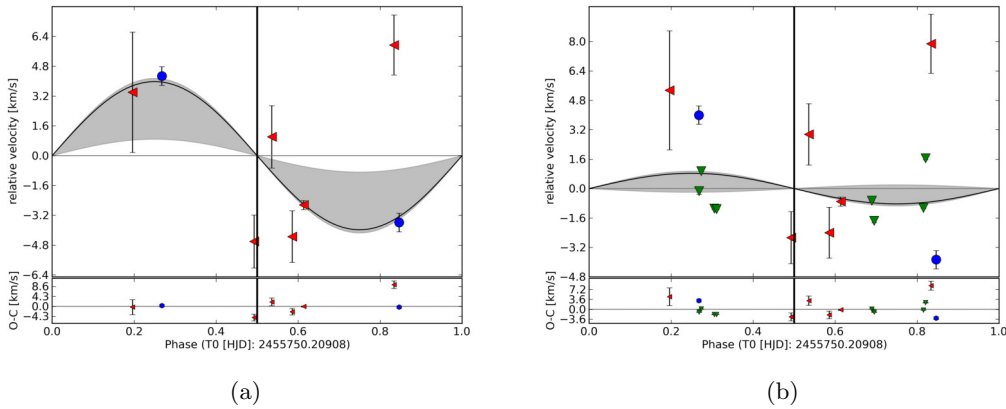
Figure 6.13: orbital fit of LRc08_E2_4203; (a) Tentative detection of an RV-signal consistent with a brown dwarf; blue HARPS data, red TWIN data, (b) Same data, but with UVES-measurements (green) added. The signal of the brown dwarf cannot be confirmed.

6.14   LRc10_E2_3265

A detailed analysis of the CoRoT light curve shows a transit signal that corresponds to a $0.5\,R_{Jup}$ companion in a 4.8 d orbit. Since, the photometric spectral type of the object is $A5$ V, I observed the candidate as backup-target on my observations with the TWIN spectrograph. The orbital fit to the RV-measurements does not show a significant result for the RV-variations. The upper limit derived for the semi-amplitude of the companion is 3.83 km/s. I derived the spectral-type of the star from the mean spectrum obtained by

combining all six TWIN spectra. Since it is an $F6$ V star with M $= 1.35\,M_\odot$, the upper mass-limit for the companion is $m \sin\ i = 41\,M_{Jup}$.

6.15   IRa01_E2_2721

This star was one of the most challenging targets in order to find the radial velocity variation. With a $v \sin\ i_\star$ of about $236\,\mathrm{km/s}$ it rotates extremely fast. This limits the reachable RV-accuracy to 1-3 km/s. SANDIFORD spectra from the star show RV-variations of about $147\,\mathrm{km/s}$, indicating a binary nature of the object. Since the S/N is very low and the orbit is not covered by the SANDIFORD spectra completely, the object was observed with CAFE (CAFEI). By using the same wavelength-area as observed with SANDIFORD, I obtained comparable RV-variations. The orbital fit to all measurements is consistent to a binary with $m \sin\ i = 1.2\,M_\odot$ (see Figure 6.14 (a)). This binary is extremely interesting because of its short period of only 0.6 days. It might be a progenitor of low-mass white dwarf with a helium core (He-WD). Furthermore, the ephemeris calculated from the orbital fit are phase shifted to the expected variations for the light curve by a phase of 0.5. This result implies that the main object in the system has to be an invisible companion like a white dwarf. Nevertheless, this interpretation is inconsistent to the expected size of $1.5\,R_{Jup}$. To solve this case the star was observed again with CAFE (CAFEII) and UVES. UVES spectra offer the first time high S/N data and, thus, the possibility to analyse the star with a sufficient accuracy. The analysis of the UVES spectra shows a velocity difference of about $20\,\mathrm{km/s}$ between the H_α and the H_β lines. Since I used a synthetic template spectrum of a fast rotating $A5$-star to derive the RVs, this unusual spectrum causes the observed RV-variations. The only possibility to analyse the
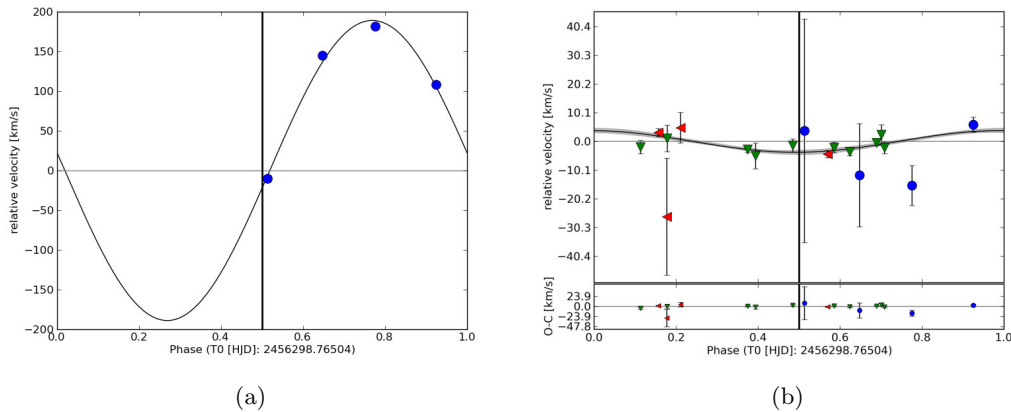
Figure 6.14: Orbital fit of IRa01_E2_2721; (a) CAFE measurements indicate a binary with an invisible component; (b) All CAFE and UVES data, analysed by using a co-added UVES spectrum as template.

RV-variations relative to the separate spectra is to use the stellar spectrum itself as template. I normalised one UVES spectrum, binned it, and re-sampled it to a high-resolution spectrum with high S/N. This method introduces an offset to the absolute RV-values. Since it is a constant offset, It is easily be removed afterwards. I used this method to analyse the new CAFE spectra (CAFE II) and to re-analyse the old CAFE spectra (CAFE I). I used the wavelength range between $4778\,\text{Å}$ and $6800\,\text{Å}$, covered by the red arm of UVES. As shown in Figure 6.14 (b), the RV-velocity of the object in this wavelength region does not show

any variations. green are the UVES data, blue are the CAFE I data and red are the CAFE II data. The orbital fit does not converge to an significant result. The upper limit is an amplitude of 17 km/s which results in an upper mass-limit of $m \sin i = 0.12 \, M_\odot$. If only UVES data are used, this upper-limit is even smaller. These results exclude any high-mass binary in a 0.6 days orbit.

6.16 IRa01_E1_4591

The light curve of the candidate shows transits that match to a $1 \, R_{Jup}$ companion on a close-in orbit of only 0.07 AU in a period of 4.3 d. Furthermore the star shows pulsations with a period of 0.084 d and a mean amplitude of 0.12 mmag. This is exact a 51th part of one transit-period, which indicates that these pulsations are triggered by the companion. I obtained six CAFE spectra that show strong RV-variations. As shown in Figure 6.15 (a), a circular orbit fits to the RV-data with a semi amplitude of 16.31 ± 12.84 km/s. This result shows that it is a binary.   Nevertheless, this orbit does not explain why the star shows

(a)   (b)
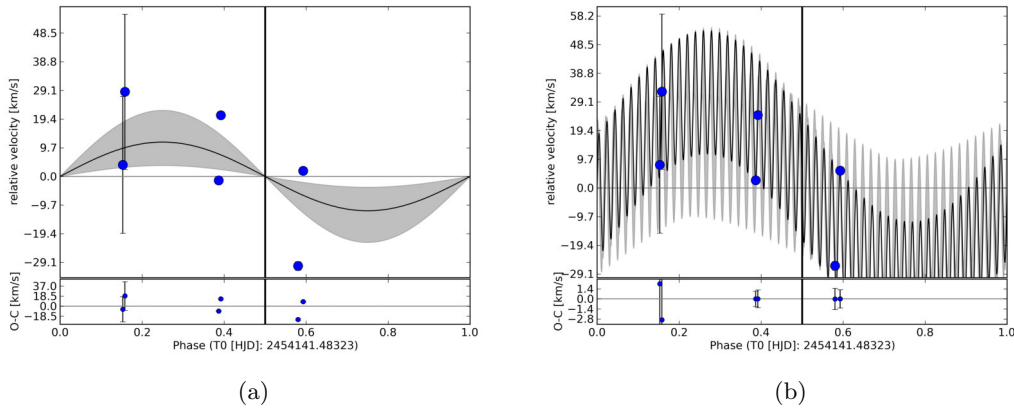
Figure 6.15: Orbital fit of IRa01_E1_4591; (a) CAFE measurements indicate a binary solution; (b) same CAFE data, but including the effect of pulsations, introduced to the RV-measurements.

parameter	value	error
ephemeris [HJD]	2454141.48323	±0.1
v_{r0} [km/s]	51.70	±1.75
K [km/s]	32.36	±11.03
e	0.0	(fixed)
period [days]	4.2945	(fixed)
pulsations		
K_p [km/s]	20.87	±3.56
period [days]	0.0842	(fixed)

Table 6.9: IRa01_E1_4591: Parameters of the fit

extreme RV-variations of 32.2 km/s in only 1.3 h. Probably the pulsations induce strong RV-variations of this star. To measure them, I assume an sinusoidal RV-variation with the period of the pulsation that is superimposed to the orbit of the binary. The new orbital fit is shown in Figure 6.15 (b), and reveals an extreme RV-variation with an semi-amplitude (K_p) of 21 km/s. The parameters of the fit are summarised in Table 6.9. The reduced χ^2 of this fit is only 0.02, compared to 107.56 for the first fit. this is an almost perfect match

within the error bars of the RV-measurements. The new semi-amplitude of the orbit is 32.4 ± 11 km/s. By using a primary mass of $2.04\,M_\odot$ the calculated mass of the secondary is $m\sin\ i\ =\ 0.45^{+0.01}_{-0.31}\,M_\odot$. Six spectra are the minimum number of data-points to solve the system. More data would put further constraints to the influence of the pulsation in IRa01_E1_4591. Due to the pulsations the eclipse-shape is distorted and might be v-shaped, which might explain the shallow eclipse-depth. Thus, I can explain the system by a grazing binary system with an $A5$ V primary component and a $M0$ V secondary component. Tidal interactions between both stars probably induce the pulsations on the primary component.

7 Discussion of the survey

In this section, I will discuss further some of the more interesting objects, extrapolate conclusions from the survey and compare these conclusions to results from literature.

7.1 Confirmed binaries

I found six cases for eclipsing binaries in the survey. Two of them were already known before and I used them to judge the accuracy of the RV-measurement. Table 7.1 gives an overview to the parameters of the systems. P is the orbital period, M_{comp} the mass determined for the secondary and q the mass ratio with $q = M_{comp}/M_{\star}$.

To find out whether the orbital periods and masses in this small sample are typical for binaries of IMSs, I compare them to average values from the literature. Carquillat & Prieur (2007) analysed 91 A_m stars and found a Gaussian mass-distribution for the companion masses centred on $0.8 \pm 0.5\,M_{\odot}$. The stellar companions in this survey are on average smaller than these findings, but are still consistent with their lower border. The calculated mass-ratios are distributed from 0.1 to 0.6 centred on a ratio of 0.3. This is again consistent with the lower borders from Carquillat & Prieur (2007). On the other hand, this is only half of the value derived by Vuissoz & Debernardi (2004), who found $q = 0.56$ from their statistical sample of 82 A_m stars. One explanation for this bias towards low-mass companions is my selection criteria, which favour stars with shallow, planet-like transits.

ID	P [d]	M_{comp} [$M_{\odot}$]	q
LRc02_E1_0132	3.69	1.253	0.56
LRa01_E2_1578	16.06	0.75	0.56
LRa02_E1_0725	9.09	$\gtrsim 0.19$	$\gtrsim 0.09$
LRc07_E2_0108	14.45	~ 0.22	$\gtrsim 0.12$
LRc07_E2_0482	1.82	0.48	0.37
IRa01_E1_4591	4.29	0.45	0.22

Table 7.1: Binaries of the survey

It is well known that close-in binaries show circular orbits, while binaries with long orbits have statistically higher eccentricities (e.g. Duquennoy & Mayor 1992). This transition allows to put observational constraints to the tidal circularisation in binary systems and is, thus, called tidal circularisation cut-off period. For pre main-sequence stars this cut-off period is roughly 7 to 8 d Melo et al. (2001) and increases with the age of the star (Mathieu et al. 2004). The cut-off period in the small sample of binaries in this survey is obviously between 4.3 and 9 days. This is in complete agreement with the observations of Carquillat & Prieur (2007). They found a very sharp border at P $= 5.6 \pm 0.5\,d$ for the cut-off period of A_m stars and, therefore, constrain the circularisation time with the age of these stars to $0.5 - 1 \cdot 10^9\,yr$.

Since I determined the radii of the companions of LRa02_E1_0725 (2.1 R_{Jup}) and LRc07_E2_0108 (2.2 R_{Jup}) from the eclipse-depth, their masses can be calculated from the mass-radius relation of main-sequence stars (see section 1.5.1). The comparison to the RV-results shows that the calculated masses are close to those obtained from RV-measurements. This comparison

cannot be done for the other binaries. LRc02_E1_0132 is not a main sequence star and for the other stars the stellar radii cannot be determined, since they show V-shaped transits.

7.1.1 Long periodic binaries

I found three objects that show long-term trends. These objects must be long periodic binaries. LRa01_E2_0203 as well as LRa01 E2 0963 were already discussed in the previous chapter. LRa01_E2_0203 shows 10 km/s variations over a period larger than 84 d and LRa01 E2 0963 shows a linear trend of about 6 km/s over a timespan of 120 days. The star LRa02_E2_4150 also shows a linear trend. Within two years its radial velocity changed by 14.5 km/s. Unlike the first two stars, this one shows additionally RV-variations that correspond to the transit period of 8.2 d. I will discuss this candidate in more detail in the section below.

7.2 Sub-stellar companions

One goal of this survey is to identify sub-stellar companions of IMSs. I found three candidates with firm evidence for a sub-stellar companion. I will discuss each one on more detail and also show the follow-up observations that were done so far to confirm them as real objects. Their updated physical parameters are given in Tab. 7.2.

parameter	unit	LRa02_E2_4150 b	LRc07_E2_0307 b	LRa02_E1_1475 b
a	[AU]	0.128±0.002	0.0695±0.0007	0.0404±0.0003
period	[days]	8.1703±0.0003	5.61660±0.00005	2.1183±0.0003
i	[°]	85.7±0.3	84.95±0.07	71.5±0.4
R_P	[R_{Jup}]	1.8±0.2	1.8±0.1	1.6±0.1
M_P	[M_{Jup}]	$63.6^{+1.6}_{-2.2}$	$< 3.01^{\star}$	$81.5^{+4.8}_{-4.3}$
density	[g/cm^3]	14.4±4.5	> 0.6	27.9±6.6

Table 7.2: Physical parameters of LRa02_E2_4150 b, LRc07_E2_0307 b, and LRa02_E1_1475 b. (* This mass is an upper limit).

LRa02_E2_4150

This star is also designated as HD 295605. A careful determination of its stellar parameters was done by Christian Heuser. He analysed the high resolution spectra and obtained T_{eff}= 15 800 K, log(g)=4.40, and a metallicity that is 1 dex above the solar value. These values are consistent with the previous results of a B4 V star with a mass of 4.2±0.2 $M_{\odot}$ and a radius of 2.3±0.1 $R_{\odot}$ (Georgy et al. 2013). From the light curve, I derived a radius of the companion of 1.8 R_{Jup} and a mass from RV-measurements of $63.6^{+1.6}_{-2.2} M_{Jup}$. This could be, therefore, the first transiting, close-in brown dwarf orbiting an early B-type star. This object is placed directly at the border from high-mass sub-stellar objects and very low-mass stars. I analysed the CoRoT light curves in the three different bands. The light curve shows periodic intensity variations with an amplitude of 0.0124 mag (see Figure 7.1 (a)). These are caused by pulsations and can analytically be described by a superposition of sinus functions. The frequencies are shown in Table 7.3 and were obtained using the program "period04" (Lenz & Breger 2004). The amplitudes are relative to the mean intensity of 2767638.45733403 electrons/sec. F2 and F3 are alias of the main frequency F1. Those are

pulsations that are similar to the pulsations found for γ Dor stars.

I phase folded the light curve with the period of 8.1703 d to check the transit depth. Figure 7.1 (b) shows the transit of the object with a total duration of 3.41 h. The colours represent the three-colour light curves from the CoRoT satellite. The transit depth is about 0.65 % in red and green. With 0.7 %, it is slightly deeper in blue, which can be an effect of the lower S/N compared to the other colours or due to a residual of the pulsation. For example, the linear increase of intensity, which is visible within the transit disappears if the pulsations are removed from the light curve. It is thus a residuum of the pulsations.

(a)

(b)
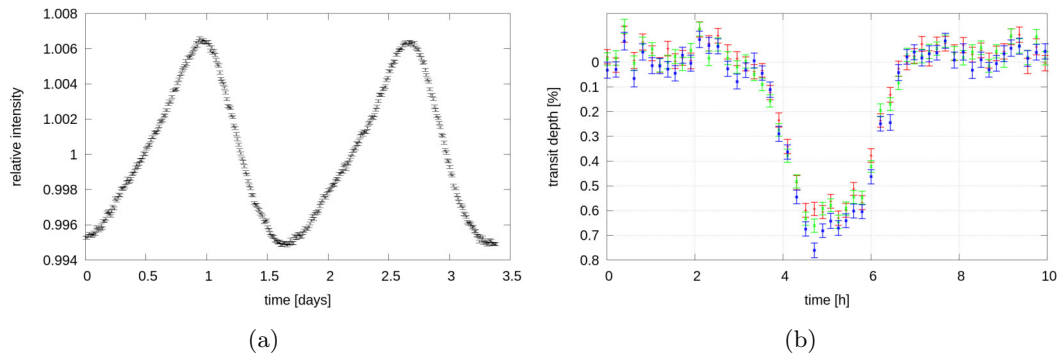
Figure 7.1: Light curve of *LRa*02_*E*2_4150. (a) binned and phase folded to the main pulsation frequency, (b) binned and phase folded to the orbital frequency. The colours represent the three chromatic channels of CoRoT.

#	frequency [c/d]	amplitude	phase
F1	0.589	14707.62	0.023
F2	1.178	3260.23	0.032
F3	1.769	809.13	0.026
F4	0.014	6373.63	0.984
F5	0.008	5508.18	0.145

Table 7.3: Detected frequencies of the pulsation of LRa02_E2_4150.

To calculate the size of the companion, it is important to verify that no close-by star contaminates the light curve. Using the EXODAT database it is possible to reconstruct the position of the mask in the sky. This reveals a 15.5 mag star, which contaminates the blue channel. Since the blue channel also shows a lower S/N compared to the other colours, I only used the green and red channels of the light curve to calculate the size of the companion.

In the acquisition images from the first FIES observations in December 2012 the star appeared slightly elongated. This elongation was probably due to a slightly defocussed image of the acquisition camera. Nevertheless, there is a possibility of a close visual companion of the star at 2" distance and only 1 mag fainter than the main star itself. Therefore, I analysed high resolution images of this star to confirm or to exclude this possible visual companion. First, I analysed an image obtained with the CFHT wide-field imager. Since the star is saturated in this image it is not possible to exclude a second star.

Two important entries are found in the literature that strengthen the existence of a second source. First, the star is reported as a visual binary in the Tycho Double Star Catalogue (Fabricius et al. 2002). Second, Magakian (2003) found this star to be associated with a

reflection nebula. In this case, the second source might origin from a temporal brightening of the nebula. Both scenarios might explain the elongated image in the acquisition camera. To solve this an observation campaign was started to monitor the star. Pilar Montañés kindly provided service observations with the CAMELOT imager at the IAC80 Telescope at the Instituto de Astrofísica de Canarias' Teide Observatory (Tenerife, Canary Islands,Spain). The star was monitored several times per week in service mode in the time from 05-03 to 12-04-15, using the bands V, R, I, and H_α. The mean seeing for the monitoring was 1". Nevertheless, the bright companion was not detected in all images and bands. To calculate the significance of this result, I co-added all images of the star and subtracted the Point spread function (PSF) of the imager. The PSF was obtained from the image of the star itself. I rotated the image centred to the coordinates of the star in steps of 22.5°and calculated the median of all rotated images. This method removes all humps in the PSF that might be caused by a close-by light source. After subtraction of the PSF, I can conclude that there is no light source with a brightness difference less than 7 mag at a distance ≥ 0.8". I also exclude any bright H_α emission in the vicinity of the star.

Another consistency check aims in excluding any possible double lined binary by analysing the line-profile. Therefore, I analysed all FIES spectra using the CCF method. The bisectors of these profiles are variable, which indicates time-dependent changes in the line profile. These can be caused by pulsations of the star or simply by the limited accuracy of the measurement due to the rapid rotation of the star. To analyse the time-dependence, I first phase-folded these variations to the transit period and second to the period of the main pulsation. The changes of the profile are not in phase with both periods. Thus, the measured RV-variations are not caused by these profile variations, but rather by the presence of a real companion. On the other hand, these changes in the line profiles explain the relatively large error bars of some of the RV-measurements. Furthermore, a visual inspection of the CCF-profiles in all phases of the orbit does not show any obvious binarity or asymmetry. Therefore, I can exclude a double-lined binary.

I analysed the last five FIES spectra in the same way as the previous spectra. They were obtained in consecutive nights by Davide Gandolfi in January 2015. The spectra confirm the current velocity change of about -3 km/yr and, therefore, the presence of a stellar companion with P > 3yr. Nevertheless, after applying this offset the RV-measurements do not fit to the orbital fit (shown in section 6.5). These new measurements, therefore, do not confirm the mass of the companion. Since LRa02_E2_4150 is a very interesting candidate, further RV-observations are planned and will shed more light in the nature of the object. The FIES spectra furthermore show strong differences in the bisector compared to the older spectra. If these differences would be caused by the long periodic stellar companion, this result shows that the secondary is bright enough to affect the measurements.

LRc07_E2_0307

The star was discovered by analysing the light curves of the field LRc07 together with Sascha Grziwa. Therefore, this transit was first found in this survey and was not previously known by the CoRoT detection teams. Afterwards, intensive follow-up observations of the object

from the CoRoT team were performed. A spectral classification of high-resolution spectra gives $T_{eff} = 6430 \pm 70$ K, $\log(g)=4.40$, which is consistent with the spectral type $F6$ V that I found in this work. Using evolutionary tracks (Girardi et al. 2000) Eike Guenther derived the stellar parameters: M $= 1.43 \pm 0.04\, M_\odot$ and R $= 1.93 \pm 0.01\, R_\odot$. The Transit of this object (which is shown in Figure 4.1) leads to a large object of $1.8\, R_{Jup}$. From the best orbital fit I derived a mass of $0.72^{+0.27}_{-0.13}\, M_{Jup}$. With this mass it would be a very low density planet with only $0.16\, g/cm^3$. Nevertheless, due to the low number of only 17 spectra and the relative large errors, the significance of this solution is not high enough to confirm this solution. Therefore, I determined the upper limit for the companion mass of $3\, M_{Jup}$. The upper mass limit would result in a mean density of $0.68\, g/cm^3$. This is consistent to the average density of giant planets (Hatzes & Rauer 2015).

Since the star is located in the centre field the false alarm rate is relatively high. Seeing limited on-off observations (see section 1.3.3) were done with the IAC 80 telescope and the WISE-1-m-telescope. These observations prove that the transit comes from the star itself and is not caused by any other eclipsing star in the field. The data obtained with the WISE-1 telescope have a quality that is even high enough to analyse the transit parameters. From these observations the ephemeris of the transit is significantly improved and can be used for further follow-up of the transit. Imaging with the AO system PISCES at the LBT (Large Binocular Telescope) reveals two previously unknown stars close to the candidate itself. Both of these stars are too faint to be a source of the transit. From these observations we know with a very high probability that the transit is caused by an object orbiting LRc07_E2_0307 itself.

(a)   (b)
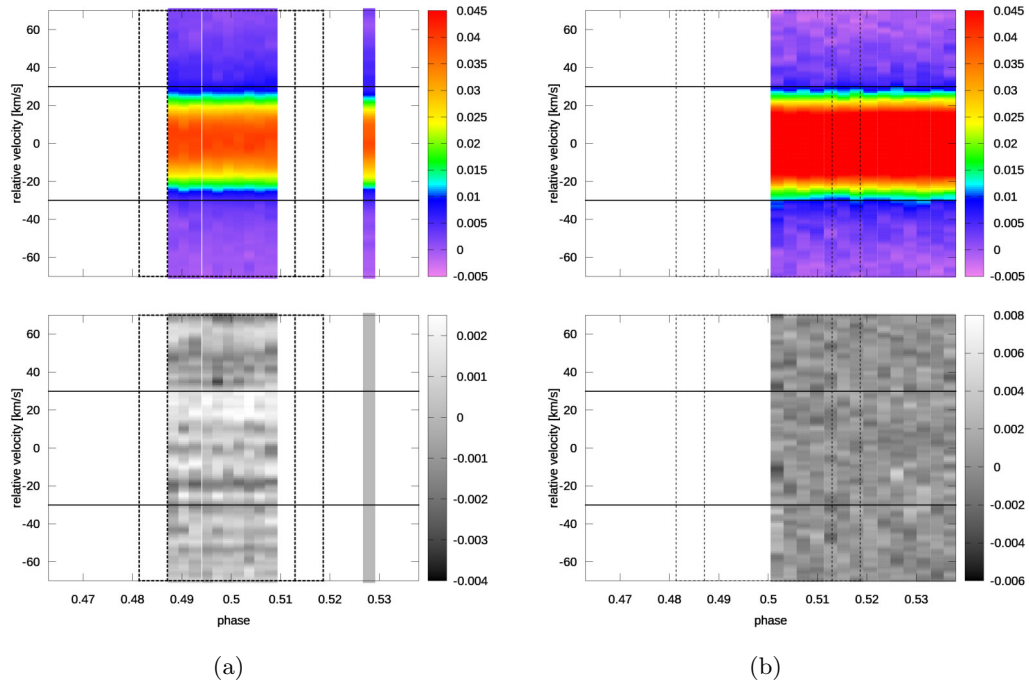
Figure 7.2: Line-profile tomography of LRc07_E2_0307. Uppel panel: line-profile. lower panel: residuals after removing the mean line profile (a) UVES spectra, (b) FIES spectra. Note: The residuals are calculated from inverted line-profiles. Negative dips represent positive humps in the actual line-profile.

Using the UVES and FIES spectra, as well as the improved ephemeris, I confirmed the RM effect as a red-shift during the transit. Since the size of the planet is relatively large and the star rotates with $v \sin i_\star = 33 \, km/s$, I would expect a hump in the blue part of the line-profile (negative part in the velocity space). This planet might be resolved by line-profile tomography. I, therefore, analysed the line profiles of the UVES and FIES spectra that were obtained during the transit. Figure 7.2 shows the line profiles as well as the residuals after subtracting the mean line-profile. The solid black lines indicate the velocity $30 \, km/s$ and are drawn to guide the eye, while the dashed black lines mark the ingress and egress of the transit calculated from the improved ephemeris ($T_0 = 2456864.459$ HJD). From the UVES spectra I used the line-profile of the spectrum that was observed directly after the transit to remove the line-profile and calculate the residuals (Figure 7.2 (a), lower panel). These show a hump at -20 km/s. This is exactly the expected behaviour to confirm the planet signal. The hump does not change its position during the transit-duration. This is consistent with the measured constant red shift, measured from the spectra directly and indicates an almost polar (obliquity $\sim 90°$) orbit. The observation of this hump provides (apart from the transit itself) an independent confirmation of the presence of the object. Together with the upper mass limit, I can conclude that the companion of LRc07_E2_0307 is a transiting planet in an almost polar orbit at $0.07 \, AU$ distance around its $F6$ V host star.

On the other hand, a second spectrum out of the transit was obtained with UVES one year later. This spectrum has a higher S/N than the first out-of-transit spectrum. If I use this spectrum to remove the profile from all spectra the hump is not visible anymore and the first out-of-transit spectrum shows a negative dip at -20 km/s. Two possible scenarios would describe this situation: First, the star is active in RV and shows small scale line profile variations. This might just by chance result in a hump in the second out-of-transit spectrum that is similar to the planet signal. Second, the dip in the first out-of-transit spectrum is a real line-profile variation due to activity. In this case the observed hump during the transit would be an artefact. The second scenario would alternatively explain the measured RV-drift as well as the fact that the position of the hump does not change during the transit. More UVES spectra taken out of the transit would shed light in this discussion. The S/N of line-profiles obtained from the FIES spectra (Figure 7.2 (b), lower panel) is too low to show any signal of a hump.

Nevertheless, it is definitively a very promising candidate and deserves further follow-up observations.

LRa02_E1_1475

This target was already in the CoRoT target list as I started this survey. Therefore it was followed-up by the CoRoT group with several instruments. Observations with the CFHT from 2010 revealed that the transit is on-target. This means that none of the close-by stars are the source of the transit measured by CoRoT. Guenther et al. (2013) observed the star with CRIRES to search in the infrared for lines of a late-type companion star. He cross-correlated the spectrum with that of the M3 V star HIP4569 and did not found any match for a late-type star. This excludes any companion earlier than spectral type $F6$ V within the accuracy of this method. The mentioned pulsations with a period of $0.7 \, d$ were already detected by Sarro

et al. (2013). They also calculated stellar parameters from GIRAFFE spectra and found: $T_{eff1} = 8396\,K$, $T_{eff2} = 7909\,K$ and log(g)=3.8. The two values for the temperature result from the fit to two different data-sets of synthetic and observed templates. Christian Heuser also calculated the stellar parameters, based on high resolution UVES spectra. He determined $T_{eff} = 7900\,K$, log(g)=3.8, and a low metallicity by fitting a third grid of synthetic spectra. The log(g) is consistent for all datasets. I used the average effective temperature from all datasets and derived T_{eff} to $8068 \pm 163\,K$. The error is derived as the standard deviation of the three independent datasets. These values are consistent with an $A7\,IV$ star. This indicates
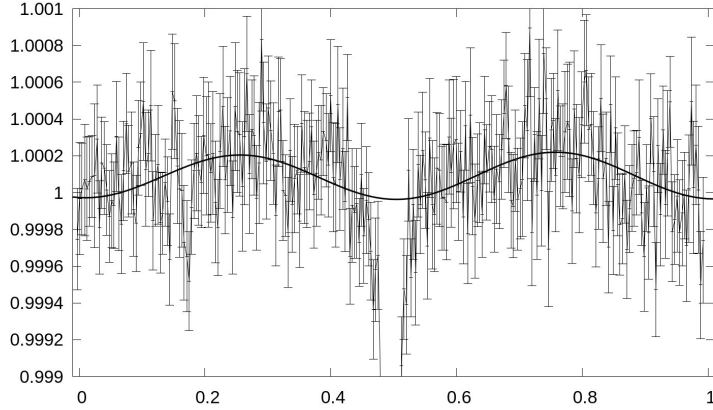
Figure 7.3: Light curve of LRa02_E1_1475. Ellipsoidal variations are obviously visible, black line: fit to the variations.

from the log(g) that the star is already slightly evolved. By comparing the parameters with stellar evolution models (Georgy et al. 2013) and using a low metallicity, I obtained M = $1.98 \pm 0.05\,M_\odot$ and R=$2.93 \pm 0.03\,R_\odot$. This is almost twice the radius that is expected from a main-sequence star. For the companion this results in a size of $1.6 \pm 0.1\,R_{Jup}$. From the light curve an inclination of $71.5°$ can be derived. Together with $m \sin i$ from RV-measurements the mass of the companion is $81.5^{+4.8}_{-4.3}\,M_{Jup}$.

Given the semi-major axis of $0.04\,AU$, this brown dwarf is with only $3\,R_\star$ extremely close to its host star. This is even more extreme than CoRoT-7b that exhibit a distance of $4\,R_\star$. Therefore, I expect tidal effects of the light curve. The pulsations of the star are variable in intensity (with an amplitude of up to $1\,\%$) and are consistent to one third of the orbital period of $1.12\,d$. Due to this period, the intensity variations are almost completely cancelled if the light curve is phase folded to the orbital period. It is, thus, possible to analyse the phase-folded light curve for tidal effects using the BEER approach (Mazeh et al. 2012). I did the analysis with the red channel of CoRoT which exhibit the lowest amount of distortions. The result is displayed in Figure 7.3. I measured the amplitude of ellipsoidal variations with $122 \pm 23\,ppm$. The effect of reflected light ($1.6 \pm 9.8\,ppm$) and Doppler beaming ($8.5 \pm 23\,ppm$) are spurious and consistent with zero detections. To calculate the mass from this method, I used the equation (7) in (Mazeh et al. 2012) and due to the similar spectral type of the host star I adopted the numerical factor α_{ellip}=1. This factor describes the response of the stellar surface to the tidal effects that are induced by the companion (Faigler & Mazeh 2011). The mass of the companion from the ellipsoidal variations is $6.8\,M_{Jup}$. This mass is an important confirmation of the sub-stellar nature of the companion. On the other hand, the mass obtained by this method is one order of magnitude smaller than the mass obtained

from the RV-measurements. This discrepancy might be solved by a further analysis of the light curve to obtain a more accurate value of α_{ellip}. Since the star is an extreme fast rotator ($v \sin i_\star \sim 160 \, km/s$), time resolved spectroscopy during the transit would resolve the brown dwarf. The high-resolution spectra of this star do not cover the phases of the transit. Nevertheless, such measurements would first additionally confirm the brown dwarf and, second clarify its obliquity to the stellar spin axis.

7.3 Unsolved cases and false alarms

Finally, I analysed the two objects, LRc03_E2_2657 and LRc08_E2_4203 that show planet-like transits. RV-measurements from spectra obtained with UVES do not fit to an orbit of the transit period. Therefore, these measurements disproved previous brown dwarf solutions, indicating that the companion masses are much lower than derived from those solutions. The upper mass-limits derived from the RV-measurements show that none of both candidates is a binary. Both are faint and fast rotators. Thus, further follow-up observation like time-resolved spectroscopy would be interesting to solve these cases.

ID	upper limit $[M_{Jup}]$	comments
LRc03_E2_2657	< 80	no RV-variations with UVES
LRc08_E2_4203	< 66	no RV-variations with UVES
LRc10_E2_3265	< 52	prob. BEB with periastron brightening
IRa01_E2_2721	< 126	No EB, pulsating star
LRa02_E2_1023	< 42	prob. BEB

Table 7.4: unsolved candidates: The first two candidates are still candidates for sub-stellar companions, the other three are most probably false alarms.

For three other targets my investigation revealed that they are most probably false alarms: For LRc10_E2_3265, I got only an upper limit excluding a massive companion, but the light curve of the object shows a strong periastron brightening after the transit. This result is consistent with a Background eclipsing binary (BEB). IRa01_E2_2721 is a very interesting and pulsating star with strong RV-shifts for different lines. Finally, after obtaining UVES spectra with high S/N, any high-mass sub-stellar companion can be ruled out. Furthermore, LRa02_E2_1023 shows line profile variations that are consistent with a contaminating object in the background. For all of these objects, I obtained upper limits for the masses. Those are summarised in Table 7.4.

7.3.1 Mass-density relation of brown dwarfs

The brown dwarfs found in this survey are at the border of very high-mass brown dwarfs and low-mass stars. Since Hatzes & Rauer (2015) found a maximum density of companions at $M_{comp} = 63 \pm 6 \, M_{Jup}$, LRa02_E2_4150 b might serve as a benchmark object to analyse this transition between brown dwarfs and stars. Fig. 7.4 shows the mass-density diagram. The positions of the brown dwarfs found in this survey are marked.

Spiegel et al. (2011) calculated that brown dwarfs will reach almost the same radius of $\lesssim 1 \, R_{Jup}$ when they cool down and contract. This is also found empirically from the observations of transiting brown dwarfs of solar-type and low-mass stars (Csizmadia 2016). Both objects
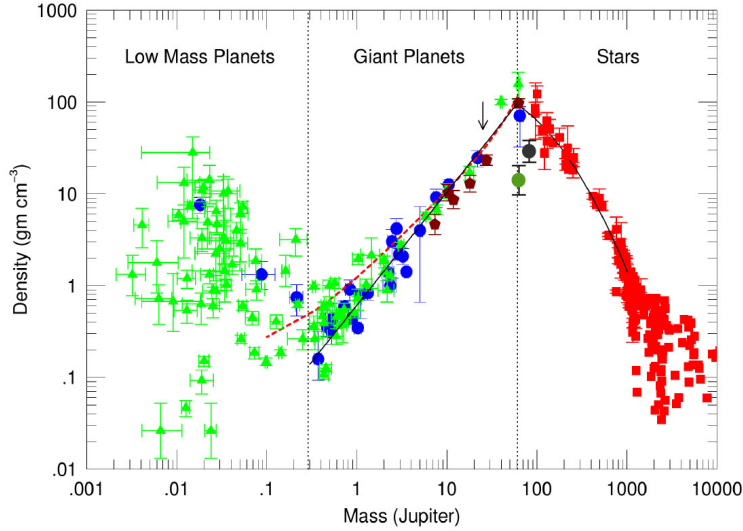
Figure 7.4: Mass-density diagram for transiting objects (diagram from Hatzes & Rauer (2015), Figure 1). The positions of LRa02_E2_4150 b, and LRa02_E1_1475 b are marked by dark-gray and green filled circles, respectively.

exhibit much larger radii than observed for brown dwarfs of solar-type stars. Although, the mass of them and those observed by late-type stars are similar, the difference is the age. LRa02_E2_4150 b is the first brown dwarf orbiting a *B*-type star. The age of this star has to be less than 20 Myr (Georgy et al. 2013). The host star of LRa02_E1_1475 b is slightly evolved. This means that the companion will be engulfed by the star within the next two Myr. Nevertheless, it is still an *A*-type star with an age that has to be ~ 0.9 Gyr.

Stassun et al. (2006) found a young (< 1 Myr) system of two eclipsing brown dwarfs that show radii of 7.0 and 5.3 R_{Jup} with masses of 56.6 and 35.6 M_{Jup}, respectively. This discovery shows, that young brown dwarfs are much larger than old 1-Gyr objects. Thus, the large radii of both brown dwarfs can be explained by their youth. By comparing those radii, one can draw the preliminary conclusion that massive brown dwarfs shrink by $\sim 70\%$ within the first 20 Myr, but only by $\sim 10\%$ between 20 and 900 Myr. This is compatible to the model calculations of Spiegel et al. (2011), who showed that massive and young (< 10 Myr) brown dwarfs have radii with more than $2 R_{Jup}$.

7.4 Frequency of planets of intermediate mass stars

The main goal of this survey is to derive the frequency of close-in planets for different stellar masses. As explained in section: 2 the CoRoT survey is perfectly suited to do such a survey.

7.4.1 The absolute frequency of planets in the CoRoT survey

If I include the three sub-stellar objects found in this work the harvest of the CoRoT-survey yielded 35 sub-stellar objects.

ID	$M_\star$ [$M_\odot$]	SpT	Period [d]	R_{comp} [R_{Jup}]	M_{comp} [M_{Jup}]	Distance [AU]	reference
CoRoT-33 b	0.86±0.04	*G9* V	5.8	1.10 ±0.53	59 ±1.8	0.058	Csizmadia et al. (2015)
CoRoT-8 b	0.88±0.04	*K1* V	6.2	0.57 ±0.02	0.22 ±0.03	0.063	Bordé et al. (2010)
CoRoT-10 b	0.89±0.05	*K1* V	13.2	0.97 ±0.07	2.75 ±0.16	0.011	Bonomo et al. (2010)
CoRoT-24 b	0.91±0.08	*K1* V	5.1	0.33 ±0.04	0.018	0.056	Alonso et al. (2014)
CoRoT-24 c	0.91±0.08	*K1* V	11.7	0.44 ±0.04	0.088±0.035	0.098	Alonso et al. (2014)
CoRoT-7 b	0.92±0.02	*K0* V	0.8	0.16 ±0.01	0.018±0.003	0.017	Barros et al. (2014)
CoRoT-7 c	0.92±0.02	*K0* V	3.7		0.042±0.003	0.045	Haywood et al. (2014)
CoRoT-1 b	0.95±0.15	*G0* V	1.5	1.49 ±0.08	1.03 ±0.12	0.025	Barge et al. (2008)
CoRoT-18 b	0.95±0.15	*G9* V	1.9	1.31 ±0.18	3.47 ±0.38	0.029	Hébrard et al. (2011)
CoRoT-2 b	0.97±0.06	*G7* V	1.7	1.47 ±0.03	3.31 ±0.16	0.028	Alonso et al. (2008)
CoRoT-29 b	0.97±0.14	*K0* V	2.9	0.9 ±0.16	0.85 ±0.2	0.039	Cabrera et al. (2015)
CoRoT-9 b	0.99±0.04	*G3* V	95.3	0.94 ±0.04	0.84 ±0.07	0.407	Deeg et al. (2010)
CoRoT-5 b	1.00±0.02	*F9* V	4.0	1.39 ±0.05	0.47 ±0.05	0.049	Rauer et al. (2009)
CoRoT-28 b	1.01±0.14	*G8/G9* IV	5.2	0.96 ±0.07	0.484±0.087	0.059	Cabrera et al. (2015)
CoRoT-17 b	1.04±0.1	*G2* V	3.8	1.02 ±0.07	2.43 ±0.16	0.046	Csizmadia et al. (2011)
CoRoT-27 b	1.05±0.11	*G2*	3.6	1.01 ±0.04	10.39±0.55	0.047	Parviainen et al. (2014)
CoRoT-6 b	1.05±0.05	*F9* V	8.9	1.17 ±0.04	2.96 ±0.34	0.085	Fridlund et al. (2010)
CoRoT-12 b	1.08±0.08	*G2* V	2.8	1.44 ±0.13	0.917±0.065	0.040	Gillon et al. (2010)
CoRoT-13 b	1.09±0.02	*G0* V	4.0	0.89 ±0.01	1.308±0.066	0.051	Cabrera et al. (2010)
CoRoT-25 b	1.09±0.11	*G0* V	4.9	1.08 ±0.1	0.27 ±0.04	0.058	Almenara et al. (2013)
CoRoT-26 b	1.09±0.06	*G8* IV	4.2	1.26 ±0.07	0.52 ±0.05	0.052	Almenara et al. (2013)
CoRoT-16 b	1.10±0.08	*G5* V	5.4	1.17 ±0.14	0.535±0.085	0.062	Ollivier et al. (2012)
CoRoT-22 b	1.10±0.05	*G0* IV	9.8	0.44 ±0.03	0.038±0.028	0.092	Moutou et al. (2014)
CoRoT-14 b	1.13±0.09	*F9* V	1.5	1.09 ±0.07	7.6 ±0.6	0.027	Tingley et al. (2011)
CoRoT-20 b	1.14±0.08	*G2* V	9.2	0.84 ±0.04	4.24 ±0.23	0.090	Deleuil et al. (2012)
CoRoT-23 b	1.14±0.08	*G0* V	3.6	1.05 ±0.13	2.8 ±0.30	0.048	Rouan et al. (2012)
CoRoT-4 b	1.16±0.03	*F8* V	9.2	1.19 ±0.05	0.72 ±0.08	0.090	Moutou et al. (2008)
CoRoT-19 b	1.21±0.05	*F9* V	3.9	1.29 ±0.03	1.11 ±0.06	0.052	Guenther et al. (2012a)
CoRoT-21 b	1.29±0.09	*F8* IV	2.7	1.3 ±0.14	2.26 ±0.31	0.041	Pätzold et al. (2012)
CoRoT-15 b	1.32±0.12	*F7* V	3.1	1.12 ±0.3	63.3 ±4.1	0.045	Bouchy et al. (2011)
CoRoT-3 b	1.41±0.08	*F3* V	4.3	1.01 ±0.07	22.12±1.5	0.058	Deleuil et al. (2008); Tsantaki et al. (2014)
LRc07_E2_0307 b	1.43±0.04	*F6* V	5.6	1.8 ±0.1	<3.01	0.070	this work
LRc09_E2_3322 b*	1.5	*F3* V	3.2	2.60	<20	0.049	Grziwas et al. in prep.
LRc08_E2_4203 b*	1.5	*F3* V	3.29	0.8	< 66	0.05	this work
CoRoT-11 b	1.56±0.10	*F6* V	3.0	1.43 ±0.03	2.67 ±0.3	0.047	Gandolfi et al. (2010); Tsantaki et al. (2014)
LRc03_E2_2657 b*	1.93	*A7* V	5.15	0.7	< 80	0.07	this work
LRa02_E1_1475 b	1.98±0.05	*A7* IV	2.1	1.6 ±0.1	81.5 ±4.8	0.040	this work
LRa02_E2_4150 b	4.2±0.2	*B4* V	8.2	1.8 ±0.2	63.6 ±2.2	0.128	this work

Table 7.5: Sub-stellar objects, found in the CoRoT survey sorted by the mass of the host-star. The vertical line marks the host-star mass that are $\gtrsim 1.3\,M_\odot$ and, thus the IMSs. Objects, marked by an * mark unsolved cases.

These objects cover stellar masses from 0.86 to 5 $M_\odot$ and are shown in Table 7.5. For completeness also the unsolved candidates from this survey LRc08_E2_4203 and LRc03_E2_2657 as well as the planet candidate LRc09_E2_3322, which was newly discovered by Sascha Grizwa, are shown and marked by *.

Since Tsantaki et al. (2014) improved and updated the masses of the host-stars of CoRoT-3 b and CoRoT-11 b, I re-calculated their masses and semi-mayor axis. The group of IMSs (from 1.3 to 2.1 $M_\odot$) is marked in Table 7.5 by horizontal lines. On the lower end CoRoT-21 belongs to this group within the error-bars. Thus, six stars in the mass range of IMSs have been identified as host stars of sub-stellar objects. Some of these sub-stellar objects orbit in relatively wide orbits and, thus, cannot be compared to the population of Hot Jupiters. As shown for example, in Chiang & Laughlin (2013) the population of Hot Jupiters includes all massive planets that are closer than 0.1 AU from their host stars.

CoRoT-9 b does not fulfil this criterion. It orbits at 0.4 AU or at 93 stellar radii relative to its host star. This criterion does not include the radius of the host star. The brown dwarf candidate LRa02_E2_4150 b for example orbits at a distance of 0.14 AU. This value excludes it from the sample of close-in objects. On the other hand, due to the large radius

of its host-star, its separation is only 9.7 stellar radii. This is the same value than for the very close-in planets CoRoT-29 b and CoRoT-25 b. Nevertheless, to derive the frequency of close-in companions and compare it to the literature all companions have to be closer to the star than 0.1 AU. Therefore, I leave out: CoRoT-9 b (0.4 AU), CoRoT 10b (0.11 AU), as well as the massive brown dwarf candidate LRa02_E2_4150 b. Furthermore, I do not use CoRoT-7 c for the analysis, since it is not a transiting planet.
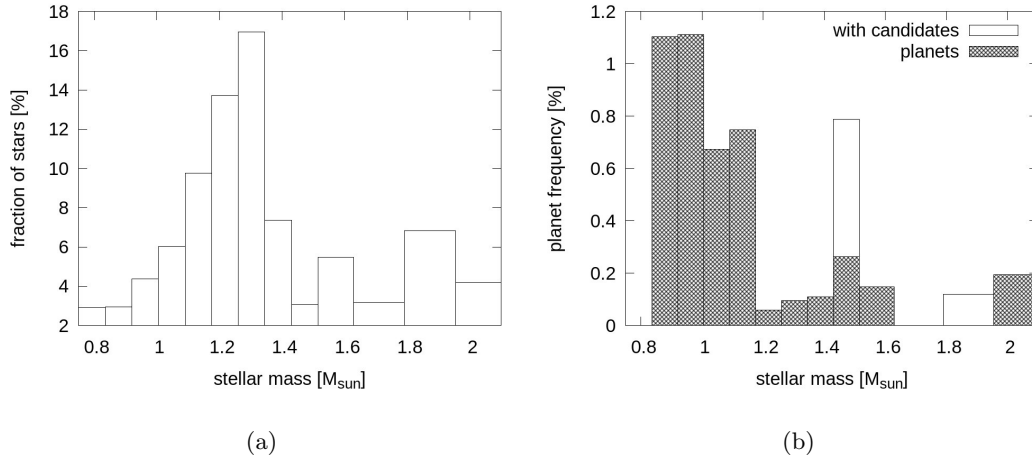

Figure 7.5: (a) Distribution of spectral types of main-sequence and sub-giant stars in the CoRoT survey derived from low-resolution spectroscopy.; (b) the absolute frequencies of close-in planets found in the CoRoT survey. The influence of unconfirmed planet candidates is shown as empty boxes.

To cover the whole mass-range of planet-host stars identified in the CoRoT mission, I analysed the stellar population from 0.75 - 2.1 $M_\odot$. To calculate the statistic, I used a constant bin-size of 0.085 $M_\odot$ for solar-type and low-mass IMSs ($< 1.6\,M_\odot$), but a variable bin-size for higher mass stars to include each two spectral sub-classes per mass-bin. The number of close-in planets found with CoRoT is biased to the actual number of stars observed by CoRoT. In chapter 3, I calculated the number of stars of different masses in three CoRoT anticentre fields (published in Sebastian et al. (2012); Guenther et al. (2012b)). I can assume that this distribution is representative for all CoRoT fields (see section: 7.4.2 for a discussion). Since this classification is done for stars actually observed with CoRoT, the distribution is, thus, not biased to selection effects of the CoRoT mission. 7131 stars have been spectroscopically classified. 74.9 % of them are main sequence or sub-giant stars. The stellar distribution is shown in Figure 7.5 (a). The conversion from spectral types to stellar masses is done by comparing them with values from the literature (Gray 2005).

In the CoRoT- mission, light curves of 163 664 stars have been processed and analysed (Moutou et al. 2013). Thus, I can calculate the absolute number of CoRoT targets per mass-bin by using the information that 74.9 % of all of them are main-sequence or sub-giant stars as well as the distribution of those stars shown in Figure 7.5 (a). With this distribution the actual number of detected planets per mass-bin (see Table 7.5) can be normalised to obtain an absolute frequency of planets. Finally I multiplied the frequency obtained per mass-bin by 10 to account for the typical geometrical probability to detect a transiting planet if the orbital planes are orientated randomly (see chapter 2). To derive for example the planet-frequency for the spectral-types $F8$-$F9$, I first determine the mass-range from 1.175-1.26 $M_\odot$. From

the stellar population, as shown in Figure 7.5 (a), 13.72 % of 74.9 % of all stars observed by CoRoT are in this mass-bin. With $1.21\,M_\odot$ only CoRoT-19 is located in this mass-bin. Thus, by correcting for the geometrical probability the absolute frequency of planets in this mass-bin is 0.06 %. All calculated planet frequencies are displayed in Figure 7.5 (b).

From these absolute frequencies per mass-bin, the mean planet-frequency for close-in planets in a larger mass-range can be derived. I obtain 0.79 ± 0.23 % for stars with masses $< 1.3\,M_\odot$ and 0.11 ± 0.04 % for IMSs between 1.3 and $2.1\,M_\odot$. As shown in Figure 7.5 (b), this confirms that there is a true lack of transiting close-in planets for stars more massive than $1.1\,M_\odot$. It is interesting to note that the most frequent stars in the CoRoT survey are in the mass region around 1.26-1.35 $M_\odot$ (*F*6-*F*7 V stars). On the other hand, only 2 close-in planets have been found in the same region. This confirms that this finding is not only an artefact of selection effects but a real cut-off for the frequency of close-in planets.

7.4.2 Discussion on the planet frequency

Some assumptions have been used to calculate the planet frequency. In the following, I will highlight them and discuss their influence to the observed result:

1.) All planets have been detected in the survey: I derived a mean frequency for close-in planets of solar-type stars of 0.79 ± 0.23 %. This is fully consistent with the findings from radial velocity surveys. Naef et al. (2005) derived for close-in planets with $P < 5\,d$ a frequency of 0.7 ± 0.5 % and Cumming et al. (2008) found 0.65 ± 0.4 %. This perfect agreement with the frequency derived in this survey confirms that all close-in Hot Jupiters from solar-like stars have been detected within the CoRoT-survey. For IMSs, planets with small radii are not easy to detect and, thus, a selection effect due to the size of the planets is introduced. Nevertheless, The accuracy of the CoRoT light curves is high enough to detect all transiting planets of IMSs with radii $\geq 1\,R_{Jup}$. The three unconfirmed candidates are shown in Figure 7.5 (b) as empty boxes to indicate their unconfirmed status. Especially in the mass-bin from 1.43-1.52 $M_\odot$ the planet frequency would be 0.79 % if the candidates LRc09_E2_3322 b and LRc08_E2_4203 b are confirmed. Adding all tree candidates the mean planet-frequency for IMSs would be 0.21 ± 0.12 %. Even if single candidates would be confirmed in future, the frequency for close-in planets of IMSs would still be significantly smaller than that for solar-type stars. The empty boxes close to M=1.5 $M_\odot$ in Figure 7.5 (b) show that 2-4 more planets per-mass bin have to be detected to obtain the same planet frequency for IMSs than for solar-type stars. This work obviously shows that within the accuracy obtained with CoRoT this scenario can be excluded for close-in planets with radii $\geq 1\,R_{Jup}$.

2. The statistical relevance is satisfied with the number of stars observed by CoRoT: The frequency for stars $< 1.3\,M_\odot$ is based on 25 detected sub-stellar objects and for IMSs on 6 detected sub-stellar objects. For a frequency of 0.8 % a minimum of 1250 stars have to be analysed to find one transiting planet. Per mass-bin at least 3600 stars have been analysed, which would yield statistically 2 to 3 planets per-mass bin for stars $< 1.3\,M_\odot$. Since I found a frequency of 0.1 % for IMSs, at least 9100 stars have to be analysed to find one transiting planet. The zero detections can be explained, since the smallest number of analysed stars per mass-bin is 3600. The calculated frequencies per mass-bin for IMSs are thus only an upper limit. Nevertheless, the calculated mean frequency for IMSs is statistically

very significant since about 57 000 light curves have been analysed in this mass-range.

3. The spectral distribution is the same for all CoRoT fields: Gazzano et al. (2010) found that the population in anticentre and centre direction in the first CoRoT fields is almost the same. Since the complete CoRoT survey is restricted to a very limited area in the sky and the pre-selection was done in the same way, I do not expect a dramatic change in the distribution of stars (see section: 3.3.2 for more details). However, in the case that the measured stellar population would slightly change for different CoRoT fields, the overall distribution of stars will change. How does the derived planet frequency change with a different stellar population? In the case that more IMSs would have been observed, the planet frequency for IMSs would be even smaller. Since the obtained frequency is an upper limit this case would not influence the result of this work at all. On the other hand, it could be possible that the number of IMSs is overestimated. In this case I assume that the most frequently observed stars would be solar-mass stars with M$\sim 1\,M_\odot$. The derived difference between the planet-frequency of solar-mass and IMSs would only be a factor 4, but it would still be significant. I thus can confirm that the assumption that the spectral distribution is the same for all CoRoT fields does not influence to the result that there is a lack of close-in planets of IMSs.

8 Conclusions

Compared to planets of solar-mass stars not much is known for planets of intermediate-mass stars (IMSs) with masses from 1.3 to 2.1 $M_\odot$. The planets of IMSs detected so far have on average larger separations and higher masses than planets of solar-type stars. From RV-surveys of evolved stars it is known that the frequency of planets at distances larger than 5 AU is higher in comparison to solar-mass stars. On the other hand, those surveys also report an apparent lack of close-in planets. This can be due, first, to a selection effect because of the sample of evolved stars. In this case, as long as these stars are on the main-sequence the frequency of close-in planets for IMSs should also be high like the frequency of planets with larger orbits. After these stars evolve their close-in planets will be engulfed. Second, those close-in planets of IMSs do not form. This would for example be the case if migration processes are less efficient than for solar-mass stars. To find out, which explanation is true the only thing to do is to derive the planet frequency for close-in planets of IMSs as long, as they are on the main sequence. Hasegawa & Pudritz (2013) predict that this frequency will increase linearly with stellar mass and is 5-11 % for IMSs. On the other hand, if those planets do not form efficiently, Currie (2009) predict a frequency of main-sequence IMSs with close-in planets of less than 1.5 %.

To calculate the frequency of close-in planets of IMSs empirically, I carried out a four years survey for close-in sub-stellar companions of IMSs on the main-sequence. Transit surveys are not biased towards solar-type stars, thus, the main source for this survey is the CoRoT mission. The accuracy of the CoRoT light curves allows one to detect all transiting close-in (< 0.1 AU) planets of IMSs with radii R $> 1\,R_{Jup}$. This survey was done in two mayor steps: First, a sample of 7 131 stars in the anticentre direction of CoRoT was spectroscopically classified to characterise the distribution of stars of the CoRoT survey. This classification is based on low-resolution spectra obtained with the AAOmega multi-object spectrograph (see chapter 3). From this classification, I obtained two main results: First, 32.8 % of all main sequence stars in the CoRoT survey are IMSs. This result confirms that the CoRoT survey is ideal to analyse the frequency for close-in planets of IMSs. Second, I obtained the distribution of main-sequence stars in the survey (see Figure 7.5 (a)). This result is important to calculate the absolute frequency of close-in planets in the survey. In a second step,

Number	status
4	close-in binaries
3	long periodic binaries
1	planet
2	brown dwarfs
2	planet-candidates
3	false alarms

Table 8.1: Result of the survey in numbers.

14 promising candidates among the IMSs with periods between 0.6 to 14 days were selected from the CoRoT light curves. These are distributed equally in the centre and anticentre direction of CoRoT. Some of these candidates were already found in the regular survey. Since they were identified as rapid rotators from high-resolution spectroscopy, no further follow-up observations were scheduled. The reason for this is that a rapid rotation as well as stellar

pulsations limit the accuracy of the RV-measurements. Therefore, the RV semi-amplitudes of planets with small masses ($M < 1 M_{Jup}$) are not detectable for IMSs (see chapter: 5). On the other hand, IMSs harbour on average more massive planets than solar-mass stars. Therefore, the RV-variations caused by massive close-in planets can still be detected. In an intensive analysis including database-research as well as an intensive follow-up program with low-resolution-, high-resolution spectroscopy, and imaging these candidates were studied in detail.

The results are summarised in Table 8.1. Among the three long periodic binaries the object LRa02_E2_4150 shows a transiting brown dwarf companion orbiting the primary component. Three objects turned out to be false alarms. For one of them (LRc10_E2_3265), the light curve of shows an increasing brightness after the transit, indicating periastron brightening. This effect is known from eccentric binaries and is also visible in the light curves of the close-in binaries LRa01_E2_1578, LRa02_E1_0725, and LRc07_E2_0108. These binaries show RV-variations that match best to eccentric orbit solutions. Therefore, for the analysis of light curves a brightening directly before of after the transit turned out to be a good indicator for a false alarm.

The two brown dwarfs, LRa02_E2_4150 b and LRa02_E1_1475 b are very massive and just on the border to low-mass stars. LRa02_E2_4150 b orbits a B-type star and is, therefore, the first brown dwarf orbiting a star that is more than four times more massive than the Sun. With $1.8\,R_{Jup}$ it is much larger than other brown dwarfs in the same mass region. This is the same for LRa02_E1_1475 b. It is located extreme close to its star. Its orbital separation is only $3\,R_{\star}$ and is, thus, relative to the size of the star closer than CoRoT-7b. The resulting ellipsoidal variations are visible in the light curve and confirm the existence of this massive object. The large radii of both objects are much larger than expected for typical brown dwarfs. Since these objects are young, this measurement confirms that brown dwarfs have large radii in the first million years. Both have a relatively short existence. LRa02_E2_4150 b has to be younger than 20 Myr, since it orbits a B-type star. Since the host star of LRa02_E1_1475 b is slightly evolved and the companion is extremely close to its star, it will be engulfed within the next two million years, when the star becomes a giant.

Finally, the candidate LRc07_E2_0307 b turned out to be a close-in planet. AO-imaging and further resolved transit observations exclude any contamination of the background and confirm that the transit originates from this star. Furthermore, time-resolved spectroscopy shows evidence for a Rossiter-McLaughlin effect that results in a obliquity of the orbital plane of almost $90°$.

Due to the accuracy of CoRoT the survey is complete for close-in ($< 0.1\,\mathrm{AU}$) Jupiter-like planets with radii R $> 1\,R_{Jup}$. I thus, derived the number of planets, detected for different stellar masses. This was done by analysing all planets detected in both in this work and in the main CoRoT survey. Based on the distribution of stars in the CoRoT survey derived in the first step of this work, I obtained the absolute frequency of close-in planets for different stellar masses (see Figure 7.5 (b)). The mean frequency for close-in planets is $0.79 \pm 0.23\,\%$ for stars with masses $< 1.3\,M_{\odot}$. This is in perfect agreement with previous results from radial-velocity surveys and confirms therefore that the CoRoT survey is essential complete for close-in hot Jupiters. For IMSs between 1.3 and $2.1\,M_{\odot}$, I obtained a mean frequency of $0.11 \pm 0.04\,\%$. This frequency is significantly smaller than for solar-mass stars. The result

furthermore, shows that there is a lack of transiting close-in planets for main-sequence stars more massive than $1.1\,M_\odot$. I have shown that this result is highly significant. First due to the high number of stars analysed in the CoRoT survey, and second due to the intensity of the effect itself. Even if the spectral distribution changes in different fields of CoRoT, this effect would still be detectable. Nevertheless, an analysis of the distribution of the planet frequency in different fields of CoRoT is beyond the scope of this work. Furthermore, the number of stars, analysed with CoRoT is too small to calculate this frequencies. This result means that close-in planets of IMSs are less frequent than long-periodic planets of IMSs ($\sim 11\,\%$) and they are less frequent than close-in planets of solar-type stars ($0.8\,\%$). The high planet frequency that was observed for evolved IMSs for planets at distances $>0.5\,$AU is not observed for close-in ($< 0.1\,$AU) planets of main-sequence IMSs.

In the common theories of planet formation massive gas-giants form in large distances from their host-stars. Furthermore, IMSs have larger protostellar discs than solar-mass stars. In these discs more planets can form. Thus, the previous observational result that the frequency for IMSs of planets in large separations is higher than for solar-mass stars is fully consistent to these theories. To finally form hot Jupiters these planets have to migrate inwards to reach their close-in orbits. In the context of disc-migration, the surprising result that close-in planets are extremely rare can be explained by the lifetime of the protostellar discs of IMSs. It is apparently long enough, so that hot Jupiters can form, but on average not long enough for them to migrate inwards. Nevertheless, this survey shows that the formation of hot Jupiters has to be less efficient for IMSs than for solar-mass stars.

References

Aceituno, J., Sánchez, S. F., Grupp, F., et al. 2013, Astron. & Astrophys., 552, A31

Aigrain, S., Pont, F., Fressin, F., et al. 2009, Astron. & Astrophys., 506, 425

Alexander, R., Pascucci, I., Andrews, S., Armitage, P., & Cieza, L. 2014, Protostars and Planets VI, 475

Alibert, Y., Mordasini, C., & Benz, W. 2011, Astron. & Astrophys., 526, A63+

Almenara, J. M., Bouchy, F., Gaulme, P., et al. 2013, Astron. & Astrophys., 555, A118

Alonso, R., Auvergne, M., Baglin, A., et al. 2008, Astron. & Astrophys., 482, L21

Alonso, R., Moutou, C., Endl, M., et al. 2014, Astron. & Astrophys., 567, A112

Alonso-Floriano, F. J., Morales, J. C., Caballero, J. A., et al. 2015, Astron. & Astrophys., 577, A128

Ammler-von Eiff, M., Sebastian, D., Guenther, E. W., Stecklum, B., & Cabrera, J. 2015, Astronomische Nachrichten, 336, 134

Anglada-Escudé, G. & Butler, R. P. 2012, Astrophys. J. Suppl, 200, 15

Baglin, A., Auvergne, M., Barge, P., et al. 2002, in ESA Special Publication, Vol. 485, Stellar Structure and Habitable Planet Finding, ed. B. Battrick, F. Favata, I. W. Roxburgh, & D. Galadi, 17–24

Bakos, G. Á., Noyes, R. W., Kovács, G., et al. 2009, in IAU Symposium, Vol. 253, IAU Symposium, ed. F. Pont, D. Sasselov, & M. J. Holman, 21–27

Ballard, S., Fabrycky, D., Fressin, F., et al. 2011, ApJ, 743, 200

Baraffe, I., Chabrier, G., Allard, F., & Hauschildt, P. H. 2002, Astron. & Astrophys., 382, 563

Baranne, A., Mayor, M., & Poncet, J. L. 1979, Vistas in Astronomy, 23, 279

Baranne, A., Queloz, D., Mayor, M., et al. 1996, A&A Suppl., 119, 373

Barge, P., Baglin, A., Auvergne, M., et al. 2008, Astron. & Astrophys., 482, L17

Barros, S. C. C., Almenara, J. M., Deleuil, M., et al. 2014, Astron. & Astrophys., 569, A74

Beech, M. 1987, Astrophys. & Space Sc., 132, 269

Boisnard, L. & Auvergne, M. 2006, in ESA Special Publication, Vol. 1306, ESA Special Publication, ed. M. Fridlund, A. Baglin, J. Lochard, & L. Conroy, 19

Bond, I. A., Udalski, A., Jaroszyński, M., et al. 2004, Astrophys. J. Letters, 606, L155

Bonomo, A. S., Santerne, A., Alonso, R., et al. 2010, Astron. & Astrophys., 520, A65

Bordé, P., Bouchy, F., Deleuil, M., et al. 2010, Astron. & Astrophys., 520, A66

Borucki, W. J., Koch, D. G., Batalha, N., et al. 2012, The Astrophysical Journal, 745, 120

Borucki, W. J. & Summers, A. L. 1984, Icarus, 58, 121

Boss, A. P. 1997, Science, 276, 1836

Bouchy, F., Deleuil, M., Guillot, T., et al. 2011, Astron. & Astrophys., 525, A68

Bouchy, F., Pepe, F., & Queloz, D. 2001, Astron. & Astrophys., 374, 733

Boulade, O., Charlot, X., Abbon, P., et al. 2003, in Society of Photo-Optical Instrumentation Engineers (SPIE) Conference Series, Vol. 4841, Instrument Design and Performance for Optical/Infrared Ground-based Telescopes, ed. M. Iye & A. F. M. Moorwood, 72–81

Bowler, B. P., Johnson, J. A., Marcy, G. W., et al. 2010, ApJ, 709, 396

Brown, T. M. 2003, Astrophys. J. Letters, 593, L125

Brown, T. M. 2008, in Extrasolar Planets, ed. H. Deeg, J. A. Belmonte, & A. Aparicio, 65

Burrows, A., Hubbard, W. B., Lunine, J. I., & Liebert, J. 2001, Reviews of Modern Physics, 73, 719

Burrows, A., Sudarsky, D., & Hubeny, I. 2004, ApJ, 609, 407

Cabrera, J., Bruntt, H., Ollivier, M., et al. 2010, Astron. & Astrophys., 522, A110

Cabrera, J., Csizmadia, S., Erikson, A., Rauer, H., & Kirste, S. 2012, Astron. & Astrophys., 548, A44

Cabrera, J., Csizmadia, S., Montagnier, G., et al. 2015, Astron. & Astrophys., 579, A36

Cameron, A. C., Guenther, E., Smalley, B., et al. 2010, Mon. Not. R. Astron. Soc., 407, 507

Carone, L., Keppens, R., & Decin, L. 2015, Mon. Not. R. Astron. Soc., 453, 2412

Carquillat, J.-M. & Prieur, J.-L. 2007, Mon. Not. R. Astron. Soc., 380, 1064

Charbonneau, D., Berta, Z. K., Irwin, J., et al. 2009, Nature, 462, 891

Charbonneau, D., Brown, T. M., Latham, D. W., & Mayor, M. 2000, Astrophys. J. Letters, 529, L45

Chauvin, G., Lagrange, A.-M., Dumas, C., et al. 2005, Astron. & Astrophys., 438, L25

Chiang, E. & Laughlin, G. 2013, Mon. Not. R. Astron. Soc., 431, 3444

Christian, D. J., Pollacco, D. L., Clarkson, W. I., et al. 2005, in ESA Special Publication, Vol. 560, 13th Cambridge Workshop on Cool Stars, Stellar Systems and the Sun, ed. F. Favata, G. A. J. Hussain, & B. Battrick, 475

Christian, D. J., Pollacco, D. L., Skillen, I., et al. 2006, Mon. Not. R. Astron. Soc., 372, 1117

Csizmadia, S. 2016, III.6 Exploration of the brown dwarf regime around solar-like stars by CoRoT, ed. CoRot Team, 143

Csizmadia, S., Hatzes, A., Gandolfi, D., et al. 2015, Astron. & Astrophys., 584, A13

Csizmadia, S., Moutou, C., Deleuil, M., et al. 2011, Astron. & Astrophys., 531, A41

Cui, X.-Q., Zhao, Y.-H., Chu, Y.-Q., et al. 2012, Research in Astronomy and Astrophysics, 12, 1197

Cumming, A., Butler, R. P., Marcy, G. W., et al. 2008, Publ. Astron. Soc. Japan, 120, 531

Currie, T. 2009, Astrophys. J. Letters, 694, L171

da Silva, R., Maceroni, C., Gandolfi, D., Lehmann,

H., & Hatzes, A. P. 2014, Astron. & Astrophys., 565, A55

David, T. J. & Hillenbrand, L. A. 2015, ApJ, 804, 146

de Cuyper, J.-P. & Hensberge, H. 1998, A&A Suppl., 128, 409

Deeg, H. J. 2015, Astron. & Astrophys., 578, A17

Deeg, H. J., Gillon, M., Shporer, A., et al. 2009, Astron. & Astrophys., 506, 343

Deeg, H. J., Moutou, C., Erikson, A., et al. 2010, Nature, 464, 384

Dekker, H., D'Odorico, S., Kaufer, A., Delabre, B., & Kotzlowski, H. 2000, in Society of Photo-Optical Instrumentation Engineers (SPIE) Conference Series, Vol. 4008, Optical and IR Telescope Instrumentation and Detectors, ed. M. Iye & A. F. Moorwood, 534–545

Deleuil, M., Bonomo, A. S., Ferraz-Mello, S., et al. 2012, Astron. & Astrophys., 538, A145

Deleuil, M., Deeg, H. J., Alonso, R., et al. 2008, Astron. & Astrophys., 491, 889

Deleuil, M., Meunier, J. C., Moutou, C., et al. 2009, Astronom. J., 138, 649

D'Odorico, S., Cristiani, S., Dekker, H., et al. 2000, in Proc. SPIE, Vol. 4005, Discoveries and Research Prospects from 8- to 10-Meter-Class Telescopes, ed. J. Bergeron, 121–130

Döllinger, M. P., Hatzes, A. P., Pasquini, L., et al. 2011, in American Institute of Physics Conference Series, Vol. 1331, American Institute of Physics Conference Series, ed. S. Schuh, H. Drechsel, & U. Heber, 79–87

Donati, J.-F., Semel, M., Carter, B. D., Rees, D. E., & Collier Cameron, A. 1997, Mon. Not. R. Astron. Soc., 291, 658

Dong, S. & Zhu, Z. 2013, ApJ, 778, 53

Doyle, L. R. 2008, in Extrasolar Planets, ed. H. Deeg, J. A. Belmonte, & A. Aparicio, 1

Dupret, M.-A., Miglio, A., Grigahcène, A., & Montalbán, J. 2007, Communications in Asteroseismology, 150, 98

Duquennoy, A. & Mayor, M. 1992, Binaries as Tracers of Stellar Formation

Eastman, J., Siverd, R., & Gaudi, B. S. 2010, Publ. Astron. Soc. Japan, 122, 935

Endl, M., Brugamyer, E. J., Cochran, W. D., et al. 2016, ApJ, 818, 34

Fabricius, C., Høg, E., Makarov, V. V., et al. 2002, Astron. & Astrophys., 384, 180

Faigler, S. & Mazeh, T. 2011, Mon. Not. R. Astron. Soc., 415, 3921

Favata, F. & Micela, G. 2003, Space Science Reviews, 108, 577

Fielding, D. B., McKee, C. F., Socrates, A., Cunningham, A. J., & Klein, R. I. 2015, Mon. Not. R. Astron. Soc., 450, 3306

Florentin-Nielsen, R., Andersen, M. J., & Nielsen, S. P. 1995, in IAU Symposium, Vol. 167, New Developments in Array Technology and Applications, ed. A. G. D. Philip, K. Janes, & A. R. Upgren, 207

Fressin, F., Torres, G., Désert, J.-M., et al. 2011, Astrophys. J. Suppl, 197, 5

Fridlund, M., Hébrard, G., Alonso, R., et al. 2010, Astron. & Astrophys., 512, A14

Fuhrmann, K. 1998, Astron. & Astrophys., 338, 161

Fuhrmann, K. 2004, Astronomische Nachrichten, 325, 3

Fuhrmann, K. 2008, Mon. Not. R. Astron. Soc., 384, 173

Fuhrmann, K. 2011, Mon. Not. R. Astron. Soc., 414, 2893

Gandolfi, D., Hébrard, G., Alonso, R., et al. 2010, Astron. & Astrophys., 524, A55

Gazzano, J.-C., de Laverny, P., Deleuil, M., et al. 2010, Astron. & Astrophys., 523, A91

Georgy, C., Ekström, S., Granada, A., et al. 2013, Astron. & Astrophys., 553, A24

Gillon, M., Hatzes, A., Csizmadia, S., et al. 2010, Astron. & Astrophys., 520, A97

Girardi, L., Bressan, A., Bertelli, G., & Chiosi, C. 2000, A&A Suppl., 141, 371

Gray, D. F. 2005, The Observation and Analysis of Stellar Photospheres

Gray, D. F. & Brown, K. I. T. 2006, Publ. Astron. Soc. Japan, 118, 399

Gray, R. O. & Corbally, J., C. 2009, Stellar Spectral Classification, ed. Gray, R. O. & Corbally, C., J. (Princeton: Princeton University Press)

Grziwa, S., Pätzold, M., & Carone, L. 2012, Mon. Not. R. Astron. Soc., 420, 1045

Guenther, E. W., Díaz, R. F., Gazzano, J.-C., et al. 2012a, Astron. & Astrophys., 537, A136

Guenther, E. W., Fridlund, M., Alonso, R., et al. 2013, Astron. & Astrophys., 556, A75

Guenther, E. W., Gandolfi, D., Sebastian, D., et al. 2012b, Astron. & Astrophys., 543, A125

Guenther, E. W. & Geier, S. 2015, in Astrophysics and Space Science Library, Vol. 411, Astrophysics and Space Science Library, ed. H. Lammer & M. Khodachenko, 169

Hareter, M., Paparó, M., Weiss, W., et al. 2014, Astron. & Astrophys., 567, A124

Hartman, J. D., Bakos, G. Á., Buchhave, L. A., et al. 2015, ArXiv e-prints

Hasegawa, Y. & Pudritz, R. E. 2013, ApJ, 778, 78

Hatzes, A. P., Cochran, W. D., & Endl, M. 2010, in Astrophysics and Space Science Library, Vol. 366, Astrophysics and Space Science Library, ed. N. Haghighipour, 51

Hatzes, A. P., Cochran, W. D., Endl, M., et al. 2006, Astron. & Astrophys., 457, 335

Hatzes, A. P., Fridlund, M., Nachmani, G., et al. 2011, ApJ, 743, 75

Hatzes, A. P. & Rauer, H. 2015, Astrophys. J. Letters, 810, L25

Haywood, R. D., Collier Cameron, A., Queloz, D., et al. 2014, Mon. Not. R. Astron. Soc., 443, 2517

Hébrard, G., Evans, T. M., Alonso, R., et al. 2011, Astron. & Astrophys., 533, A130

Herrero, E., Morales, J. C., Ribas, I., & Naves, R. 2011, Astron. & Astrophys., 526, L10

Hidas, M. G., Ashley, M. C. B., Webb, J. K., et al. 2005, Mon. Not. R. Astron. Soc., 360, 703

Howell, S. B., Sobeck, C., Haas, M., et al. 2014, Publ. Astron. Soc. Japan, 126, 398

Huang, Y., Liu, X.-W., Zhang, H.-W., et al. 2015, Research in Astronomy and Astrophysics, 15, 1240

Ida, S. & Lin, D. N. C. 2005, ApJ, 626, 1045

Iorio, L. 2011, Mon. Not. R. Astron. Soc., 411, 167

Iorio, L. 2016, Mon. Not. R. Astron. Soc., 455, 207

Jenkins, J. M., Twicken, J. D., Batalha, N. M., et al. 2015, Astronom. J., 150, 56

Johnson, J. A., Aller, K. M., Howard, A. W., & Crepp, J. R. 2010, Publ. Astron. Soc. Japan, 122, 905

Johnson, M. C., Cochran, W. D., Collier Cameron, A., & Bayliss, D. 2015, Astrophys. J. Letters, 810, L23

Jones, M. I., Jenkins, J. S., Bluhm, P., Rojo, P., & Melo, C. H. F. 2014, Astron. & Astrophys., 566, A113

Kasting, J. F., Whitmire, D. P., & Reynolds, R. T. 1993, Icarus, 101, 108

Kennedy, G. M. & Kenyon, S. J. 2008, ApJ, 673, 502

Koch, D. G., Borucki, W. J., Basri, G., et al. 2010, Astrophys. J. Letters, 713, L79

Kokubo, E. & Ida, S. 2002, ApJ, 581, 666

Kozai, Y. 1962, Astronom. J., 67, 591

Kupka, F. G., Ryabchikova, T. A., Piskunov, N. E., Stempels, H. C., & Weiss, W. W. 2000, Baltic Astronomy, 9, 590

Kurtz, D. W., Elkin, V. G., & Mathys, G. 2005, Mon. Not. R. Astron. Soc., 358, L6

Kurucz, R. L. 2006, ArXiv Astrophysics e-prints

Latham, D. W., Stefanik, R. P., Mazeh, T., Mayor, M., & Burki, G. 1989, Nature, 339, 38

Lee, J. W., Kim, S.-L., Kim, C.-H., et al. 2009, Astronom. J., 137, 3181

Léger, A., Rouan, D., Schneider, J., et al. 2009, Astron. & Astrophys., 506, 287

Lehmann, H., Guenther, E., Sebastian, D., et al. 2015, Astron. & Astrophys., 578, L4

Lehmann, H., Tkachenko, A., Semaan, T., et al. 2011, Astron. & Astrophys., 526, A124

Lenz, P. & Breger, M. 2004, in IAU Symposium, Vol. 224, The A-Star Puzzle, ed. J. Zverko, J. Ziznovsky, S. J. Adelman, & W. W. Weiss, 786–790

Loeb, A. & Gaudi, B. S. 2003, Astrophys. J. Letters, 588, L117

Lovis, C. & Mayor, M. 2007, Astron. & Astrophys., 472, 657

Magakian, T. Y. 2003, Astron. & Astrophys., 399, 141

Mamajek, E. E. 2009, in American Institute of Physics Conference Series, Vol. 1158, American Institute of Physics Conference Series, ed. T. Usuda, M. Tamura, & M. Ishii, 3–10

Mandel, K. & Agol, E. 2002, Astrophys. J. Letters, 580, L171

Mandushev, G., Torres, G., Latham, D. W., et al. 2005, ApJ, 621, 1061

Marcy, G. W. & Butler, R. P. 1992, Publ. Astron. Soc. Japan, 104, 270

Marcy, G. W. & Butler, R. P. 2000, Publ. Astron. Soc. Japan, 112, 137

Marmier, M., Ségransan, D., Udry, S., et al. 2013, Astron. & Astrophys., 551, A90

Marois, C., Macintosh, B., Barman, T., et al. 2008, Science, 322, 1348

Martins, J. H. C., Santos, N. C., Figueira, P., et al. 2015, Astron. & Astrophys., 576, A134

Mathieu, R. D., Meibom, S., & Dolan, C. J. 2004, Astrophys. J. Letters, 602, L121

Mayor, M., Pepe, F., Queloz, D., et al. 2003, The Messenger, 114, 20

Mayor, M. & Queloz, D. 1995, Nature, 378, 355

Mazeh, T., Nachmani, G., Sokol, G., Faigler, S., & Zucker, S. 2012, Astron. & Astrophys., 541, A56

Mazeh, T., Naef, D., Torres, G., et al. 2000, Astrophys. J. Letters, 532, L55

McCarthy, J. K., Sandiford, B. A., Boyd, D., & Booth, J. 1993, Publ. Astron. Soc. Japan, 105, 881

McLaughlin, D. B. 1924, ApJ, 60, 22

Meeus, J. 1988, Astronomical formulae for calculators

Melo, C. H. F., Covino, E., Alcalá, J. M., & Torres, G. 2001, Astron. & Astrophys., 378, 898

Menu, J., van Boekel, R., Henning, T., et al. 2015, Astron. & Astrophys., 581, A107

Mizuno, H., Nakazawa, K., & Hayashi, C. 1978, Progress of Theoretical Physics, 60, 699

Monnier, J. D., Tuthill, P. G., Ireland, M., et al. 2009, ApJ, 700, 491

Mordasini, C., Mollière, P., Dittkrist, K.-M., Jin, S., & Alibert, Y. 2015, International Journal of Astrobiology, 14, 201

Morgan, W. W., Keenan, P. C., & Kellman, E. 1943, An atlas of stellar spectra, with an outline of spectral classification, ed. Morgan, W. W., Keenan, P. C., & Kellman, E.

Morris, S. L. 1985, ApJ, 295, 143

Motalebi, F., Udry, S., Gillon, M., et al. 2015, ArXiv e-prints

Moutou, C., Almenara, J. M., Díaz, R. F., et al. 2014, Mon. Not. R. Astron. Soc., 444, 2783

Moutou, C., Bruntt, H., Guillot, T., et al. 2008, Astron. & Astrophys., 488, L47

Moutou, C., Deleuil, M., Guillot, T., et al. 2013, Icarus, 226, 1625

Mullally, F., Coughlin, J. L., Thompson, S. E., et al. 2015, Astrophys. J. Suppl, 217, 31

Muterspaugh, M. W., Lane, B. F., Kulkarni, S. R., et al. 2010, Astronom. J., 140, 1657

Naef, D., Mayor, M., Beuzit, J.-L., et al. 2005, in ESA Special Publication, Vol. 560, 13th Cambridge Workshop on Cool Stars, Stellar Systems and the Sun, ed. F. Favata, G. A. J. Hussain, & B. Battrick, 833

Nagasawa, M., Ida, S., & Bessho, T. 2008, ApJ, 678, 498

Ollivier, M., Gillon, M., Santerne, A., et al. 2012, Astron. & Astrophys., 541, A149

Parviainen, H., Gandolfi, D., Deleuil, M., et al. 2014, Astron. & Astrophys., 562, A140

Pasquini, L., Avila, G., Blecha, A., et al. 2002, The Messenger, 110, 1

Pätzold, M., Endl, M., Csizmadia, S., et al. 2012, Astron. & Astrophys., 545, A6

Perryman, M. 2011, The Exoplanet Handbook

Perryman, M., Hartman, J., Bakos, G. Á., & Lindegren, L. 2014, ApJ, 797, 14

Pinheiro da Silva, L., Rolland, G., Lapeyrere, V., & Auvergne, M. 2008, Mon. Not. R. Astron. Soc., 384, 1337

Pollacco, D. L., Skillen, I., Cameron, A. C., et al. 2006, Publ. Astron. Soc. Japan, 118, 1407

Pribulla, T., Sebastian, D., Ammler-von Eiff, M., et al. 2014, Mon. Not. R. Astron. Soc., 443, 2815

Quanz, S. P. 2015, Astrophys. & Space Sc., 357, 148

Quirrenbach, A., Amado, P. J., Caballero, J. A., et al. 2011, in IAU Symposium, Vol. 276, IAU Symposium, ed. A. Sozzetti, M. G. Lattanzi, & A. P. Boss, 545–546

Rasio, F. A. & Ford, E. B. 1996, Science, 274, 954

Rauer, H., Catala, C., Aerts, C., et al. 2014, Experimental Astronomy, 38, 249

Rauer, H., Queloz, D., Csizmadia, S., et al. 2009, Astron. & Astrophys., 506, 281

Reffert, S., Bergmann, C., Quirrenbach, A., Trifonov, T., & Künstler, A. 2015, Astron. & Astrophys., 574, A116

Ribas, I., Guinan, E. F., Güdel, M., & Audard, M. 2005, ApJ, 622, 680

Ricker, G. R., Winn, J. N., Vanderspek, R., et al. 2015, Journal of Astronomical Telescopes, Instruments, and Systems, 1, 014003

Rossat, N., Delmotte, N., Fourniol, N., Pirenne, B., & Dobrzycki, A. 2005, in Astronomical Society of the Pacific Conference Series, Vol. 347, Astronomical Data Analysis Software and Systems XIV, ed. P. Shopbell, M. Britton, & R. Ebert, 674

Rossiter, R. A. 1924, ApJ, 60, 15

Rouan, D., Parviainen, H., Moutou, C., et al. 2012, Astron. & Astrophys., 537, A54

Sahlmann, J., Lazorenko, P. F., Ségransan, D., et al. 2013, Astron. & Astrophys., 556, A133

Sahlmann, J., Ségransan, D., Queloz, D., & Udry, S. 2011, in IAU Symposium, Vol. 276, The Astrophysics of Planetary Systems: Formation, Structure, and Dynamical Evolution, ed. A. Sozzetti, M. G. Lattanzi, & A. P. Boss, 117–120

Santos, N. C., Israelian, G., & Mayor, M. 2004, Astron. & Astrophys., 415, 1153

Sarro, L. M., Debosscher, J., Neiner, C., et al. 2013, Astron. & Astrophys., 550, A120

Saunders, W., Bridges, T., Gillingham, P., et al. 2004, in Society of Photo-Optical Instrumentation Engineers (SPIE) Conference Series, ed. A. F. M. Moorwood & M. Iye, Vol. 5492, 389–400

Schatzman, E. 1962, Annales d'Astrophysique, 25, 18

Schneider, J., Dedieu, C., Le Sidaner, P., Savalle, R., & Zolotukhin, I. 2011, Astron. & Astrophys., 532, A79, exoplanets.eu

Schroeder, D. J. 1967, Applied Optics, 6, 1976

Seager, S. & Mallén-Ornelas, G. 2003, ApJ, 585, 1038

Sebastian, D., Guenther, E. W., Schaffenroth, V., et al. 2012, Astron. & Astrophys., 541, A34

Shalygin, E. V., Markiewicz, W. J., Basilevsky, A. T., et al. 2015, Geophys. Res. Lett., 2015GL064088

Shporer, A., Jenkins, J. M., Rowe, J. F., et al. 2011, Astronom. J., 142, 195

Skrutskie, M. F., Cutri, R. M., Stiening, R., et al. 2006, Astronom. J., 131, 1163

Smalley, B., Kurtz, D. W., Smith, A. M. S., et al. 2011, Astron. & Astrophys., 535, A3

Smith, G. A., Saunders, W., Bridges, T., et al. 2004, in Society of Photo-Optical Instrumentation Engineers (SPIE) Conference Series, ed. A. F. M. Moorwood & M. Iye, Vol. 5492, 410–420

Spiegel, D. S., Burrows, A., & Milsom, J. A. 2011, ApJ, 727, 57

Stassun, K. G., Mathieu, R. D., & Valenti, J. A. 2006, Nature, 440, 311

Stix, M. 1989, The Sun (Springer-Verlag)

Szabó, G. M., Szabó, R., Benkő, J. M., et al. 2011, Astrophys. J. Letters, 736, L4

Telting, J. H., Avila, G., Buchhave, L., et al. 2014, Astronomische Nachrichten, 335, 41

Tian, F., France, K., Linsky, J. L., Mauas, P. J. D., & Vieytes, M. C. 2014, Earth and Planetary Science Letters, 385, 22

Tian, F., Kasting, J. F., & Solomon, S. C. 2009, Geophys. Res. Lett., 36, 2205

Tingley, B., Endl, M., Gazzano, J.-C., et al. 2011, Astron. & Astrophys., 528, A97

Tkachenko, A., Van Reeth, T., Tsymbal, V., et al. 2013, Astron. & Astrophys., 560, A37

Tody, D. 1986, in Society of Photo-Optical Instrumentation Engineers (SPIE) Conference Series, ed. D. L. Crawford, Vol. 627, 733–+

Tonry, J. & Davis, M. 1979, Astronom. J., 84, 1511

Torres, G., Andersen, J., & Giménez, A. 2010, A&A Rev., 18, 67

Tsantaki, M., Sousa, S. G., Santos, N. C., et al. 2014, Astron. & Astrophys., 570, A80

Udalski, A. 2009, in Astronomical Society of the Pacific Conference Series, Vol. 403, Astronomical Society of the Pacific Conference Series, ed. K. Z. Stanek, 110–+

Udry, S. 2010, in In the Spirit of Lyot 2010

Udry, S., Lovis, C., Bouchy, F., et al. 2014, ArXiv e-prints

Valdes, F., Gupta, R., Rose, J. A., Singh, H. P., & Bell, D. J. 2004, Astrophys. J. Suppl, 152, 251

van de Kamp, P. 1982, Vistas in Astronomy, 26, 141

Vigan, A., Chauvin, G., Bonavita, M., et al. 2014, in IAU Symposium, Vol. 299, IAU Symposium, ed. M. Booth, B. C. Matthews, & J. R. Graham, 17–20

Vigan, A., Patience, J., Marois, C., et al. 2012, Astron. & Astrophys., 544, A9

Villaver, E. & Livio, M. 2009, Astrophys. J. Letters,

705, L81

Villaver, E., Livio, M., Mustill, A. J., & Siess, L. 2014, ApJ, 794, 3

Vincent, J.-B., Bodewits, D., Besse, S., et al. 2015, Nature, 523, 63

Vogt, S. S., Allen, S. L., Bigelow, B. C., et al. 1994, in Society of Photo-Optical Instrumentation Engineers (SPIE) Conference Series, Vol. 2198, Instrumentation in Astronomy VIII, ed. D. L. Crawford & E. R. Craine, 362

von Essen, C., Mallonn, M., Albrecht, S., et al. 2015, ArXiv e-prints

Vuissoz, C. & Debernardi, Y. 2004, in Astronomical Society of the Pacific Conference Series, Vol. 318, Spectroscopically and Spatially Resolving the Components of the Close Binary Stars, ed. R. W. Hilditch, H. Hensberge, & K. Pavlovski, 320–322

Waters, L. B. F. M. & Waelkens, C. 1998, Annu. Rev. Astro. Astrophys., 36, 233

Wheatley, P. J., Pollacco, D. L., Queloz, D., et al. 2014, in IAU Symposium, Vol. 299, IAU Symposium, ed. M. Booth, B. C. Matthews, & J. R. Graham, 311–312

Winn, J. N. 2009, in IAU Symposium, Vol. 253, IAU Symposium, ed. F. Pont, D. Sasselov, & M. J. Holman, 99–109

Winn, J. N., Fabrycky, D., Albrecht, S., & Johnson, J. A. 2010, Astrophys. J. Letters, 718, L145

Wittenmyer, R. A., Gao, D., Ming Hu, S., et al. 2015, Publ. Astron. Soc. Japan, 127, 1021

Wittenmyer, R. A., Welsh, W. F., Orosz, J. A., et al. 2005, ApJ, 632, 1157

Wolszczan, A. & Frail, D. A. 1992, Nature, 355, 145

Zhao, G., Zhao, Y.-H., Chu, Y.-Q., Jing, Y.-P., & Deng, L.-C. 2012, Research in Astronomy and Astrophysics, 12, 723

List of Figures

List of Tables

Acknowledgements

A Appendix

A.1 RV-measurements of candidates

Table A1.1: RV-measurements of candidates

Candidate	Instrument	measurements		
		time[HJD]	RV [km/s]	RV-error [km/s]
LRc02_E1_0132	SANDIFORD			
		2456114.68655	-65.44	2.75
		2456115.81200	50.45	0.05
		2456116.67486	13.65	0.03
		2456116.80218	-1.40	0.10
		2456116.89931	-11.25	0.20
		2456117.74837	-92.84	0.01
LRa01_E2_1578	SANDIFORD			
		2455932.80695	27.93	0.17
		2455940.73286	72.38	0.40
		2455943.83277	102.19	0.05
		2455944.78241	51.71	1.16
LRa02_E1_0725	SANDIFORD			
		2455931.84211	34.57	0.59
		2455932.75142	29.18	1.41
		2455942.64734	37.48	0.47
		2455944.63862	45.39	0.59
		2455946.82358	19.28	0.68
LRa01_E2_0203	SANDIFORD First run			
		2455930.68657	51.32	0.04
		2455931.68721	52.90	0.07
		2455931.89848	53.45	0.24
		2455932.72165	52.65	0.09
		2455932.89188	53.23	0.12
		2455937.80095	52.60	0.21
		2455940.83232	51.30	0.29
		2455946.63087	48.58	0.17
	SANDIFORD Second run			
		2456290.71353	54.78	0.39
		2456293.70422	53.44	0.20
		2456293.81325	52.45	0.00
		2456295.70860	53.96	0.01
		2456298.86696	50.88	0.04
		2456299.70108	52.16	0.15
		2456300.68286	52.64	0.08
		2456300.88703	52.79	0.48
	CAFE			
		2456278.55232	43.15	0.00
		2456278.57444	44.20	0.79
		2456280.39903	43.00	1.24
		2456280.61148	42.79	0.11
		2456280.70333	41.87	0.10
		2456281.48594	42.47	0.09
		2456281.50980	42.20	0.14
		2456281.70674	42.45	0.15
	UVES			
		2456587.71560	30.91	0.26

Table A1.1 – Continuation

Candidate	Instrument	measurements		
		time[HJD]	RV [km/s]	RV-error [km/s]
		2456598.83527	35.42	0.18
		2456625.81607	40.89	0.31
		2456626.82636	40.93	0.25
		2456629.69486	41.23	0.15
LRa02_E2_4150	SANDIFORD First run			
		2455930.71916	23.32	1.19
		2455931.80739	23.76	1.02
		2455932.68852	24.04	1.10
		2455937.75734	27.11	1.01
		2455938.66680	29.94	1.13
		2455940.65576	26.48	1.16
		2455942.78786	27.28	1.13
		2455943.68710	23.52	1.07
		2455945.64925	27.07	1.17
	SANDIFORD Second run			
		2456290.76649	21.71	1.21
		2456293.89312	19.63	1.11
		2456298.74494	25.37	1.07
		2456299.77669	17.24	1.13
		2456300.78502	20.42	1.16
	CAFE First run			
		2456280.46146	44.87	0.40
		2456280.66053	43.16	1.44
		2456281.67949	42.72	3.17
	CAFE Second run			
		2457018.56174	26.33	0.15
		2457020.53544	28.86	1.52
		2457021.58635	29.14	0.51
		2457022.53144	30.66	0.55
	HARPS			
		2456329.59680	34.96	0.30
		2456332.55900	32.34	0.73
	FIES First run			
		2456283.64113	33.91	1.53
		2456284.73257	34.91	0.73
	FIES Second run			
		2456296.64008	35.22	0.30
		2456297.71935	33.32	1.06
		2456298.69040	32.09	0.40
	FIES Third run			
		2457050.58743	26.65	0.36
		2457051.47029	30.27	0.27
		2457052.48538	27.45	0.27
		2457053.57644	27.57	0.04
		2457054.42491	26.51	0.22
LRa01_E2_0963	SANDIFORD			
		2455944.71157	37.63	0.20
		2455945.72419	37.46	0.91
		2455946.63879	36.81	0.24
	CAFE			

Table A1.1 – Continuation

Candidate	Instrument	measurements		
		time[HJD]	RV [km/s]	RV-error [km/s]
		2456620.65322	27.33	0.01
		2456620.67517	26.84	0.32
		2456621.61100	26.53	0.51
		2456621.63296	27.44	0.34
		2456629.63108	26.51	0.07
		2456629.66032	26.76	0.19
		2456634.62799	26.44	0.29
		2456634.64994	28.17	0.26
		2456635.51262	26.69	0.24
		2456635.53457	27.20	0.56
		2456636.51622	25.96	0.20
		2456636.53817	27.27	0.20
		2456637.50200	25.14	0.16
		2456637.52396	27.14	0.20
		2456638.55521	23.66	0.65
		2456638.57717	25.22	0.23
	FIES			
		2456650.53149	26.24	0.21
		2456651.50987	26.23	0.15
		2456668.60259	25.59	0.07
		2456740.47331	21.70	0.17
LRa02_E1_1475	HIRES			
		2455962.96299	43.34	6.77
		2455964.87595	42.44	1.47
		2456315.83576	27.45	5.43
		2456315.95414	33.80	14.34
		2456317.94208	29.15	4.56
	HARPS			
		2455546.71708	27.60	1.97
		2455547.71536	44.16	1.75
		2456307.66380	36.34	1.89
		2456308.66913	45.29	2.35
		2456312.68506	42.43	5.72
		2456332.60448	28.60	0.49
		2456334.72000	30.49	6.54
		2456335.63909	46.67	5.63
		2456336.56863	33.64	0.53
		2456353.66197	25.77	1.00
		2456354.65832	44.04	9.29
		2456355.64480	34.42	2.19
		2456360.66932	27.65	4.49
		2456361.53093	41.77	11.33
		2456362.58672	30.77	0.98
		2456364.58864	31.13	1.77
		2456365.58175	45.39	2.99
	UVES			
		2456587.72768	41.12	0.78
		2456587.74101	43.10	1.75
		2456629.67304	38.23	2.02
		2456629.68407	35.59	1.67
		2456656.56692	33.19	3.16
		2456656.57796	34.63	5.17
		2456667.75962	31.70	6.46
		2456667.77063	31.11	1.02
		2456669.79442	34.24	0.84
		2456669.80543	36.40	2.77
		2456675.63855	31.59	3.15
				to be continued

Table A1.1 – Continuation

Candidate	Instrument	measurements		
		time[HJD]	RV [km/s]	RV-error [km/s]
		2456675.64955	31.15	2.56
		2456676.79285	40.28	2.32
		2456676.80386	45.35	0.68
		2456694.55314	36.78	3.18
LRa02_E2_1023	SANDIFORD			
		2455941.66357	38.18	0.20
		2455941.86102	21.45	0.20
		2455943.74867	39.22	0.20
		2455946.75232	38.53	0.20
LRc03_E2_2657	TWIN			
		2456818.53864	6.92	1.19
		2456818.61507	5.67	7.29
		2456819.63481	8.64	0.67
		2456820.41433	10.21	7.60
		2456821.41622	0.09	6.65
		2456821.53623	-0.37	2.60
	HARPS			
		2456452.69441	-1.48	1.51
		2456455.67293	6.00	0.77
	UVES			
		2456863.60736	-11.48	0.10
		2456866.60703	-14.66	1.05
		2456869.49887	-11.59	0.73
		2456870.50113	-11.58	0.36
LRc07_E2_0108	SANDIFORD			
		2456112.72575	3.41	0.10
		2456113.73331	-6.77	0.08
		2456114.66364	-7.82	0.10
		2456115.66603	-13.82	0.10
		2456115.84391	-11.63	0.09
		2456116.72874	-14.56	0.05
		2456117.77434	-17.09	0.14
	TWIN			
		2456818.64877	-13.81	2.00
		2456819.40779	-16.98	2.00
		2456819.41603	-18.75	2.00
		2456820.37144	-18.31	2.00
		2456820.60323	-4.16	2.00
		2456820.61656	-23.01	2.00
		2456820.62448	-13.10	2.00
		2456820.63619	-3.79	2.00
		2456821.37296	-25.09	2.00
		2456821.66176	-17.25	2.00
		2456855.39807	-24.06	2.00
		2456855.60093	-29.20	2.00
		2456855.62255	-65.48	2.00
LRc07_E2_0307	SANDIFORD			
		2456115.69276	19.95	0.21
		2456116.85210	19.02	0.25
		2456117.80003	18.09	0.26
	UVES			
	in transit	2456510.54852	9.84	0.19
		2456510.56038	9.76	0.19
				to be continued

Table A1.1 – Continuation

Candidate	Instrument	measurements		
		time[HJD]	RV [km/s]	RV-error [km/s]
		2456510.57224	9.80	0.19
		2456510.58728	9.66	0.19
		2456510.59915	9.71	0.19
		2456510.61101	9.71	0.19
		2456510.62305	9.72	0.19
		2456510.63490	9.68	0.19
		2456510.64676	9.92	0.19
		2456510.65885	9.66	0.19
		2456510.77030	9.58	0.19
		2456782.90083	9.49	0.19
	HARPS			
		2456093.80675	10.18	0.20
		2456096.67636	9.99	0.20
		2456098.79155	10.15	0.20
		2456101.67704	10.01	0.20
		2456115.70754	9.98	0.20
		2456118.64215	10.05	0.20
	FIES in transit			
		2456499.39103	9.61	0.38
		2456499.40588	9.67	0.33
		2456499.42072	10.08	0.42
		2456499.43564	9.72	0.28
		2456499.45169	9.74	0.17
		2456499.46652	9.57	0.14
		2456499.48135	9.06	0.38
		2456499.49626	9.40	0.34
		2456499.51231	9.36	0.18
		2456499.52715	9.64	0.25
		2456499.54199	9.49	0.24
		2456499.55689	9.58	0.54
		2456499.57294	9.06	0.32
		2456499.58778	9.58	0.56
		2456499.60264	9.20	0.10
		2456499.61754	9.25	0.38
		2456499.63358	9.31	0.46
		2456499.64843	9.23	0.23
	FIES Second run			
		2456101.60540	9.68	0.43
		2456102.58413	9.24	0.30
		2456104.50742	10.12	0.72
		2456107.49199	9.27	0.54
	FIES Third run			
		2456118.51460	9.28	0.24
		2456119.45816	9.58	0.26
		2456120.45199	9.68	0.63
		2456121.62526	9.68	0.34
		2456122.49860	9.53	0.48
	FIES Fourth run			
		2456459.46791	9.65	0.27
		2456461.46262	9.65	0.13
LRc07_E2_0482	SANDIFORD			
		2456115.74109	63.25	0.09
		2456116.75534	37.21	0.30
	TWIN			

Table A1.1 – Continuation

Candidate	Instrument	measurements		
		time[HJD]	RV [km/s]	RV-error [km/s]
		2456818.44748	49.32	4.35
		2456818.63589	74.64	4.68
		2456820.38910	63.68	4.62
		2456821.39135	-12.89	5.23
		2456821.64610	-16.37	5.04
	IDS			
		2456429.68899	111.69	3.31
		2456430.69020	20.70	0.99
		2456432.69440	16.56	1.17
LRc08_E2_4203	TWIN			
		2456818.48244	15.95	1.38
		2456818.57451	17.64	0.24
		2456820.48877	23.69	3.24
		2456821.46328	15.68	1.42
		2456821.60504	21.30	1.67
		2456855.44570	26.23	1.61
	HARPS			
		2456097.77494	17.78	0.50
		2456099.67744	9.92	0.50
	UVES			
		2456861.54386	15.93	0.20
		2456861.56163	15.38	0.20
		2456863.56748	16.32	0.20
		2456863.58525	16.86	0.20
		2456866.73130	16.55	0.20
		2456866.74906	17.50	0.20
		2456868.52861	16.43	0.20
		2456868.54637	17.89	0.20
LRc10_E2_3265	TWIN			
		2456818.51769	11.07	1.54
		2456820.43990	12.70	1.14
		2456821.51005	10.65	1.60
		2456821.56399	8.11	0.58
		2456855.49774	12.04	0.74
		2456855.52629	7.20	2.48
IRa01_E2_2721	SANDIFORD			
		2456298.81700	-112.95	0.76
		2456299.85633	-85.35	21.04
		2456300.73399	34.20	0.36
		2456300.83410	7.16	0.31
	CAFE First run			
		2456280.42544	6.05	39.32
		2456280.50753	-9.57	18.11
		2456280.58581	-13.20	7.05
		2456280.67723	8.21	2.61
	CAFE Second run			
		2457018.42973	25.69	5.39
		2457018.64910	16.41	1.29
		2457019.63230	-5.61	20.56
		2457019.61976	23.96	1.41
	UVES			
		2456936.78085	1.22	2.05
				to be continued

Table A1.1 – Continuation

Candidate	Instrument	measurements		
		time[HJD]	RV [km/s]	RV-error [km/s]
		2456936.76911	2.98	0.92
		2456937.81161	-1.59	4.53
		2456937.79993	0.68	1.14
		2456942.75984	2.04	2.27
		2456942.84508	-0.16	1.41
		2456942.82168	1.29	1.85
		2456958.79352	5.82	3.53
		2456965.77321	1.50	2.35
		2456965.81303	4.53	4.68
IRa01_E1_4591	CAFE			
		2456278.65345	59.54	23.14
		2456278.67541	84.30	26.27
		2456279.65790	54.32	1.06
		2456279.68020	76.35	1.24
		2456280.48853	25.35	1.49
		2456280.54243	57.58	1.27
		2456280.54243	57.58	1.27

A.2 Spectral types from low resolution Nasmyth-spectra

Table A2.1: Spectral types from low resolution spectra obtained with the Nasmyth spectrograph

Object	Spt	Template
IRa01_E1_2692	F7 V	HD51530
IRa01_E2_0783	F8 V	HD35296
IRa01_E2_1712	A9 V	HD162570
IRa01_E2_3952A	B4V	HD189944
IRa01_E2_3952B	B4IV	HD180554
LRa01_E1_0286	G8 V	HD128167
LRa01_E1_2240	F6 II	HD61295
LRa01_E1_3221	F2 V	HD128167
LRa01_E2_0203	F1 V	HD168092
LRa01_E2_0928	B5 IV	HD41692
LRa01_E2_1578	F6 V	HD173667
LRa01_E2_3739	B3 V	HD74280
LRa01_E2_4519	A4 V	HD136729
LRa02_E1_4967	F2 V	HD128167
LRa02_E2_0764	G0 V	HD48682
LRa02_E2_4496	B4 IV	HD180554
LRa02_E2_5607	F-star	(HD91752)
LRa03_E2_0678	K3 V	HD139323
LRa03_E2_0861	G9 V	HD185144
LRa03_E2_1326	G8 V	HD184385
LRa03_E2_3913	G6 V	HD117043
LRa04_E2_2875	K0 IV	HD99491
LRa05_E2_0385	B9 V	HD15318
LRa05_E2_1168	F8 V	HD35296
LRa05_E2_3796	K0 IV	HD99491
LRa06_E2_5287	F5 V	HD168151
LRa07_E2_3354	A2 II	HD39866
LRa07_E2_4439	K3 V	HD139323
LRc03_E2_0935	F7 V	HD215648
LRc03_E2_5079	K5 III	HD47914
LRc03_E2_5451	K0 IV	HD99491
to be continued		

Table A2.1 – Continuation

Object	Spt	Template
LRc04_E2_2875	G5 V	HD59747
LRc04_E2_4032	G0 V	HD176377
LRc04_E2_5713	G0 V	HD165401
LRc05_E2_0168	G0	HD176377
LRc05_E2_3718	G0.5 Va	HD84737
LRc06_E2_0119	F7 V	HD187013
LRc07_E2_0146	F8 V	HD210855
LRc07_E2_0158	F7 IV	HD216385
LRc07_E2_0182	F6 IV	HD120136
LRc07_E2_0187	F7 V	HD215648
LRc07_E2_0307	F6 V	HD173667
LRc07_E2_0482	F7 V	HD215648
LRc07_E2_0534	K2 III	HD180610
LRc07_E2_2968	G8 V	HD184385
LRc07_E2_4203	G0 .5Va	HD84737
LRc08_E2_0275	G5	HD192699
LRc08_E2_4203	F3 V	HD91752
LRc08_E2_4520	G0.5 Va	HD84737
LRc09_E2_0131	K0 III-IV	HD168723
LRc09_E2_0308	G0 V	HD157214
LRc09_E2_0548	G5 IV	HD10697
LRc09_E2_0892	K1 III	HD160290
LRc09_E2_2479	K5 III	HD47914
LRc09_E2_3338	A4 V	HD136729
LRc09_E2_3403	G0.5Va	HD84737
LRc10_E2_0740	K5 III	HD157681
LRc10_E2_1984	M7.5 III	HD126327
LRc10_E2_3956	G0.5 Va	HD84737
LRc10_E2_5093	K1.5 III	HD170693
SRa01_E2_2379	B4 III	HD183144
SRa02_E1_1011	F9 V	HD102870
SRa03_E2_1073	F3 V	HD91752
SRa05_E2_3522	A4 V	HD136729
SRa05_E2_4016	G5 V	HD59747
SRc01_E1_0346	B5 IV	HD41692

Instrument	Telescope	Date	Observer	Object	Spt
TWIN	CAHA 3.5 m	05/2012	C. Heuser	LRc02_E1_0132	F6 III
				LRc03_E2_0832	F0 IV
				LRc03_E2_2657	A7 V
				LRc07_E2_0108	A9 IV
				SRc01_E1_0346	B5 III
ISIS	WHT	12/2012	T. Kupfer	IRa01_E1_2721	A2 IV
				IRa01_E1_4591	A5 V
				LRa01_E2_0203	F2 IV
				LRa02_E1_1475	A5 V
				LRa02_E1_4129	A9 IV
				LRa02_E2_1023	F3 V
				LRa02_E2_4150	B4 V
ISIS/IDS	WHT/INT	06/2013	C. Heuser	LRc05_E2_0168	F9 V
				LRc07_E2_0146	F6 IV
				LRc07_E2_0187	F5 V
				LRc07_E2_0482	F6 V
TWIN	CAHA 3.5 m	07/2014	E. Ziegerer	LRc09_E2_3322	F3 V

Table A3.1: Spectral types from low resolution spectra observed by our collaboration partners

A.3 Spectral types from low resolution spectra from other spectrographs

A.4 Observational parameters of the transit-candidates

ID	Rectascention [h:m:s]	Declination [h:m:s]	apparent magnitude
IRa01_E1_4591	06:46:10.244	-01:42:23.630	B:14.48; R:13.21
IRa01_E2_2721	06:47:23.865	-03:08:32.377	R:12.98
LRa01_E2_0203	06:41:00.051	-01:29:29.738	B:11.91; V:11.51; R:11.56
LRa01_E2_0963	06:41:34.477	-00:53:57.746	B:14.80; R:14.15
LRa01_E2_1578	06:42:05.924	-00:31:31.390	B:14.73; R:13.57
LRa02_E1_0725	06:52:36.485	-03:07:30.151	B:13.53; R:13.42
LRa02_E1_1475	06:51:29.005	-03:49:03.486	B:13.99; R:13.41
LRa02_E2_1023	06:53:25.072	-05:42:47.027	R:13.35
LRa02_E2_4150	06:50:01.371	-05:12:07.448	B:10.62; V:10.55; R:10.82
LRc02_E1_0132	18:43:16.951	+05:58:00.246	B:12.70; V:11.95; R:11.59
LRc03_E2_2657	18:31:19.816	-06:21:23.875	B:14.65; R:13.14
LRc07_E2_0108	18:33:35.740	+07:42:19.278	B:11.65; V:11.15; R:11.44
LRc07_E2_0307	18:31:00.241	+07:11:00.125	B:13.72; V:13.06; R:12.72
LRc07_E2_0482	18:31:00.762	+07:08:26.322	R:12.78
LRc08_E2_4203	18:33:27.345	+05:20:01.334	B:16.04; R:14.64
LRc10_E2_3265	18:35:59.542	+07:49:08.436	B:14.93; R:14.03

Table A4.1: Coordinates of CoRoT candidates, in this survey

Ehrenwörtliche Erklärung

Ich erkläre hiermit ehrenwörtlich, dass ich die vorliegende Arbeit selbständig, ohne unzulässige Hilfe Dritter und ohne Benutzung anderer als der angegebenen Hilfsmittel und Literatur angefertigt habe. Die aus anderen Quellen direkt oder indirekt übernommenen Daten und Konzepte sind unter Angabe der Quelle gekennzeichnet.

Dr. Eike W. Guenther hat mir unentgeldlich als Betreuung der vorliegenden Arbeit geholfen. Weitere Personen waren an der inhaltlich-materiellen Erstellung der vorliegenden Arbeit nicht beteiligt. Insbesondere habe ich hierfür nicht die entgeltliche Hilfe von Vermittlungs bzw. Beratungsdiensten (Promotionsberater oder andere Personen) in Anspruch genommen. Niemand hat von mir unmittelbar oder mittelbar geldwerte Leistungen für Arbeiten erhalten, die in Zusammenhang mit dem Inhalt der vorgelegten Dissertation stehen.

Die Arbeit wurde bisher weder im In- noch im Ausland in gleicher oder ähnlicher Form einer anderen Prüfungsbehörder vorgelegt.

Die geltende Promotionsordnung der Physikalisch-Astronomischen Fakultät ist mir bekannt.

Ich versichere ehrenwörtlich, dass ich nach bestem Wissen die reine Wahrheit gesagt und nichts verschwiegen habe.

Jena, den 01. Oktober 2016

_____

Sebastian, Daniel

Seitens des Verfassers bestehen keine Einwände, die vorliegende Doktorarbeit für die öffentliche Nutzung in der Thüringer Universitäts- und Landesbibliothek zur Verfügung zu stellen.

Jena, den 01. Oktober 2016

_____

Sebastian, Daniel

Lebenslauf

Zur Person

Name	Sebastian
Vorname	Daniel
Geburtsdatum	03.03.1987
Geburtsort	Leipzig

Werdegang

seit 02.2016	Mitarbeiter in der Technologie bei der asphericon GmbH
10.2011 - 01.2016	Doktorand an der Thüringer Landessternwarte (TLS)
06. - 09.2011	Wissenschaftliche Hilfskraft an der TLS Teilnahme an ESA Summer School Alpbach (07.2011), Teilnahme an IMPRS Summer School Heidelberg (08.2011)
10.2005 - 05.2011	Physikstudium an der FSU Jena und Diplomarbeit an der TLS Betreuer: Prof. Dr. Artie P. Hatzes Thema: "Die Suche nach frühen Sternen in der CoRoT Durchmusterung" Abschluss: Diplom Physiker

Voträge

09.2014	Jahrestagung der Astronomischen Gesellschaft in Bamberg "Transiting Sub-stellar companions of Intermediate-mass stars"
03.2013	CoRoT-Week workshop, in La Laguna, Teneriffa, Spanien "Transiting planets of intermediate-mass stars"
06.2012	öffentlicher Vortrag zu langen Nacht der Museen, Jena Unbekannte Welten- Mit Raumsonden den Geheimnissen unseres Sonnensystems auf der Spur!
02.2012	öffentlicher Vortrag zu den Sternguckertagen in Volkenroda "Exoplaneten"
09.2011	Jahrestagung der Astronomischen Gesellschaft in Heidelberg "The stellar population in the CoRoT-fields"

Liste der Veröffentlichungen

Sebastian, D., Guenther, U. Heber, et al. 2015, "Transiting Sub-stellar companions of Intermediate-mass stars", Conference proceedings, to be published through the EPJ Web of Conferences

Sebastian, D., Guenther, E. W., Schaffenroth, V., et al. 2012, Multi-object spectroscopy of stars in the CoRoT fields - I. Early-type stars in the CoRoT-fields IRa01, LRa01, LRa02, A&A, 541, A34

Sebastian, D. & Guenther, E. W. 2011, Identifying A Stars in the CoRoT Fields IRa01, LRa01 and LRa02 in American Institute of Physics Conference Series, Vol. 1331, American Institute of Physics Conference Series, ed. S. Schuh, H. Drechsel, & U. Heber, 329 - 335

Lehmann, H., Guenther, E., Sebastian, D., et al. 2015, "Mass of WASP-33b", Astron. & Astrophys., 578, L4

Ammler-von Eiff, M., Sebastian, D., Guenther, E. W., Stecklum, B., & Cabrera, J. 2015, "The power of low-resolution spectroscopy: On the reconnaissance of planet candidates in the ground-based CoRoT follow-up", Astronomische Nachrichten, 336, 134

Ammler-von Eiff, M., Sebastian, D. Guenther E.W., 2014, "Quantitative Stellar Classification with Low-Resolution Spectroscopy", Proceedings of the IAU Symposium, Vol 293, pp. 375-377

Pribulla, T., Sebastian, D., Ammler-von Eiff, M., et al. 2014, "Cerro Armazones spectroscopic survey of F dwarfs", Mon. Not. R. Astron. Soc., 443, 2815

Maxted, P. F. L., Bloemen, S., Heber, U., et al. 2014, "EL CVn-type binaries - discovery of 17 helium white dwarf precursors in bright eclipsing binary star systems", MNRAS, 437, 1681

Volkov, I. M., Chochol, D., Grygar, J., et al. 2013, "Period changes in the eclipsing binary DX Vel", Information Bulletin on Variable Stars, 6066, 1

Guenther, E. W., Gandolfi, D., Sebastian, D., et al. 2012b, "Multi-object spectroscopy of stars in the CoRoT fields - II. The stellar population of the CoRoT fields IRa01, LRa01, LRa02, and LRa06", A&A, 543, A125

Jena, den 01. Oktober 2016